Theory, Fabrication and Applications of a Novel Archetype Semi-Ring Fabry-Perot (SRFP) Resonator, and New Tiltmeters

Thesis by

Shervin Taghavi Larigani

Submitted in Partial Fulfillment of the

Requirements for the Degree of

Doctor of Philosophy
Electrical Engineering

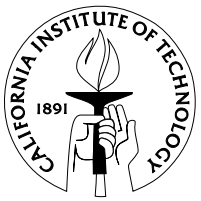

Pasadena, California

Defended December 15, 2005

Dedication

To my father who said: "Go and become strong since in the reign of nature the rights of weakers are wiped out" and "The one who lets his rights to be taken is more guilty than the one who actually takes them away".

Acknowledgments

The acknowledgments, though written last in a thesis, are located at the beginning. This corresponds very well to the fact that by far this is the most interesting part and the most read since it adds a personal touch. My stay at Caltech has been a great source of learning not only from a technical point of view but also in terms of human elements and has certainly helped me to grow more mature and strong. I also learned that the academic environment is like any human social structure subject to human goodwill or personal behavior fluctuation. I would certainly not be able to write this thesis without the help of Professor Hoffman, who beyond any professional obligation gave me the opportunity to defend my ideas. I also have to thank Dr. Jakob Van Zyl, my co-advisor, who despite having high responsibility in the hierarchy of JPL shows extremely high technical skill and human skill. I also have to thank Prof. Bruno Crosignani, Prof. Vahala and Prof. McGill for their encouragements. I am also indebted to Prof. Psaltis and Prof. McEliece to have kindly agreed to be on my thesis defense committee.

I also have to thank Jeremy Witzens and William Green for their help. Special thanks needs to be extended to Dane Boysen (who I believe will become a very prominent entrepreneur and will strongly impact society on account of his mind, generosity, and integrity), Ravi Abrol (who is among those people that, beyond having undisputable scientific skill, also have a real sense of human being), Saurabh Vyawahare, and all who helped proofread this thesis.

I also thank Vidya and Mehrdad Mahmoudi Zarandi, who share the same qualities as Ravi, which consist of combining great human and scholar qualities. Special thanks also should be extended to my dear friend Jim Endrizzi (who is the head of the International Student Program), Cedric Florens, Jack Geasland (Vietnam veteran, writer, and currently a humanity science instructor), and Linda Dozsa. I also thank Parsa Dormiani. I shouldn't also forget my dear friend Mike who was an ESL teacher at Caltech and who has lost his life to cancer. Sometimes some events can change a life, e.g, what happened when my aunt Sousan gave me a drive to Caltech for my first visit of the campus (during my stay in the USA) one year before I came here

for my PhD. I also thank the following who encouraged me to move to the USA or to come to Caltech: Dr. Fan and Prof. Khan (l'Universite Paris Sud Orsay), Miss Harris, Mike Donahoe. I also would like to mention my new great friends, Joe and Doug, who have been a great motivation for ending the thesis. I also would like to thank my office mates Wei Liang and Xiankai Sunwith whom I had great discussions. I would like to thank Dr. Mike Sellessor and Dr. Rich Wolf (from the patent office at Caltech) for their great support throughout the processing of my patents.

In all acknowledgements there are usually great phrases dedicated to the parents of the author. However, in my case I should express additional gratefulness, due to the fact that since the event of 1979 that happened in Iran, the life of my parents has completely changed and they completely lost literally everything, but still they managed to bring up their kids so well. I am indebted to my mother Simin-Dokht and brother Ramtin for their affection and support. Finally, I would like to thank my best friend, my master, my father, Jalal, to whom I owe everything I am and have. If it were not for his help, I would never have come to the USA and I would never have performed well. He has been always teaching me and showing the many dimensions of life that the common people ignore (the analogy is when common people will see only one dimension of something that has 10 dimensions). It may seem very arrogant of me, but he is really the only person that I have been impressed by. It is always an easier task to behave correctly and wisely and make great achievements when the environment is appropriate. It is something else to behave so in a very rough situation. As I like to say "stars shine in darkness," and indeed I have been extremely impressed by the great human sense, integrity, immeasurable mental strength, noncomparable visions and imaginations of my father. I believe that people come and go but what will stay forever is the track that we leave and in my father's words, "Rights are not given, they are taken".

Shervin Taghavi Larigani, Pasadena, California, USA, 2 November, 2005.

Theory, Fabrication and Applications of a Novel Archetype Semi-Ring Fabry-Perot (SRFP) Resonator, and New Tiltmeters

by

Shervin Taghavi Larigani

ABSTRACT OF

Submitted in Partial Fulfillment of the

Requirements for the Degree of

Doctor of Philosophy

Electrical Engineering

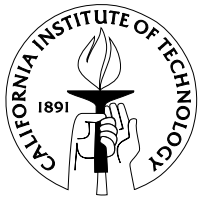

The

Pasadena, California

Defended December 15, 2005

Abstract

The first instinct of any animal (including human) is surviving, which implies security. It impacts how we perceive the whole universe. The best way of satisfying this need, consists of being able to control situations in which we are immersed. One way of doing so, consists of predicting future events. That is why we perceive and model our environment based on cyclic and periodic events, going back to the earliest civilizations.

Few examples of such periodic events are:

- The rotation of earth around the sun, which illustrates a spatial cyclic event.
- The alternate of day and night, which illustrates a temporal cyclic event.

So modeling any sort of event happening in our environment by repetitive events allows us to enforce a secure feeling, since (periodic, cyclic) events have the advantage of being able to be foreseen, which provides the advantage of being well understood. Most of the devices fabricated by human beings are inspired by the perception of its environment, and somehow in most cases we just copy nature. Few examples are:

- Airplanes are similar to birds.
- Submarines are similar to whales or sharks.

That is why basic tools of many applied and engineering sciences are resonators, which are engineered devices that generate or sustain periodic or cyclic events. One example of a resonator is a guitar. The string can just take a certain finite number of shapes since it is bounded on its two extremes. Any excitation of the string can be decomposed as the excitation of each one of these shapes, which would repeat itself

after one round trip. These shapes are called the resonant mode of the string. Each note (the music coming out of it) of the guitar corresponds to one of its resonant modes. The same way that we use a basis to describe a vector (for example x and y in the case of two dimensional vector), we can use the resonant modes as a basis to describe any intensity within the resonator. Therefore in the case of the guitar, any vibration of the string can be decomposed on a set of vibrations of each resonator mode, where the intensity of vibration of each mode is independent of the others. What differentiates any vibration of the string from another is the intensity with which this vibration couple, to each resonant mode. The same way that the guitar is a mechanical resonator, we can think of an electromagnetic resonator. The same way an electromagnetic resonator has different resonant modes, and each intensity couple to the resonator can be decomposed on a set of intensity of each resonant mode. Another example is at the atomic scales, where the atoms within a molecule have specific repetitive vibration and rotation patterns, which are called the resonant modes.

The overall concept of a resonator is the same whether it is mechanical or electromagnetic one. The basic concept of a resonator is based upon a feedback, which guarantees the repetition of an event. At the root there are no more than two ways of obtaining such feedback.

1 The first idea consists of forcing the feedback. Due to this feed back the same event would happen at the same time if it is a temporal event or at the same location if it is a spatial event.

By confining the event within a (temporal or spatial) barrier, and by being sure that the event would bounce back at that barrier, we would have created such a feedback. Such a specific barrier is often called a reflector. In the case of a mechanical resonator, such a reflector could be a wall. As an example, when someone talks within a confined structure, their voice gets echoed or resonates and in some cases the voice

generated by the speaker would get back to him. This is a resonant phenomenon. Another example is if someone who is confined in a medium separated by two walls throws a ball to one of the walls. In a specific case, where the trajectory of the ball repeats itself, we talk about resonance. The same structure is also used in an electromagnetic resonator where the two reflectors are now electromagnetic reflectors. In the case of optics, the reflectors would be mirrors. In that case, the feedback would be obtained by confining an optical medium (a waveguide) within two optical reflectors (mirrors). Such a structure is the most basic archetype resonator in optics and was invented 100 years ago, and was named after its inventors Fabry-Perot. Fundamentally, this structure is very similar to the mechanical resonator obtained with the help of two walls.

2 Another way of thinking of such a feedback is by assuring that either the temporal or spatial path used by the events would be repeated. This can be obtained if the path shape is closed. An example of such structure is a circular shape.

In this thesis, we present a completely novel resonator that in addition to having both the advantages of the first and the second types of resonators, has its own specific features. We have called this resonator a Semi-Ring Fabry-Perot (SRFP) resonator. In order to better understand this resonator we will focus ourselves in the field of optics, which emphasizes the best on the wave particularity of resonators. As we will see almost all optical resonators could be modeled as combinations of Fabry-Perot and ring resonators. These devices are the most important letter of the alphabet of the optics, where any device behaves like a word obtained with the combinations of the letters composing the alphabet, similar to introducing a new letter to the alphabet. Thus, we can with the use of this new letter create new words, which are new devices and could be useful. The benefit of the novel resonator that we introduce is beyond the scope of this thesis, where mostly optical applications of the resonator have been introduced.

At the end of the thesis, we will introduce a novel way of measuring the incidence tilt of a field using a resonator.

Contents

List of Figures **xix**

Glossary **xxx**

1 Introduction **1**

1.1 The Fabry-Perot: An archetype resonator 5

1.2 Ring resonator 8

1.3 Grating structures 9

1.3.1 Loss in a grating structure 10

1.3.2 The reflection spectrum of a grating structure 12

1.3.3 Buried grating structure 14

2 Analysis of Hypothetical Alternate Solutions to the Conventional Optical Structures **18**

2.1 Integration of a Fabry-Perot resonator on a chip in parallel with a waveguide 18

2.2 Ring resonator and combinations 20

3 Introduction to the Semi-Ring Fabry-Perot Resonator 24

3.1 Advantages of the SRFP resonator (over a conventional ring or Fabry-Perot resonator) 25

3.1.1 Advantages of the SRFP resonator over a ring resonator . . . 25

3.1.2 Advantages of the SRFP resonator over a Fabry-Perot resonator 26

4 Different Examples of NonSRFP Resonators 31

4.1 Discussing the case where the HR facet is interacting with the main waveguide 31

5 Modeling the Resonator 36

5.1 Modeling the coupling region 36

5.1.1 Special case where the coupler is symmetric 41

5.2 Modeling the SRFP resonator 43

5.2.1 Modeling the reflection and transmission between ports 1 and 3 as illustrated in fig. 5.1 43

5.2.2 T matrix of the structure 44

5.3 Modeling the reflection and transmission between ports 1 and 4 . . . 51

5.3.1 T matrix of the structure depicted in fig. 5.9 53

6 Case Where the SRFP Resonator is a Lossless and Symmetrical Resonator 55

7 Characterization of the Waveguide **63**

7.1 Slab waveguide 63

7.2 Effective index technique 65

7.2.1 Large index discontinuity assumption 65

7.2.2 Effective index technique 66

7.3 Numerical finite-difference eigenmode solver 67

8 Fabrication **73**

8.1 Choice of the material 73

8.2 Choice of the gas for etching 74

8.2.1 Several etches 75

8.2.2 The carbon tetrachloride etch 75

8.2.3 The use of CH_4/H_2 etching 77

8.2.4 Introduction of HI/H_2 78

8.2.5 Fabrication 78

9 Choice of the Coupling Region **81**

9.1 Adiabatic coupler 81

9.2 Evanescent coupler 82

9.3 TMI coupler 83

9.4 The multi-modes interference (MMI) coupler 84

9.5 Restricted interference multi-mode resonance 88

10 Testing **96**

10.1 Preliminary simulation 98

10.2 Testing an ˜3 dB SRFP resonator with low reflection coating 100

10.2.1 Testing the MMI coupler 100

10.3 Testing an ˜3 dB SRFP resonator with high reflection coating 101

10.4 Testing an SRFP with low coupling coefficient and with a high reflection coating 103

11 SRFP Resonators Used in Delay Line Schematics **112**

11.1 SRFP can be a non-MPF in transmission 114

11.2 Comparing the delay time of an SRFP with that of an FP and ring resonators 115

11.3 A 3 x 3 coupling region 116

12 SRFP with other resonators **119**

12.1 MZI inside an SRFP resonator 119

12.2 Comparison of two different embodiments combining an SRFP resonator and an MZI 124

12.3 Study of the back reflection 125

12.4 Other embodiments combining an SRFP resonator with other resonators 125

13 SRFP Resonator Used as Modulator **132**

14 Different Laser Applications of the SRFP Resonator **134**

14.1 Analysis of a laser using a single SRFP resonator with an MZI 135

14.2 Qualitative description of the tunable laser 136

14.2.1 Adding the SRFP resonator to the MZI 138

14.3 Engineering a single SRFP laser 140

14.4 SRFP on each side of a gain medium 144

15 Novel Laser Embodiments using Planar Fabrication and Based upon Interferometry Techniques Different from SRFP **149**

15.1 Tunable lasers combining ring resonators 150

15.1.1 A single ring resonator 151

15.1.2 Laser obtained with the combination of ring resonators located on each side of the gain medium 152

15.1.3 Conclusion 152

15.2 A laser using two Mach-Zehnder interferometers 153

16 General Novel Laser Embodiments **159**

17 Other Designs of the SRFP Resonator **161**

18 SDFP and SSFP **162**

18.1 Semi Disk Fabry-Perot resonator (SDFP) 162

18.2 Semisphere Fabry-Perot resonator 163

19 An Electronic Version of the SRFP Resonator **165**

20 Novel Tiltmeter **168**

20.1 A novel angle tiltmeter based on the use of a Fabry-Perot resonator . 169

21 Conclusions **176**

References **180**

List of Figures

1.1 Top view of a Fabry-Perot resonator. 6

1.2 Pictures of the transmission and the reflection of the Fabry-Perot resonator, where $\Delta\nu_{1/2}$ is the separation between the two frequencies at which the intensity is down to half of its peak value. 7

1.3 Top view of a ring resonator coupled to a waveguide. 9

1.4 Depicts a rectangular grating. Λ is the period of the structure, Λ_m is the mark length, d_g is the grating thickness, n_1 and n_2 the indices of refraction of the materials forming the grating. 10

1.5 Illustration of a ridge waveguide. Since the etching is not perfect, some roughness appears in the contour of the ridge. 11

1.6 Represents the wafer before being etched case A, the ridge waveguide with an shallow etched case B, ridge waveguide with a deep etch case C. 12

1.7 Intensity reflectivity as function of $\Delta\beta L$ with kL as parameter [4]. . 13

1.8 A GaAs-GaAlAs cw DFB injection laser with a corrugated interface (grating structures) [6]. 14

1.9 III-V compounds: Lattice constants versus bandgap energy and corresponding bandgaps wavelengths. The solid lines correspond to direct-gap materials and the dashed lines to indirect-gap materials. The binary-compound substrates that can be used for lattice-matched growth are indicated on the right, [7]. 15

2.1 Coupled Fabry-Perot resonator. 19

2.2 Crossing view of a Fabry-Perot resonator obtained by the use of grating structures as reflectors. 20

2.3 Top view of a ring resonator coupled to a waveguide terminated with a mirror. 21

2.4 Reflected light intensity spectrum of a ring resonator with a reflector shown in fig. 2.3. 22

2.5 Top view of a structure obtained by the combination of a Y junction and two coupling regions and two absorption regions. 23

3.1 Top view of an SRFP resonator. 25

3.2 Representation of the reflection of an SRFP resonator and that of a Fabry-Perot resonator. 27

3.3 Reflection and transmission light spectrum of an SRFP resonator with a 3 dB coupler versus wavelength. 28

3.4 Reflection and transmission light spectrum of an SRFP resonator with low coupling. 29

3.5 Reflection and transmission light spectrum of an SRFP resonator with high coupling ($k = j.0.9$). 30

List of Figures

4.1 Representation of a device in which the HR facet is interacting with the main waveguide. Hence, this device is not an SRFP resonator. . 32

4.2 Illustration of the fact that in region A the modes of the resonator and those of the waveguide can disturb each other. 33

4.3 Representation of the resonator and emphasizing on the existence of 3 waveguides 1,2 and 3 instead of 2 in the case of an SRFP resonator. 34

4.4 Interruption of the main waveguide using a high reflection facet. . . 35

5.1 Representation of an SRFP resonator with the association of the coupling region. 37

5.2 Representation of the forward light in the coupling region. 38

5.3 Representation of the reverse light in the coupling region. 39

5.4 Illustration of a symmetrical coupler with respect with the two transversal axes. 42

5.5 Representation of the actual device where in addition of the HR facet we also have reflection resulting from the boundary between the wavguide and air ($r_1$and r_3). 45

5.6 Representation of the field flux at port i and port j of an unknown device. 46

5.7 Illustration of the interface of two different media (i and j) with respective indexes of refraction n_i and n_j. 49

5.8 Representation of a schematic where the output is located on the side of the high reflection coating. 51

5.9 Depicts the structure where the input is the field a_1 and the output field is b_4. 52

6.1 Representation of an SRFP resonator where a_1 is the input field, b_3 the transmitted field, and b_1 is the reflected field. 56

6.2 Representation of an SRFP resonator where a_3 is the input field, b_1 is the transmitted field and b_3 is the reflected field. 60

6.3 Representation of the difference of phase between the reflected field and the transmitted one when the resonator is symmetrical and lossless, which means that r_{hr}=1. 61

6.4 Representation of the difference of phase between the reflected and the transmitted fields in the case that the SRFP resonator is symmetrical but not lossless since the reflection of the HR is 90%. 62

7.1 Schematic of a three-layer slab waveguide. Indices are assumed to be uniform in the z-direction. 64

7.2 View of the cross section of the waveguide. The different transverse regions are denoted A, B, C, and the lateral ones 1, 2, 3 [40]. 66

7.3 Illustration of a finite difference grid over a buried-rib waveguide. . . 68

7.4 Beam profile of the fundamental TE mode obtained by using the numerical finite differential method that we implemented. The lines in blue illustrate the outline of the different material layers composing the ridge waveguide. The structure of the ridge waveguide is the one shown in fig. 1.5. The effective index for the mode shown is $n_{eff} = 3.36$. Depending on the width and the length of the ridge, we can either get a single or multi-mode waveguide. 72

8.1 Illustration of the different steps of fabrication. 79

9.1 (a) and (b), simulations of light (power) propagation along an asymmetric adiabatic coupler directional coupler and (c), along a symmetric directional coupler. The light is coupled through the input guide at the bottom [66]. 89

9.2 Representation of a classical two-mode interference (TMI) coupler. 90

9.3 Energy distribution along the propagation direction in a two-mode waveguide due to the interference between modes [80]. 91

9.4 Illustration of a 2 X 2 MMI coupler where the input and output waveguides are single-modes and where the center waveguide supports multi-mode. The propagation happens along the z-axis [84]. . 92

9.5 The cross section profiles of different modes. 93

9.6 Top view of a 3 dB MMI coupler based on the restricted interference theory. 94

9.7 SEM picture of a fabricated MMI coupler. 95

10.1 Representation of the testing bench. 96

10.2 (a) Represents the reflection spectrum of the FP and the SRFP separately and (b) represents the reflection spectrum of the structure shown in fig. 5.5. 98

10.3 (a) Represents the transmission spectrum of the FP and the SRFP separately and (b) represents the transmission spectrum of the structure shown in fig. 5.5. 99

10.4 Analogy between a simple MMI coupler and an SRFP resonator. . . 101

10.5 Plot in decibel (db) of the normalized reflection spectrum of the device shown in fig. 10.4 versus wavelength. Between two consecutive strong modes there is a less strong mode. This has been predicted by simulations and characterizes the existence of an SRFP inside an FP. Even in this case where the reflection coating of the SRFP has a low value, which corresponds to the reflection created between the waveguide and air interfaces, one can distinguish the contribution of the SRFP alone to the spectrum shown above. The coupler has been designed to be a 3 dB coupler. However, testing has shown that the coupling is 51% instead of 50%. 102

10.6 Plot in decibel of the normalized transmission spectrum of the device shown in fig. 10.4 versus wavelength. As can be seen the shape of the spectrum corresponds to that has been predicted by simulations. Similar to the reflection where we could distinguish the contribution of the SRFP alone, here also the contribution of the SRFP from the transmission spectrum shown can be easily distinguished. 103

10.7 Plot in decibel of the normalized reflection spectrum of an SRFP, where the coupler has been designed to be a 3 dB coupler. The contribution of the SRFP, which corresponds the strong peaks can be clearly seen. 104

10.8 Close-up of fig. 10.7 showing the intensity contribution of the SRFP. 104

10.9 Plot in decibel of the normalized reflection spectrum of the device shown in fig. 10.11. The coupler has been designed to be a 3 dB coupler. The contribution of the SRFP corresponds to the strong peaks. 105

10.10 Close-up of the MMI coupler used in the SRFP. 106

10.11 Picture of a fabricated SRFP. 107

10.12 Plot in decibel of the normalized reflection spectrum of a device with high reflection coating and low coupling coefficient. The coupler has been designed to be a low coupler. The contribution of the SRFP corresponds to the strong peaks. 108

10.13 This is a close-up of the plot shown in fig. 10.12 in order to emphasize on the contribution of the SRFP to the intensity. 108

10.14 Plot in decibel of the normalized transmission spectrum of the device shown in fig. 10.15. The coupler has been designed to be a low coupler. The contribution of the SRFP corresponds to the strong peaks. 109

10.15 Top view of a fabricated SRFP resonator 110

10.16 (a)-(c) represent the pictures of an SRFP resonator; (d) represents an SRFP resonator before cutting the edges 111

11.1 Configuration where two SRFP resonators and a waveguide are coupled to each other with the help of 3 x 3 coupler. 117

11.2 Depicts a configuration among many others of a structure based upon a heavy use of SRFPs. Most probably, this structure would exhibit a very high delay time. This would be further enhanced in the case where the coupling coefficient between two SRFP facing each other is high and the one between the SRFP and the main waveguide is low. In that case the light is traveling from one resonator to the resonator facing it. It would mean that the light would have a much slower propagation speed along the axes of the main waveguide. 118

12.1 Spectrum of an MZI terminated by an high reflection facet and the reflection spectrum of an SRFP resonator. 120

12.2 The MZI is located outside the SRFP. 121

12.3 Intensity spectrum reflection of the device shown in fig. 12.2. 122

12.4 Structure where an MZI is located inside the SRFP resonator. . . . 123

12.5 The reflected intensity spectrum of the structure shown in fig. 12.4. 124

12.6 Comparison of the response of the structure where the MZI is located outside the SRFP resonator (shown in fig. 12.2) and the structure where the MZI is located inside the SRFP (shown in fig. 12.4). In the case where the MZI is located inside the SRFP, the difference between the strongest mode and the next strongest mode is further enhanced. 126

12.7 Mach-Zehnder interferometer inside SRFP resonator. This picture has been obtained after devloping the electron beam lithography. . . 127

12.8 Illustration of an embodiment combining an SRFP resonator and back mirror. 128

12.9 Illustration of both the reflection intensity with and without a rear facet versus the wavelength. The rear facet reflection is assumed to be equal to 0.99 and HR facet reflection corresponding to the natural reflection appearing between the semiconductor air interface and $L_3 = 4L_2$. 129

12.10 Illustration of both the reflection intensity with and without a rear facet. The rear facet reflection is assumed to be equal to the SRFP facet reflection HR facet reflection, which corresponds to the natural reflection appearing between the semiconductor air interface and $L_3 = 4L_2$. 130

12.11 Case (a) depicts a single SRFP, (b) depicts the combinations of an SRFP with waveguides of different lengths, (c) depicts combinations of an SRFP with other resonators and interferometers. The dashed box represents several examples (among many others) of resonators and interferometers that could be combined with the SRFP. 131

13.1 An SRFP modulator obtained with the help of an MZI within the coupling region. 133

14.1 Illustration of the top view of a tunable semiconductor laser where the tunable frequency mirror is obtained with the combination of an MZI inside an SRFP resonator (a). In (b) in addition to the combination of an MZI with an SRFP we also use a rear facet. . . . 136

14.2 Depicts a tunable laser, where the tunable mirror is composed with the combination of an MZI in addition to a reflection. 137

14.3 Illustration of the mode filtering by the MZ interferometer filter. . . 138

14.4 Illustration of the reflected intensity from the SRFP resonator and the location of the different modes of the device. 139

14.5 Illustration of the filtering of the modes of the laser by the combination of the SRFP resonator and the MZI. 140

14.6 The set of fig. 14.6 is related to the numerical application treated in this paragraph. Fig. 14.6 (a) represents the intensity coming back from the tunable frequency element versus frequency, (b) represents the MSR in dB versus the current in ampere, (c) represents the output power of the device in watts versus injected current in amperes. We did not take into account nonlinear effects, which limit the output power. 147

14.7 Laser embodiment where both resonators comprise SRFP resonators and are located on each side of the (gain and phase) medium. Depeneding on whether one would like to have a rear facet reflection, we can then decide whether to have the waveguide 3. 148

15.1 Top view of a tunable laser where the tunable frequency mirror is comprised of the combination of a ring resonator coupled to a semiconductor waveguide ended by a rear facet. 150

15.2 Top view of a tunable laser where the tunable frequency mirror is composed of two ring resonators coupled with the help of a 3 x 3 coupler to the same semiconductor waveguide ended by a rear facet reflection. A special design of the 3 x 3 coupler requires a high coupling efficiency between the ring resonators themselves and a low coupling coefficient between the ring resonator and the waveguide. . 156

15.3 Laser embodiment based upon the Vernier technique and using a ring resonator as the tunable frequency mirrors diposed within the semiconductor medium adjacent to the ends of the gain medium. . . 157

15.4 Top view of a tunable laser obtained by the combination of two MZIs. 158

15.5 Top view of a tunable laser obtained by the combination of two MZIs and terminated with a loop instead of a cleaved facet. 159

16.1 Illustrates a generic embodiment of lasers, which could be tuned in frequency also. 161

18.1 An Semidisk Fabry-Perot resonator. 164

19.1 Emphasizes the analogy between an electronic oscillator and an optical ring resonator. 167

19.2 Block diagram of an electronic version of the SRFP. 168

20.1 Multiple reflections model for analyzing the Fabry-Perot etalon. . . 171

20.2 Illustration of tiltmeter setup based upon the use of a Fabry-Perot resonator. 176

Glossary

APF	All pass filter
BCB	Benzocyclobutene
DWDM	Dense wavelength division multiplexing
FIR	Finite impulse response
FSR	Free-spectral range
HR	High reflection
InP	Indium phosphide
IPA	Isopropyl alcohol
MPF	Minimum phase filter
MSR	Mode suppression ratio
MMI	multi-modes interference
MSR	Mode suppression ratio
MZI	Mach-Zehnder interferometer
Non MPF	Non minimum phase filter

PMMA	Polymethylmethacrylate
SEM	Scanning electron microscope
SRFP	Semi-ring Fabry-Perot
SDFP	Semidisk Fabry-Perot
SSFP	Semisphere Fabry-Perot
TMI	Two modes interference
WDM	Wavelength division multiplexing

Chapter 1

Introduction

As explained in the abstract, resonators (independently of the field they are used in like optics, electronics, mechanics, and other ones) could be divided into two categories. In this thesis we introduce a novel type of resonator that besides combing the advantages of both types of resonators exhibits its own advantages and has unique features. In order to better understand this novel structure we will restrain ourselves to its applications for the field of optics. However, the same structure could be applied in other fields too. During the 80s and 90s we have a witnessed the tremendous development of optics. Optical devices are extensively used in fields like defense, medicine, and space. The main advantages of optical devices are high bandwidth, low delay time, high isolation of the network from outside agents, and high signal to noise ratio.

- Higher bandwidth:

Optical communications provide a bandwidth of several THz. This is many orders of magnitude better than wireless communications, which provide a band width of

several GHz at best.

- High isolation of the network:

In order to probe an optical network we have to physically interrupt it. This strongly perturbs the operation of the network. So by just monitoring the flux of communication between a source and a receiver one could easily see whether an external agent is listening to the system. This is the opposite in a wireless network, where listening to the system does not disturb it.

- Low delay time or fast transmission data for transcontinental communication:

In general, optical networks are able to deliver information much faster than wireless networks. This is because the trajectory traversed by the wave carrying information is much shorter in the case of an optical network. As an example, let us consider a transcontinental communication scheme: The optical network between the source and receiver will use optical cables. In the case of wireless communication, the information is transmitted from the source to the receiver via a satellite (the more sophisticated scheme using reflection from the ionosphere also exists, but we will not consider it here). It is straightforward to see then that in the case of a wireless network the information has to travel a much longer distance resulting in a higher delay time and more distorted information. In order to qualitatively appreciate the advantage of lower delay time in a communication network, let's consider the example of a phone communication between the USA and Europe 20 years ago. In those days there was a noticeable time delay from when the speaker ended speech and the counterpart heard it, which was a direct consequence of the long distance that the information had to traverse in the case of a satellite wireless communication. Since then, the laying of transcontinental optical fiber cables has allowed the use of an optical network. That is why the communication quality of a transcontinental

cable is as good as that of a local network and it is very hard to differentiate one from the other.

- High signal "capture" efficiency:

The amount of received signal relative to the emitted signal is higher than with wireless communication. Substantial literature comparing wireless and optical communication exists. Usually the authors expect one scheme of communication (wireless and optical depending on the field of interest) to prevail over the other one. In contrast, we would like to mention that these two schemes of communication are not competing with each other but are complimentary. With the development of the internet and the increase in the speed and size of communication signals, one could easily understand the advantages of an optical network. Most of the optics developments have happened in the area of communication operating in wavelength windows centered at 1.55 μm due to the low silicon loss at that specific wavelength. The technology has reached a state of relative maturity for this specific wavelength. Sophisticated fabrication tools requiring very difficult material growths and isotropic etchings were developed to create devices. That in turn enabled the fabrication of very complicated structures often based upon three-dimensional designs. One example is the buried grating structure used in distributed feed back (DFB) lasers. The fabrication of these complicated structures is made possible by accurate material epitaxial growth with the different materials that are gown on each other being lattice matched. Thus, lattice-matched conditions in most cases define the materials that could be used for the fabrication of such structures. The material bandgap energy defines the wavelength range in which the device could operate. Most of these materials are III-V materials and their bandgap energies allow optimum operation in the two most popular wavelength windows centered at 1.55 $\mu m$and 1.3 μm. If one finds in the future a need to develop systems operating in wavelength ranges that are not allowed by the bandgap energies of material that are lattice matched to each other,

then one cannot fabricate devices based on material epitaxial growths. That is why we believe structures based upon planar fabrication to be an emerging technology for future applications. Planar fabrication could be applied on any materials as long as they fulfill the conditions of lasing or wave guiding. We will introduce in this dissertation novel optical devices based upon planar fabrication. An important advantage of planar structures over other more sophisticated ones is their noticeable ease of fabrication. Most current optical devices are fabricated planar even though they may operate in telecommunication wavelengths where more sophisticated fabrication can be done. All optical devices are based upon the combinations and integrations of resonators and interferometers. The basic fundamental, archetype optical resonator is the Fabry-Perot, named after its inventors. This is nothing more than the optical version of the resonator obtained with the combination of a medium with two reflectors. Optical reflectors are mirrors. It is interesting to note that this device was invented 100 years ago - well before the development of any serious optical network. Another fundamental resonator is the ring. Some people would argue that the ring resonator is itself a special case of a Fabry-Perot. The ring can be easily integrated on a chip, since it does not require any mirror. All optical resonators could be seen as combinations of a variety of ring and Fabry-Perot resonators. In this thesis, we introduce a novel resonator that we call a Semi Ring Fabry-Perot (SRFP) resonator. Besides combining the advantages of a ring resonator and a Fabry-Perot resonator in a single resonator, the SRFP has unique features and exhibits several advantages over other resonators. The advantages of an SRFP resonator over a Fabry-Perot are:

- The reflection field of an SRFP has a greater finesse than the Fabry-Perot resonator.
- The SRFP can be integrated on a chip more easily than a Fabry-perot.
- The length of an SRFP resonator is not correlated with that of the chip, in contrast to the case of a Fabry-Perot. This means that in an Integrated Optical

Device, the periodicity of the spectrum responses of SRFP resonators are not correlated. However in the case of a Fabry-Perot they are.

- The SRFP resonator does not interrupt the main waveguide.
- It is easier to fabricate a symmetrical SRFP since its two arms are ended by the same facet.

There are several advantages of an SRFP resonator over a ring resonator:

- The SRFP supports waves propagating in both directions (standing waves). This allows the resonator to transmit and reflect at the same time. However, in the case of a waveguide coupled to a ring resonator there is no standing wave and therefore no reflected light.
- For the same free-spectral range, an SRFP could be fabricated more compact than a ring resonator.
- The SRFP exhibits higher delay time than similar Fabry-Perot and ring resonators.

In this thesis we will study, design, fabricate, and test different SRFP resonators. We will also introduce and study some applications of the SRFP resonator. We will also propose some novel optical devices (tunable lasers and a tiltmeter) requiring planar fabrications.

1.1 The Fabry-Perot: An archetype resonator

The most basic type of optical resonator is the Fabry-Perot cavity resonator, which is the archetype of optical devices. The Fabry-Perot cavity is comprised of two parallel

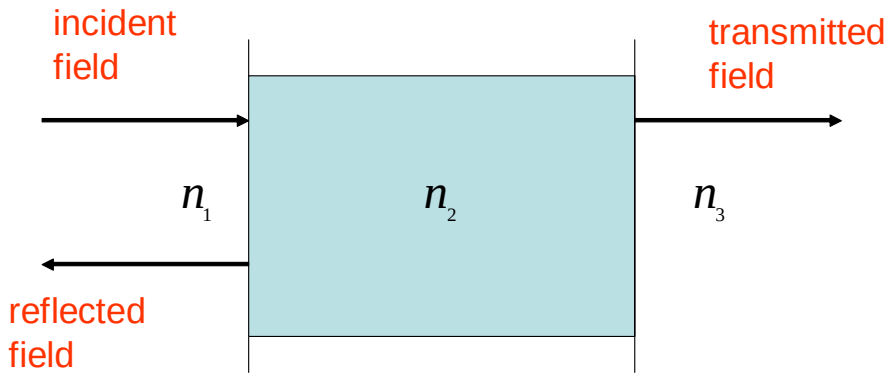

Figure 1.1: Top view of a Fabry-Perot resonator.

reflective planes separated by a distance L, fig. 1.1, [1]. It is nothing else than the optical version of a resonator consisting of a medium confined within two reflectors (which are mirrors in the case of optics). Resonance (constructive interference of the reflected light) occurs at specific wavelengths of light reflected between the two reflective planes when the distance between the planes is an even multiple of the wavelength of the light. Thus, the pattern for resonance is periodic across wavelengths, as shown in fig. 1.2. Fig. 1.2 represents the transmission (fig. 1.2 (a)) and the reflection (fig. 1.2 (b)) spectrum of the Fabry-Perot resonator. The period of the spectrum is called the free spectral range (FSR) and is defined as

$$\text{free-spectral range (FSR)} = \frac{c}{2nL},$$

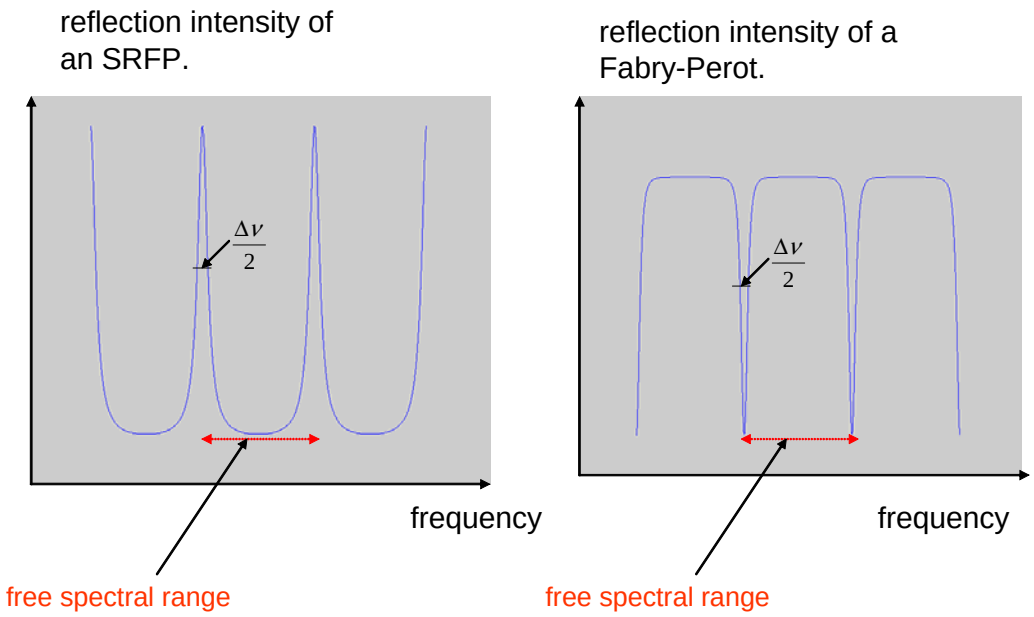

Figure 1.2: Pictures of the transmission and the reflection of the Fabry-Perot resonator, where $\Delta\nu_{1/2}$ is the separation between the two frequencies at which the intensity is down to half of its peak value.

where c is the speed of light, n the index of refraction of the medium, and L the physical length of the medium. The FSR is inversely proportional to the physical length of the medium. That means in order to separate well the modes of the structure, we need to have a relatively high FSR, and therefore a smaller medium length of the medium. Basically, that means the length L of the medium is an important parameter and dictates which the modes of the resonator are. Almost all optical resonators can be modeled as a combination of waveguides and reflectors. Therefore, they can be seen as a combination of different Fabry-Perot resonators. However, the integration of a Fabry-Perot resonator on an integrated chip requires a technically

difficult fabrication. In this case the chip length must coincide with the length of the Fabry-Perot cavity, which determines the FSR of the (transmission, reflection) spectrum intensities. An important parameter used to measure the resolution of a resonator is the finesse, which is defined by

$$finesse = \frac{\Delta\nu_{1/2}}{FSR},$$

where $\Delta\nu_{1/2}$ is the separation between the two frequencies at which the intensity is down to half of its peak value. As illustrated in fig. 1.2, the Fabry-Perot could have an relatively high finesse intensity transmission but has a low finesse reflection transmission. So in summary, the Fabry-Perot exhibits two main disadvantages:

- Difficult integration on a chip.
- Low finesse intensity reflection.

1.2 Ring resonator

One way to improve the integration of a Fabry-Perot resonator on a semiconductor chip is to use a ring resonator, which does not require the use of any cleaved facet, as shown in fig. 1.3. Ring resonators establish resonance in a similar manner to the Fabry-Perot resonator. The critical distance in a ring resonator is defined by the circumference of circular waveguide rather than the separation between two reflective planes as in a traditional Fabry-Perot resonator. The use of ring resonator is often complicated by the need for multiple coupling regions due to the fact that the device can only guide a progressive wave. Indeed in the configuration shown in fig. 1.3 there

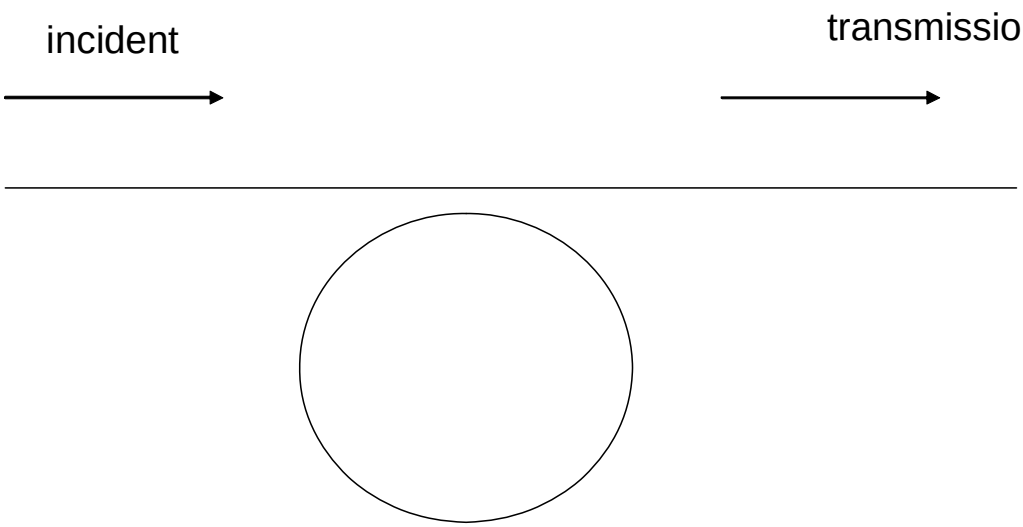

Figure 1.3: Top view of a ring resonator coupled to a waveguide.

is no back reflected field. So in summary the advantage of a ring resonator over the Fabry-Perot is its ease of integration, but its disadvantage is that it does not reflect back any field.

1.3 Grating structures

An alternate solution to the ring and Fabry-Perot resonator is a grating structure, which reflects back light and can be integrated on a chip, [4]. A grating structure is a structure where the refractive index varies periodically in the direction of propagation. The effect of the periodic structure is to couple forward and backward waves in the structure. Fig. 1.4 depicts a rectangular grating with period Λ and mark length Λ_m. The field reflectivity per unit length k_g is

$$k_g = \frac{2\Delta n_{eff}}{\lambda_B}\xi = \frac{2(n_{eff,\,r} - n_{eff,\,t})}{\lambda_B}\xi = \frac{2\Gamma(n_1 - n_2)}{\lambda_B}\xi, \tag{1.1}$$

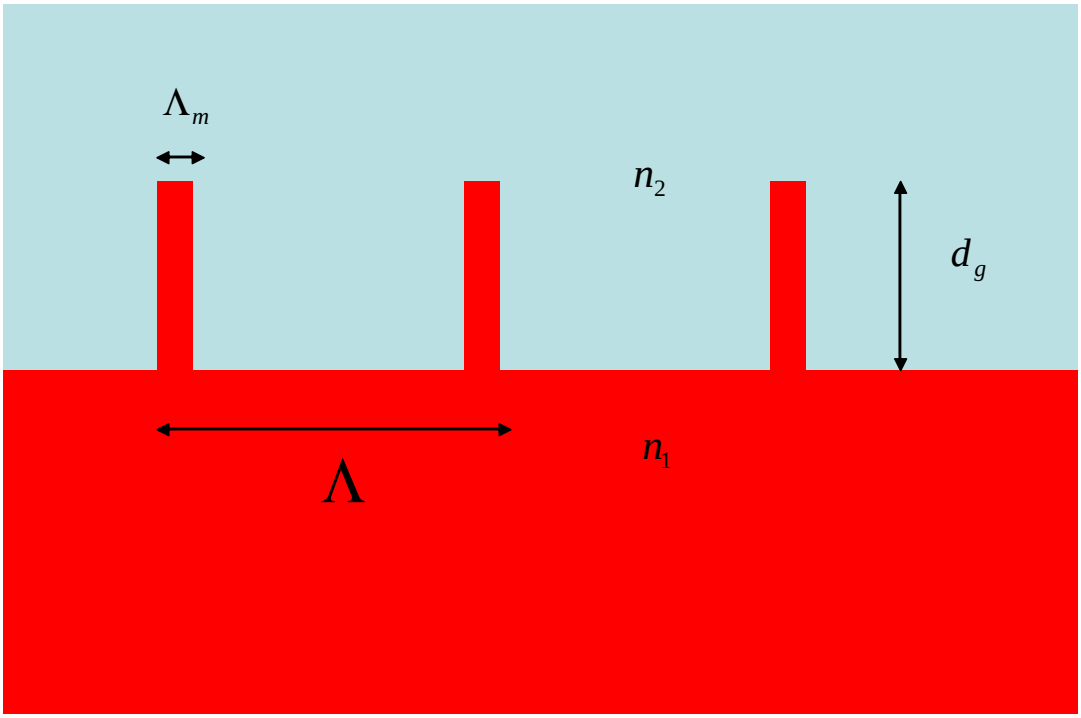

Figure 1.4: Depicts a rectangular grating. Λ is the period of the structure, Λ_m is the mark length, d_g is the grating thickness, n_1 and n_2 the indices of refraction of the materials forming the grating.

where $n_{eff,\,r}$ and $n_{eff,\,t}$ are the refractive indices corresponding to the trench and the ridge regions, where n_1 and n_2 are the refractive indices of the two layers forming the grating, and Γ is the confinement factor for the grating region of thickness d_g, and $\xi < 1$ is the reduction factor. The calculation of Γ assumes replacing the grating structure with an unperturbated layer with a refractive index of $\frac{\sqrt{(n_1^2 - n_2^2)}}{2}$.

1.3.1 Loss in a grating structure

In terms of performance, a planar grating (not a buried structure grating) structure has higher loss than a conventional ridge waveguide. The main reason for that is the

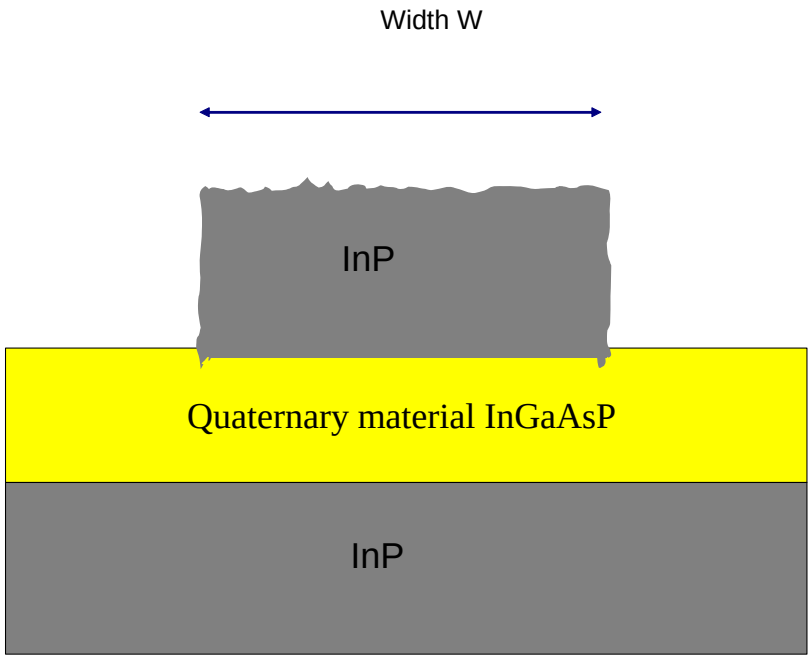

Figure 1.5: Illustration of a ridge waveguide. Since the etching is not perfect, some roughness appears in the contour of the ridge.

roughness of the facet, which scatters the light and therefore causes loss, as shown in fig. 1.5. One may argue that the same phenomenon is happening for any ridge waveguide. However, in the case of a grating, besides having a longitudinal ridge we also have lateral ridges, which increase the loss for the same reason discussed previously. One partial solution would be to design the waveguide in such way that the propagating mode is mostly buried underneath the ridge and not confined within the ridge, fig. 1.6. Even in the case of a shallow-etched ridge, the tail of the mode is still interacting with the side of the ridge, which due to its roughness, scatters some portion of the light. The extreme case would be that the mode is buried in

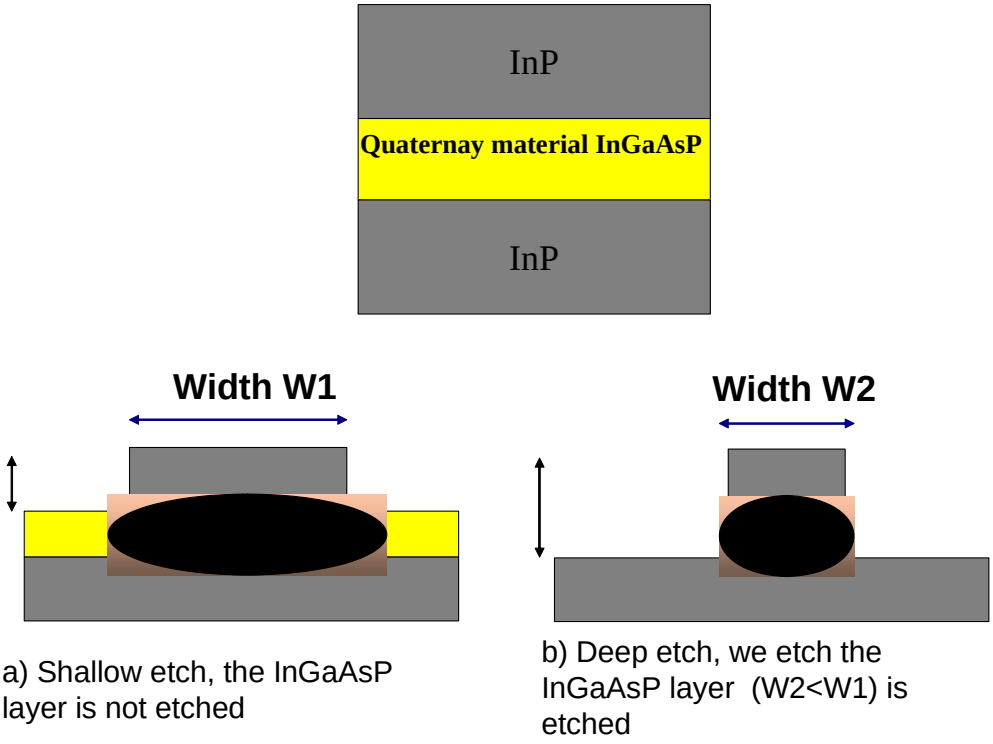

Figure 1.6: Represents the wafer before being etched case A, the ridge waveguide with an shallow etched case B, ridge waveguide with a deep etch case C.

such way that it does not interact anymore with the sidewall of the ridge. But this extreme case is not practical since that would mean that the ridge is not having any role anymore on the lateral confinement of the mode. That would basically mean that we do not have a well-confined guided mode anymore. We also have to keep in mind that the shallower the etching, the less laterally confined is the mode.

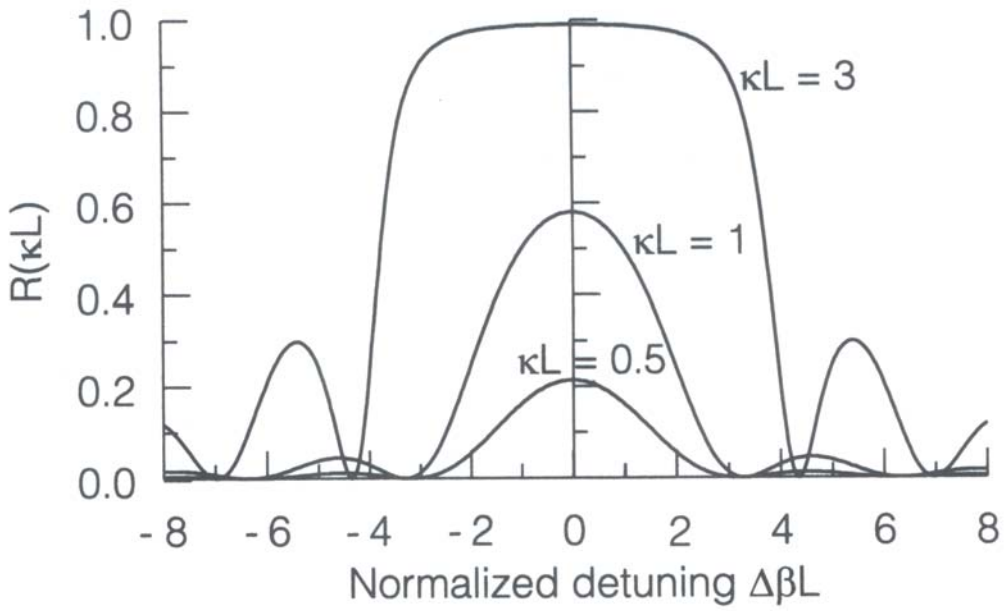

Figure 1.7: Intensity reflectivity as function of $\Delta\beta L$ with kL as parameter [4].

1.3.2 The reflection spectrum of a grating structure

Fig. 1.7 depicts the reflection spectrum grating structures for different values of $k_g L$, where L is the length of the grating. The magnitude of the reflection depends on the value of $k_g L$. For high values of $k_g L$ the grating structure behaves like a stop band. For low values of $k_g L$ the reflection intensity is low and behaves like a sinc function. One of the disadvantages of the Bragg grating is its low resolution (it has a relatively high line width). The line width of the grating reflection spectrum is approximately proportional to k_g. So in order to decrease the line width of the reflection spectrum while having a high magnitude reflection, we would have to decrease k_g and increase the length of the grating. It is shown in equation (1.1) that there are two ways of decreasing k_g and therefore the line width of the reflection spectrum:

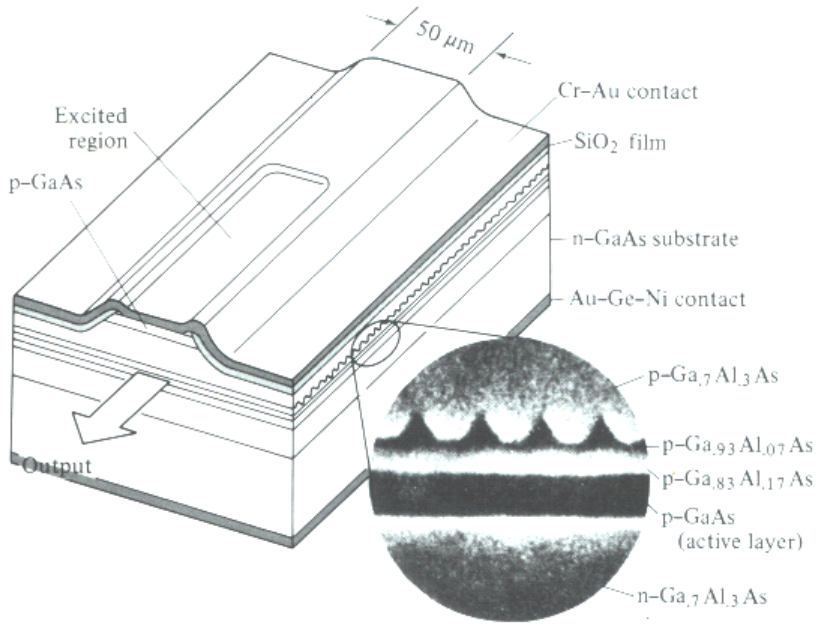

Figure 1.8: A GaAs-GaAlAs cw DFB injection laser with a corrugated interface (grating structures) [6].

- Decreasing $(n_1 - n_2)$, which can be done by having a low index of refraction between the two layers forming the grating structure.
- Decreasing the reduction factor ξ, which can be done by decreasing the duty cycle of the grating.

1.3.3 Buried grating structure

The alternate solution that avoids both the loss and the high line width of the reflection spectrum is to grow the material in such a way that we would have a buried

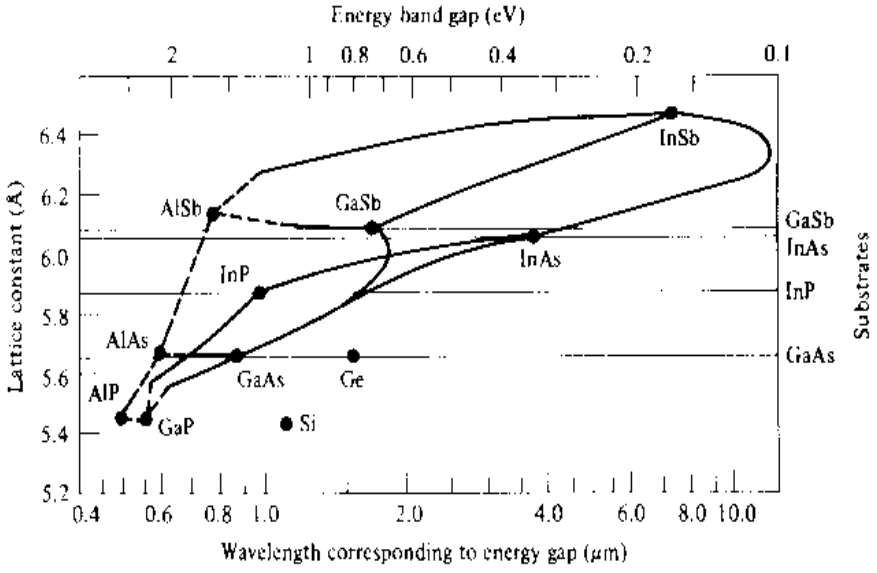

Figure 1.9: III-V compounds: Lattice constants versus bandgap energy and corresponding bandgaps wavelengths. The solid lines correspond to direct-gap materials and the dashed lines to indirect-gap materials. The binary-compound substrates that can be used for lattice-matched growth are indicated on the right, [7].

grating structure, fig. 1.8. This has the advantage of eliminating the roughness of the ridge, since most regrowth techniques introduce some amount of melt-back due to the high growth temperatures. This helps to remove some of the roughness as the new layer is grown. The only roughness that might exist is at the atomic level scale, which is far below the operating wavelength and therefore does not perturb. As far as reducing the line width of the reflection spectrum is concerned, that could be achieved easily by using a buried grating structure, since in that case the difference of indices of refraction of the two layers of material forming the grating structure is lower than compared with the case where the upper material layer is air. Therefore from equation (1.1) k_g is reduced. However, even in good cases the line width of the reflection spectrum of a grating structure is not lower that the FSR of a similar Fabry-Perot. In general a buried structure requires the regrowth of a different material

above an original material layer. The two materials have to be lattice matched. That condition limits the number of materials that can be grown on each other. This technique also has the disadvantages of requiring a very sophisticated fabrication tool, including a sophisticated material growth technique. We should also keep in mind that few materials have the advantage of being lattice matched to another [7]-[16]. One of the major reasons that people have chosen to work with III-V materials is their ability of being lattice matched, see fig. 1.9. Fig. 1.9 shows the lattice constant of some III-V materials. However, the fact that just III-V materials are lattice matched to each other considerably reduces the wavelength range where the device can operate if one would like to use the optical resonator as a passive medium. The medium should be transparent at the operating wavelength. This means that the bandgap of the structure should be bigger than the photon energy, therefore

$$E_g > h\nu = \frac{h\nu}{\lambda},$$

where E_g represents the energy gap, h is the Planck Constant, ν is the frequency and λ is the wavelength. So,

$$\lambda > \frac{h\nu}{E_g} = h\frac{c}{E_g}.$$

Besides, the bandgap is a value that is intrinsic to the material and related to the spacing of the lattice within the material, [17]-[26]. If one would like to use the medium as an active medium, the bandgap must be equal or slightly smaller than the photon energy,

$$E_g = h\nu = h\frac{c}{\lambda}.$$

One advantage of III-V materials such as GaAs, or InP based substrates is that their bandgaps correspond to the energy level that is used in WDM applications. However, even though most of today's optical applications are related to WDM, this does not mean that optics is only restricted to applications related to communication.

Indeed, other ranges of wavelength different from the ones used for WDM could be interesting in applications such as spectroscopy of different gazes. In other words, there are ranges of wavelength, which are not yet used but might be useful in the future for applications which are not yet known. Since it would be hard to proceed to epitaxial growth for some ranges of wavelength that are different than the ones of WDM. Therefore one may not be able to use the grating structures optimally in these situations. In summary, a planar grating structure exhibits a high difference of refraction indices between the layer forming the grating and the cladding layer, which is air. That results in a high value of k_g, which results in a low resolution (high line width) reflection spectrum of the grating structure. In addition, a planar grating structure exhibits higher scattering loss than a ridge waveguide having similar transversal dimensions. An alternate solution is to use a buried grating structure, where the indices of refraction between the two material layers forming the grating are very close to each other. This technique has the disadvantages of requiring very sophisticated fabrication tools and procedure. It also reduces the fabrication of the grating structure to a group of materials that are more or less lattice matched. The energy bandgaps of these materials define the range of wavelength where the buried grating structure could operate. To summarize, in order for a grating structure to be efficient, we need to have a buried structure, which could be fabricated with a restricted number of materials and requires difficult fabrication tools and steps. It is also very difficult to obtain a low line width reflection spectrum from a grating.

Chapter 2

Analysis of Hypothetical Alternate Solutions to the Conventional Optical Structures

Before introducing our device, we analyze in this chapter some structures based on the combinations of devices that we studied earlier and that might seem to be able to solve the disadvantages and weakness of grating structures, Fabry-Perot, and ring resonators used alone.

2.1 Integration of a Fabry-Perot resonator on a chip in parallel with a waveguide

As we discussed earlier, one disadvantage of a Fabry-Perot is the difficulty of integration on a chip due to its facets. Some attempts have been made to use a Fabry-Perot

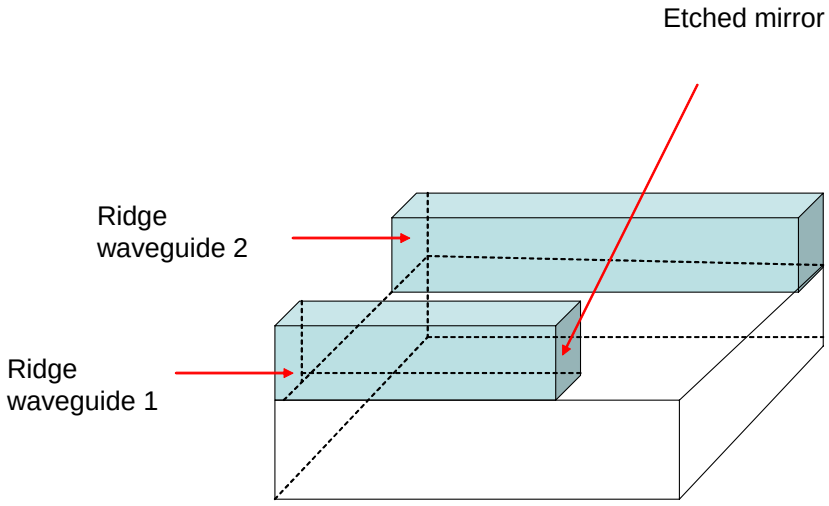

Figure 2.1: Coupled Fabry-Perot resonator.

resonator in parallel with a waveguide at different lengths on the same chip, fig. 2.1. However, this sort of structure required a sophisticated etching process, [2]. Also, in the case where the distance between the two cavities is in the order of magnitude of the wavelength, the modes propagating are not the modes of one resonator filtered out by the other resonator but rather the mode(s) of the structure composed of the combination of the two resonators. These modes are called the supermodes, [2], [3]. One solution would be to implement the Fabry-Perot resonator on the same waveguide that initially supports the light. The only way to obtain such a Fabry-Perot resonator would be to avoid fabricating the reflector facets of the Fabry-Perot resonator by just cleaving the chip. Otherwise the waveguide, which initially is sup-

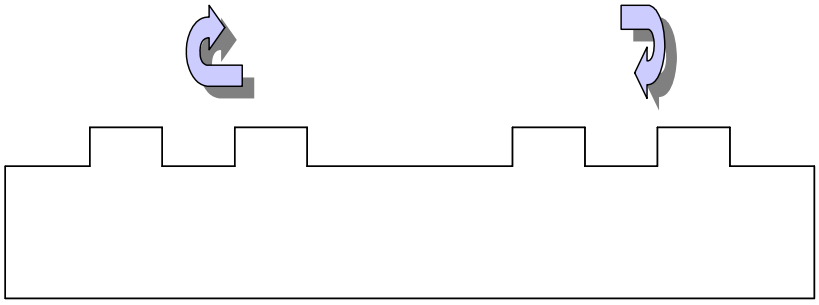

Figure 2.2: Crossing view of a Fabry-Perot resonator obtained by the use of grating structures as reflectors.

posed to support the light, would not be on a single chip anymore since it would be interrupted by the cleaved facets. We could, however, use an optical resonator as reflector for the Fabry-Perot resonator. Since the Fabry-Perot has two reflectors, we would need to have at least two resonators. One way would be to use a grating structure as reflectors, fig. 2.2. An additional problem is that we would have to fabricate a nonplanar structure that requires sophisticated techniques of etching and material growth, [8], fig. 1.3.

2.2 Ring resonator and combinations

One way to improve the integration of a Fabry-Perot resonator on a semiconductor chip is to use a ring resonator that does not require the use of any cleaved facet, fig. 1.3. Both types of optical resonators (Fabry-Perot and ring resonators) have been used in a vast number of various optical devices such as tunable lasers. However, both types present different manufacturing and design challenges. The use of ring resonators is often complicated by the need for multiple coupling regions due to the fact that the device can only guide progressive waves. Indeed, in the configuration shown in fig. 1.3 there is no back reflected field. One solution to this problem is

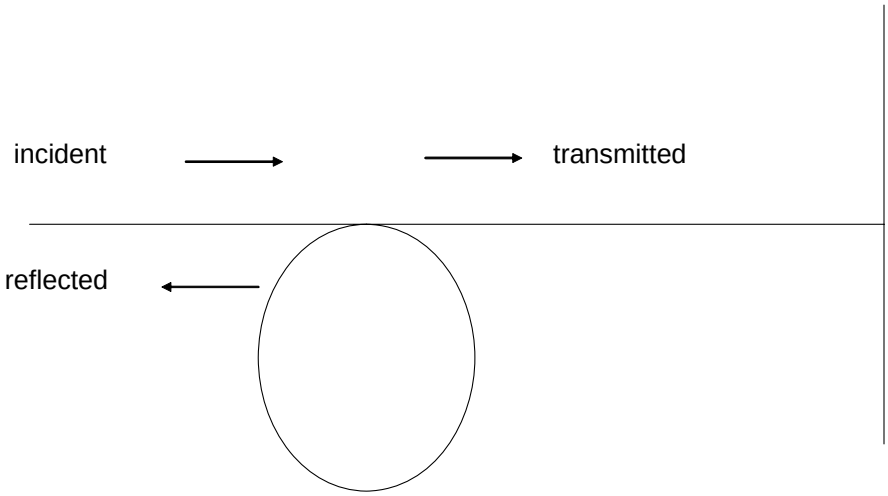

Figure 2.3: Top view of a ring resonator coupled to a waveguide terminated with a mirror.

to add a mirror, which would reflect back to the ring resonator the field that has been transmitted, fig. 2.3. However, in this case we would face the same issue as with Fabry-Perot resonators: to have a mirror in the direction of propagation of light fabrication required either cleaving the facet or adding some nonplanar filter such as gratings. Both cases are complicated to fabricate. Despite these issues of fabrication we propose looking at the device from a theoretical standpoint. Fig. 2.4 is a diagram of the spectrum of a reflected light of the structure shown in fig. 1.3. The reflected light has low finesse and its pattern is similar to the one of the Fabry-Perot resonator. In many cases, for devices such as lasers it is more convenient to

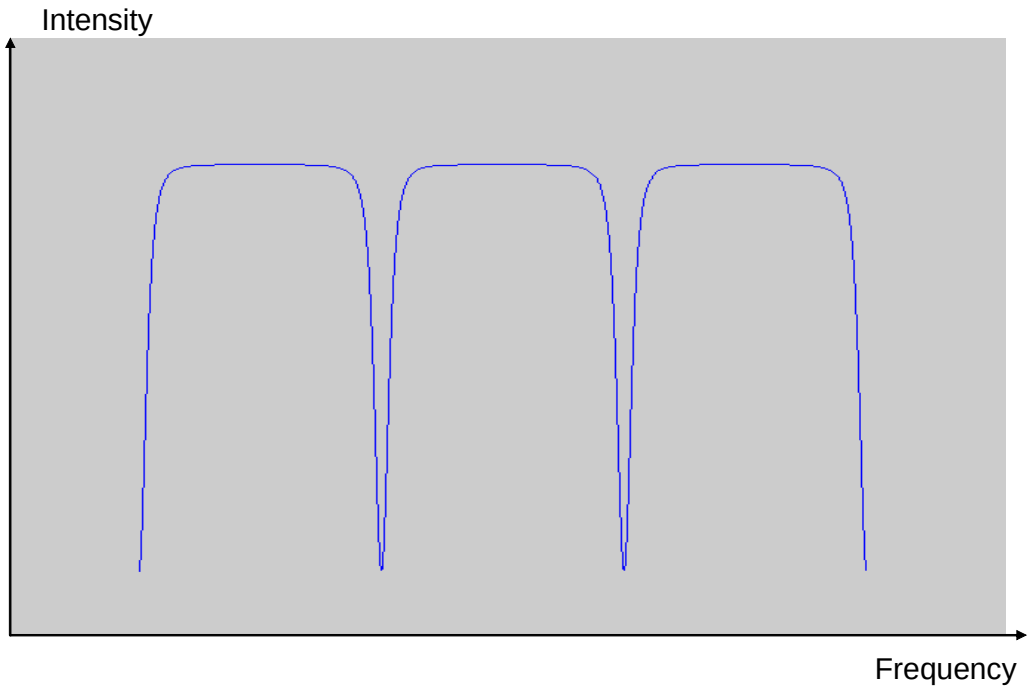

Figure 2.4: Reflected light intensity spectrum of a ring resonator with a reflector shown in fig. 2.3.

have a reflection with high finesse. An alternate solution to this problem would be to have the configuration of fig. 2.5. In this case, in addition to the structure of fig. 1.3, we would have a Y junction, two couplers, and possibly two absorption regions, which would absorb the light and prevent it from being coupled back to the ring resonator. In summary, we would ideally like a resonator to have:

1. A reflection pattern that has high finesse.

2. Ease of fabrication: a planar structure and no mirror interrupting the waveguide in the main direction of propagation. The novel resonator that we

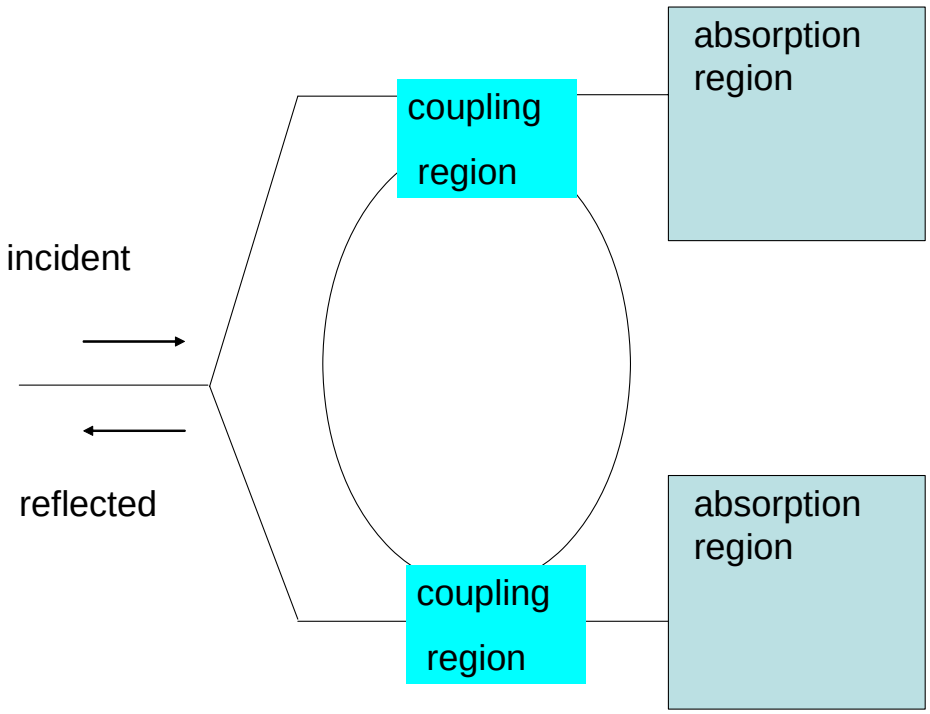

Figure 2.5: Top view of a structure obtained by the combination of a Y junction and two coupling regions and two absorption regions.

propose in the next chapter fulfills these requirements.

Chapter 3

Introduction to the Semi-Ring Fabry-Perot Resonator

Here we propose a new resonator, [27]-[38]. This optical resonator, hereafter referred to as a Semi-ring Fabry-Perot (SRFP) resonator, consists of a medium including an edge forming a reflective facet and a waveguide within the medium, the waveguide having opposing ends formed by the reflective facet, fig. 3.1. The High reflection facet should be located such way where it does not interrupt the main waveguide, otherwise it is not an SRFP resonator. That means that the high reflection facet (HR) of the SRFP resonator should not interact with the main waveguide.

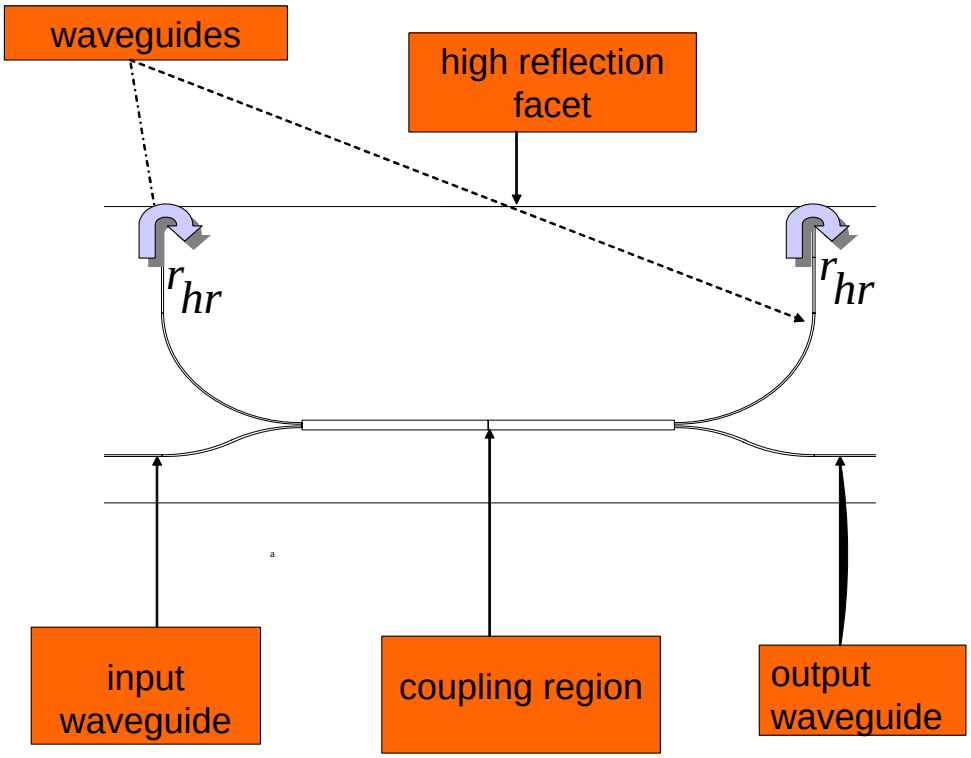

Figure 3.1: Top view of an SRFP resonator.

3.1 Advantages of the SRFP resonator (over a conventional ring or Fabry-Perot resonator)

3.1.1 Advantages of the SRFP resonator over a ring resonator

Some advantages of the SRFP resonator over a conventional ring resonator are that

- The SRFP resonator supports standing waves, which allows having a reflected intensity in addition of the transmitted intensity, whereas in the case of the

ring resonator there is just a transmitted intensity.

- In the case of a ring resonator and an SRFP resonator having the same length, the same loss, and the same coupling region, the transmission intensity of the SRFP would have a higher extinction ratio. The extinction ratio is the ratio of the power at its maximum over its power at its minimum. For the same free-spectral range, an SRFP will be more compact than a ring resonator.

- In transmission even without any loss the SRFP transmission spectrum exhibits resonant modes, whereas in the case of a ring resonator without any loss, the transmission spectrum is a flat band.

3.1.2 Advantages of the SRFP resonator over a Fabry-Perot resonator

The advantage of the SRFP resonator over a conventional Fabry-Perot cavity resonator is the use of one plane mirror for both reflecting facets. This simplifies the fabrication of the resonator, whose length now can greatly differ from that of the chip. Thus the Free Spectra Range of the SRFP resonator is not strongly dictated by fabrication requirements, as in the case of conventional Fabry-Perot resonators. It can be seen in fig. 3.2 that the reflected light spectrum of the SRFP resonator is much narrower than a similar conventional Fabry-Perot, implying higher finesse.

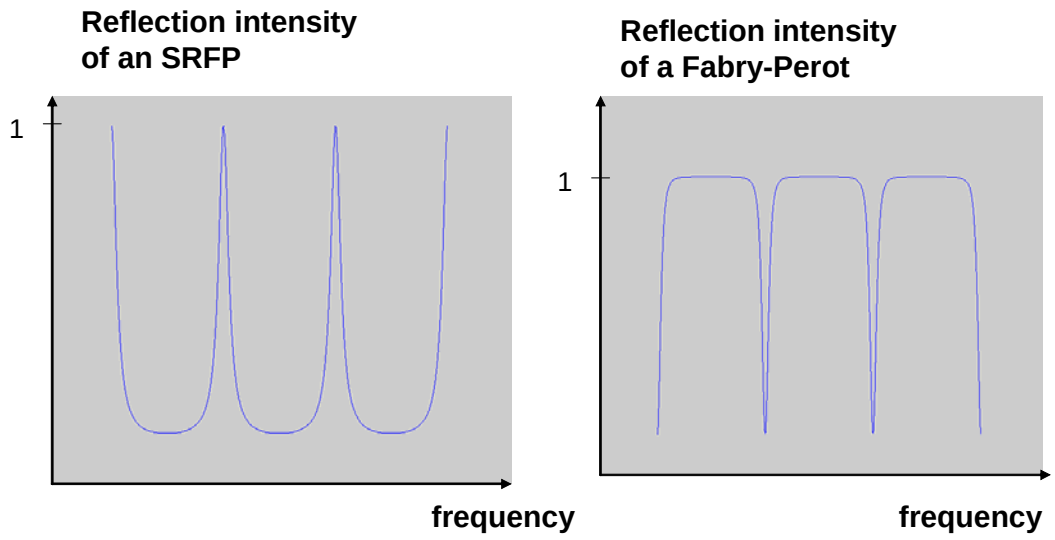

Figure 3.2: Representation of the reflection of an SRFP resonator and that of a Fabry-Perot resonator.

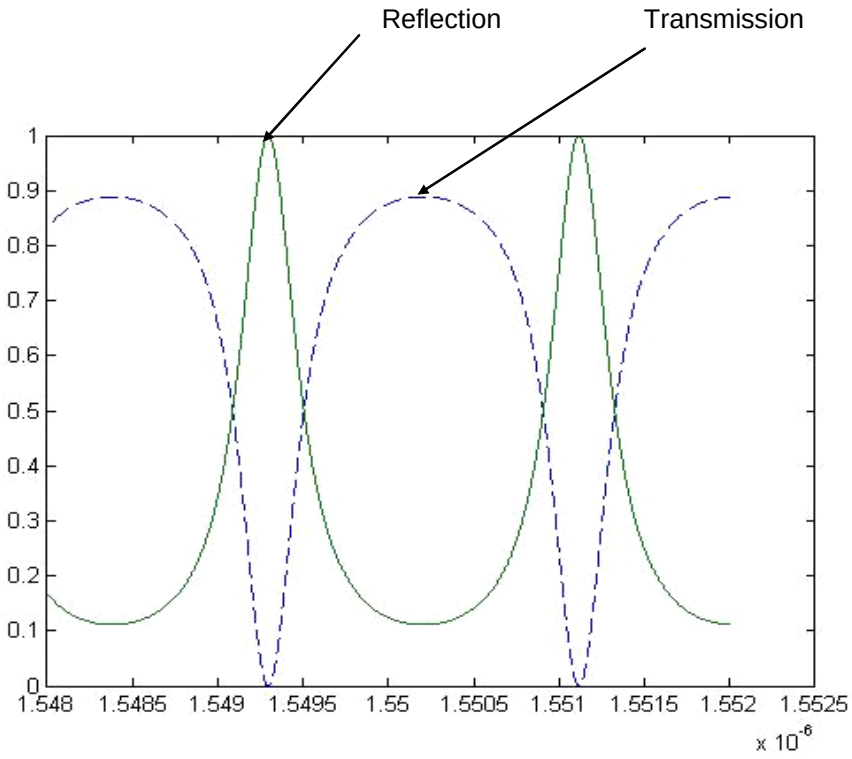

Figure 3.3: Reflection and transmission light spectrum of an SRFP resonator with a 3 dB coupler versus wavelength.

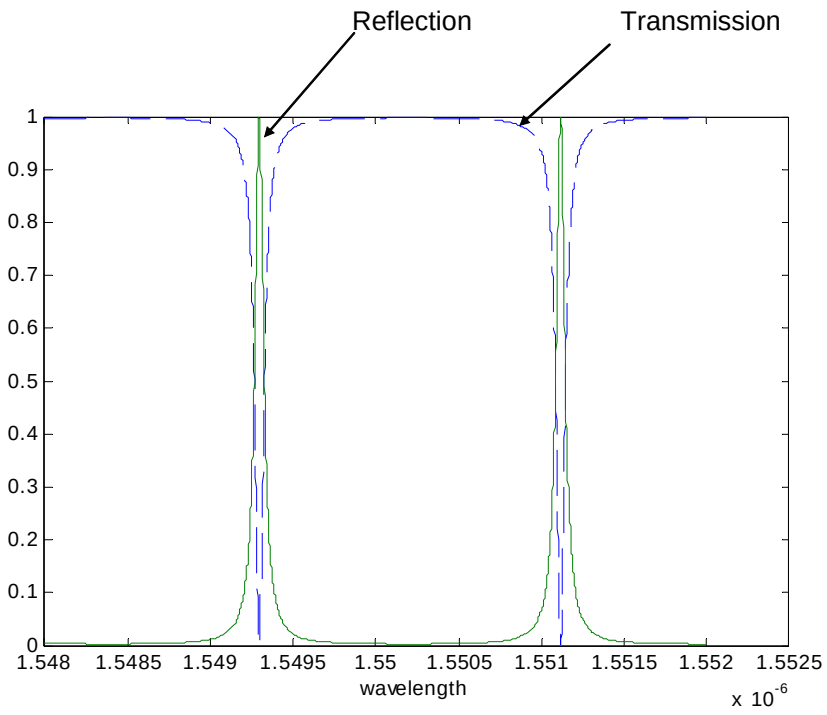

Figure 3.4: Reflection and transmission light spectrum of an SRFP resonator with low coupling.

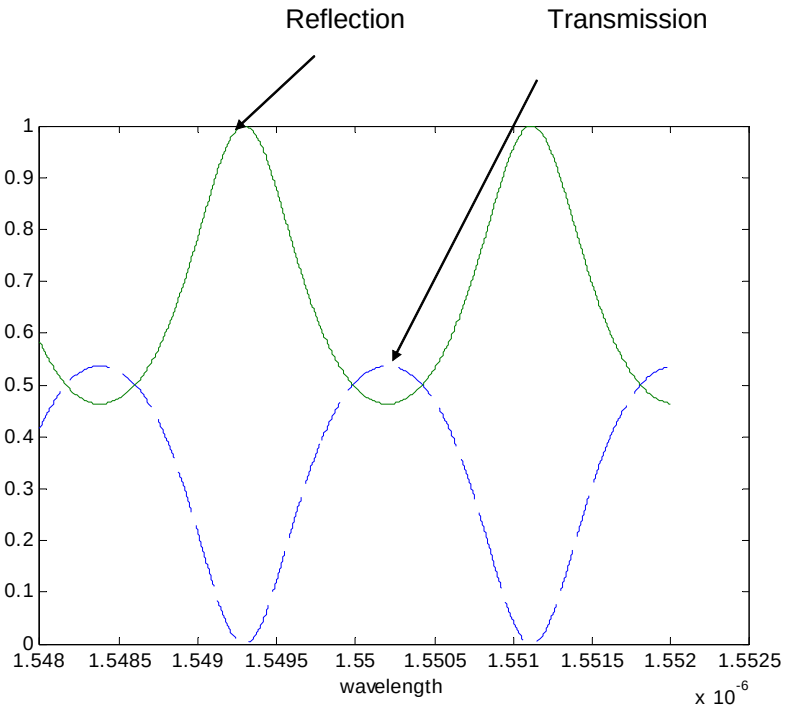

Figure 3.5: Reflection and transmission light spectrum of an SRFP resonator with high coupling ($k = j.0.9$).

Chapter 4

Different Examples of NonSRFP Resonators

In this chapter we analyze some structures that might seem to be similar to an SRFP resonator but behave differently. Fig. 4.1 is an example of a device that is not an SRFP resonator. The distinguishing feature of the SRFP resonator is the HR facet being parallel to the main waveguide making the fabrication easy; there is no interaction with the main waveguide and one can get a reflected light that has high finesse.

4.1 Discussing the case where the HR facet is interacting with the main waveguide

We here basically are comparing the case of fig. 3.1 and fig. 4.1. At first glance the structure of fig. 3.1, which we call an SRFP resonator and the structure of fig. 4.1 that is not an SRFP resonator, might seem similar.

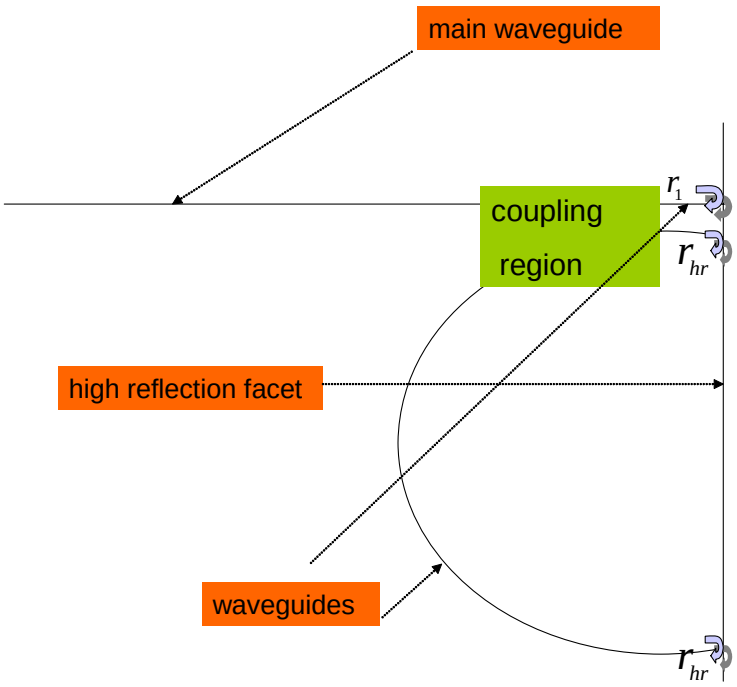

Figure 4.1: Representation of a device in which the HR facet is interacting with the main waveguide. Hence, this device is not an SRFP resonator.

- In the case of the SRFP resonator the HR facet is not interacting with the main waveguide.

- In the case of the SRFP resonator, neither of the two waveguides, which comprise the SRFP resonator, are brought so close to the main waveguide to disturb the modes of the SRFP resonator and the main waveguide. This is very important because in the case that the distance between the two waveguides is in the order of magnitude of a wavelength, the modes propagating in each waveguide will interfer with the modes of the other waveguide. The modes propagating in the structure obtained by the combination of the two waveguides are no longer

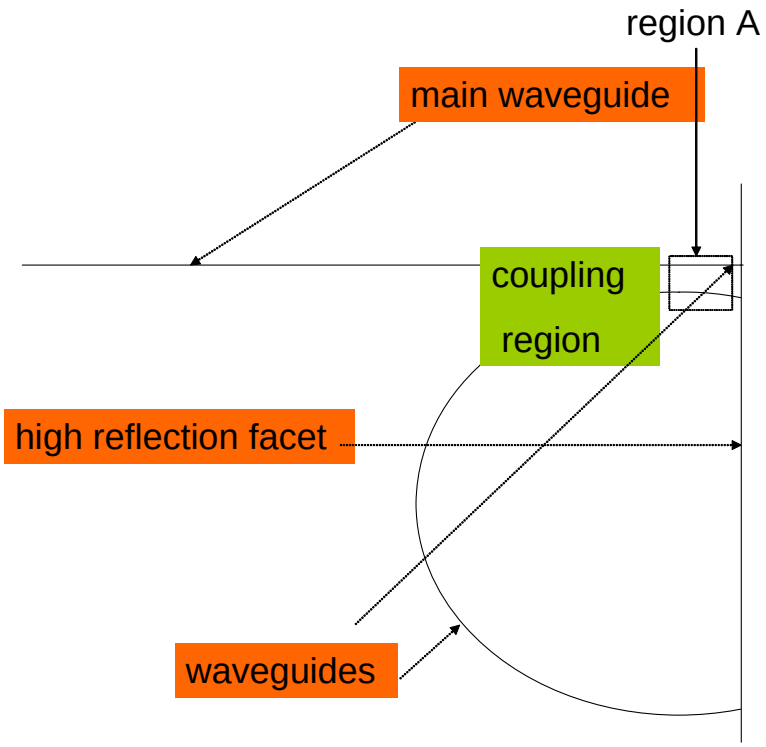

Figure 4.2: Illustration of the fact that in region A the modes of the resonator and those of the waveguide can disturb each other.

the superposition of the modes of each waveguide, but rather the supermodes of the whole structure, [3].

The reflection pattern of the resonator shown in fig. 4.2, 4.3 is additionally dependent on the length of waveguide (1 and 2) as it is in the case of an SRFP resonator; (fig. 3.1 is also depending on the length of waveguide 3, (fig. 4.3). Fig. 4.3 emphasizes the existence of three waveguides 1, 2 and 3 instead of two in the case of an SRFP resonator. Fig. 4.4 represents a structure where in addition to the SRFP resonator we interrupt the main waveguide by putting a reflector. Again, in comparing this device (fig. 4.4) with the one shown in fig. 4.2, 4.3 the location of

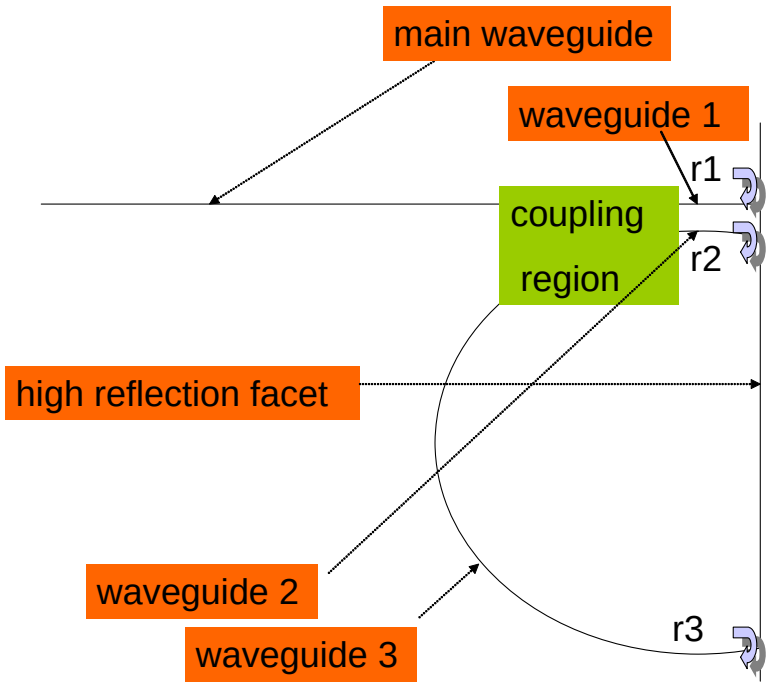

Figure 4.3: Representation of the resonator and emphasizing on the existence of 3 waveguides 1,2 and 3 instead of 2 in the case of an SRFP resonator.

the reflector could be chosen independently from the length of the waveguides within the SRFP resonator. However, we can see that in the case of fig. 4.3 the length of the waveguide 1 depends heavily on the one of waveguide 2. Also in the case of fig. 4.4 we can see that r_1 can be different from r_{hr}; however, in the case of fig. 4.3 $r_1 = r_2 = r_3$, unless very sophisticated fabrication techniques are used.

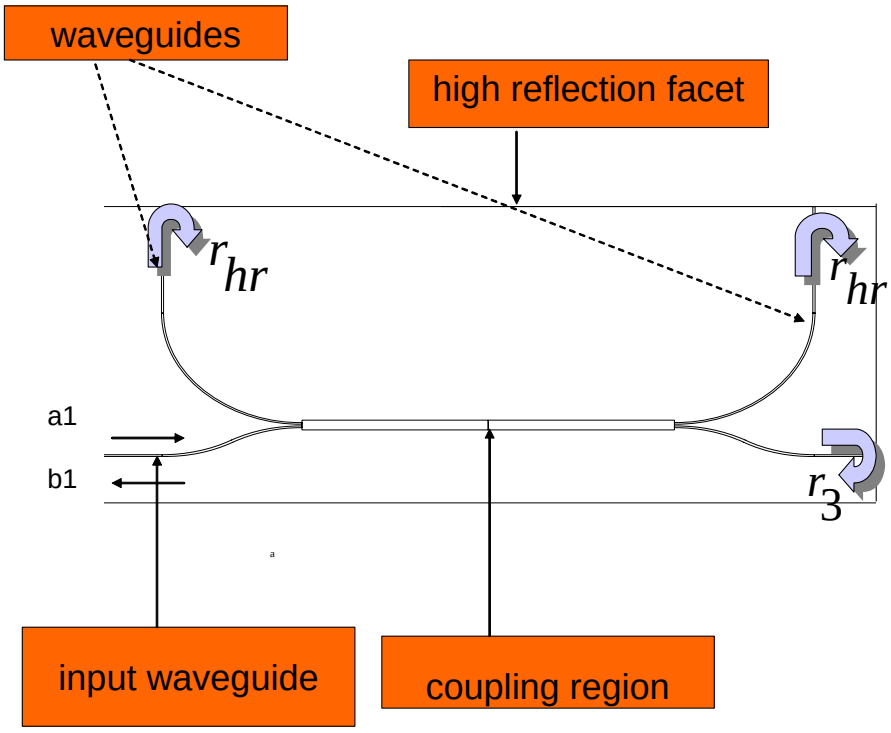

Figure 4.4: Interruption of the main waveguide using a high reflection facet.

Chapter 5

Modeling the Resonator

One would like to model the structure of fig. 5.1, where the a_i are the input fields to the coupling region and the b_i the output fields from the coupling region.

5.1 Modeling the coupling region

Before modeling the whole structure we are going to model the coupling region. We assume that within the coupling region there is no back coupling, i.e., there is no coupling between the forward field and the backward field. Using the same approach as in [39], we analyze the coupling region, where a_i (b_i) are the input (output) normalized complex field amplitude entering and leaving the coupling region. As a result of the assumption that the forward and the reverse fields are not coupled in the coupling region we can separate the forward and the reverse fields as illustrated in figs. 5.2, 5.3.

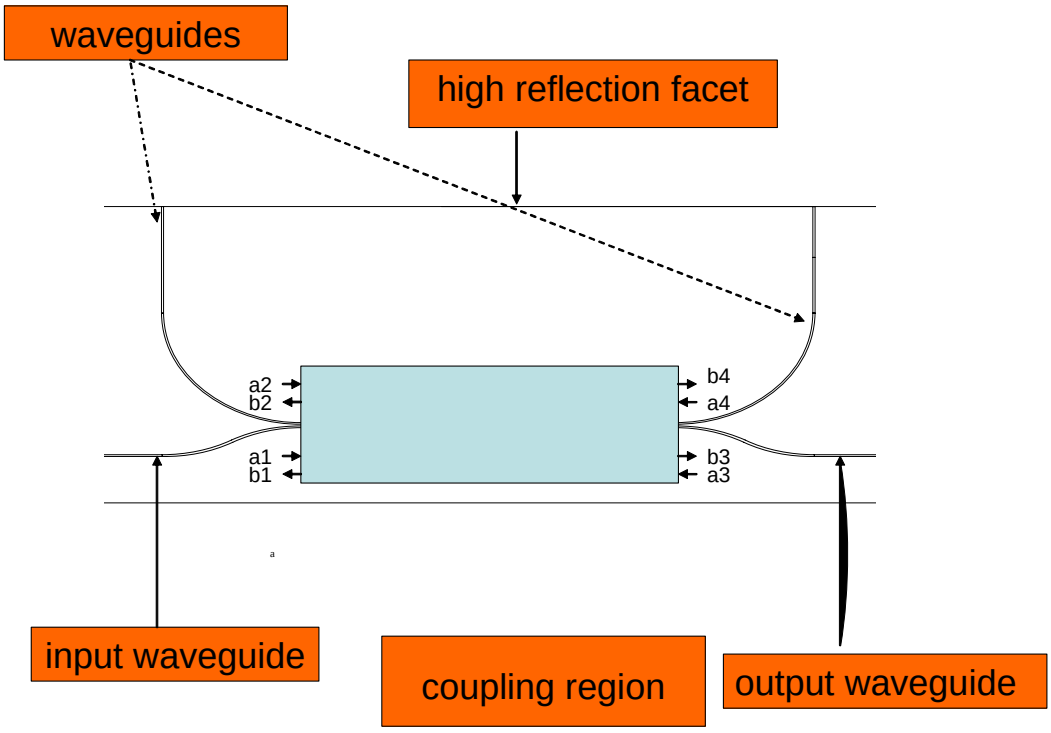

Figure 5.1: Representation of an SRFP resonator with the association of the coupling region.

$$b_1 = 0.a_1 + 0.a_2 + t_1(f).a_3 + k_1(f).a_4, \tag{5.1}$$

$$b_2 = 0.a_1 + 0.a_2 + k_1(f)^{'}a_3 + t_1(f)^{'}a_4, \tag{5.2}$$

$$b_3 = t_2(f)a_1 + k_2(f).a_2 + 0.a_3 + 0.a_4, \tag{5.3}$$

$$b_4 = k_2(f)^{'}a_1 + t_2(f)^{'}a_2 + 0.a_3 + 0.a_4, \tag{5.4}$$

where f is the frequency of the field, $t_1(f)$, $t_1(f)^{'}$, $t_2(f)$, $t_2(f)^{'}$, and $k_1(f)$, $k_1(f)^{'}$,

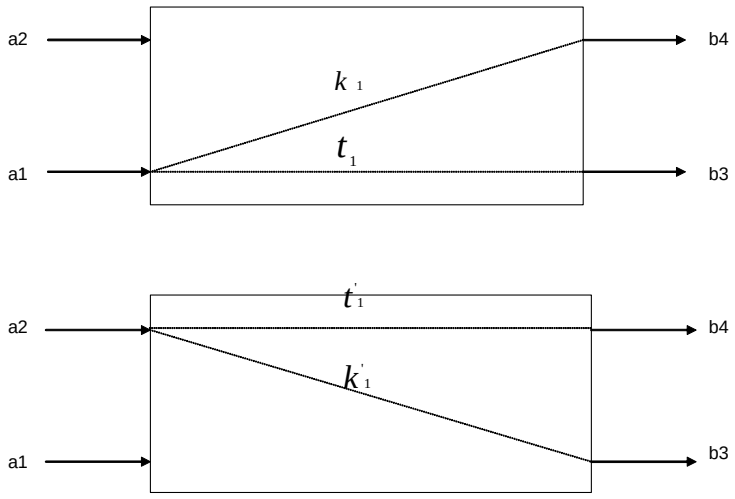

Figure 5.2: Representation of the forward light in the coupling region.

$k_2(f)$, $k_2(f)'$ are the transmission and reflection coefficients of the complex field, respectively. The set of equation (5.1) can be also written in matrix form,

$$\begin{pmatrix} b_1 \\ b_2 \end{pmatrix} = \left\{ M_1 = \begin{pmatrix} t_1(f) & k_1(f) \\ k_1(f)' & t_1(f)' \end{pmatrix} \right\} \begin{pmatrix} a_3 \\ a_4 \end{pmatrix},$$
$$\begin{pmatrix} b_3 \\ b_4 \end{pmatrix} = \left\{ M_2 = \begin{pmatrix} t_2(f) & k_2(f) \\ k_2(f)' & t_2(f)' \end{pmatrix} \right\} \begin{pmatrix} a_1 \\ a_2 \end{pmatrix}.$$

We will first analyze the forward light, illustrated in fig. 5.2. We assume that the

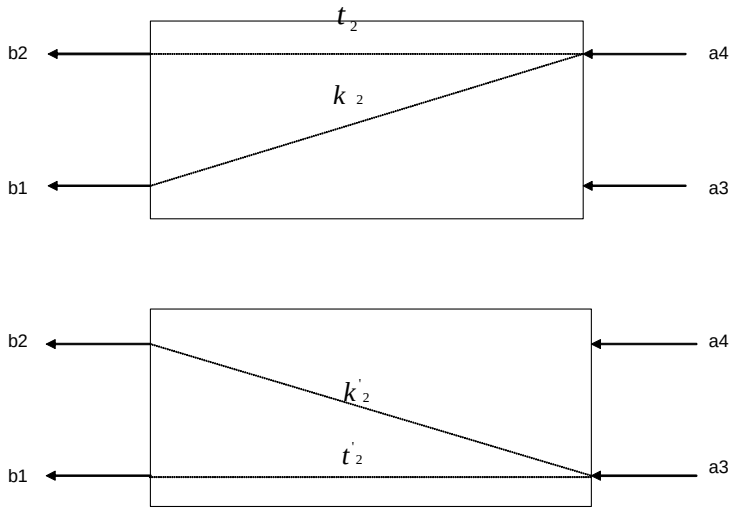

Figure 5.3: Representation of the reverse light in the coupling region.

coupling is lossless, meaning there is conservation of energy between the input light intensity and the output light intensity, expressed by the condition

$$|b_3|^2 + |b_4|^2 = |a_1|^2 + |a_2|^2 \,. \tag{5.5}$$

The condition expressed in equation (5.5) is fulfilled if the matrix M_1 is unitary. This means the columns and rows of M_1 are orthogonal to each other:

$$\begin{aligned} t_1(f)'k_1(f) + k_1(f)'t_1(f) &= 0, \\ t_1(f)'k_1(f)' + k_1(f)t_1(f) &= 0, \end{aligned} \tag{5.6}$$

and

$$\begin{aligned} |t_1(f)|^2 + |k_1(f)|^2 &= 1, \\ \left|t_1(f)'\right|^2 + \left|k_1(f)'\right|^2 &= 1. \end{aligned} \tag{5.7}$$

The conditions expressed in equations (5.6, 5.7) are satisfied either if

$$\begin{aligned} k_1(f)' &= -k_1(f)^*, \\ t_1(f)' &= t_1(f)^*, \end{aligned}$$

then

$$\begin{pmatrix} b_1 \\ b_2 \end{pmatrix} = \begin{pmatrix} t_1(f) & k_1(f) \\ -k_1(f)^* & t_1(f)^* \end{pmatrix} \begin{pmatrix} a_3 \\ a_4 \end{pmatrix}, \tag{5.8}$$

or,

$$
\begin{aligned}
k_1(f)' &= k_1(f)^*, \\
t_1(f)' &= -t_1(f)^*,
\end{aligned}
$$

then,

$$
\begin{pmatrix} b_1 \\ b_2 \end{pmatrix} = \begin{pmatrix} t_1(f) & k_1(f) \\ k_1(f)^* & -t_1(f)^* \end{pmatrix} \begin{pmatrix} a_3 \\ a_4 \end{pmatrix}. \tag{5.9}
$$

5.1.1 Special case where the coupler is symmetric

In the case where the coupler is symmetric as illustrated in fig. 5.4, then,

$$k_1(f) = k_1(f)', \tag{5.10}$$

$$t_1(f) = t_1(f)', \tag{5.11}$$

equation (5.8) combined with the condition expressed in equation (5.10) results in

$$
\begin{aligned}
k_1(f) &= -k_1(f)^* \Rightarrow k_1(f) = \pm j\,|k_1(f)|\,, \\
t_1(f) &= t_1(f)^* \Rightarrow t_1(f) = \pm\,|t_1(f)|\,.
\end{aligned}
$$

If $k_1(f)$ is pure imaginary then $t_1(f)$ is pure real. However, when equation (5.9) is combined with the condition expressed in equations (5.10) we obtain

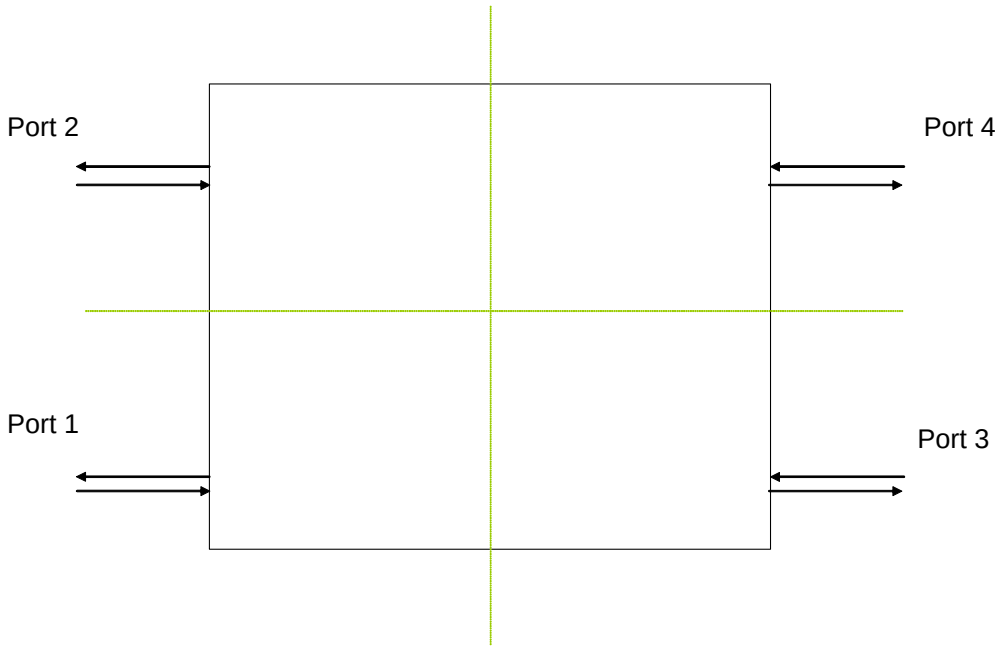

Figure 5.4: Illustration of a symmetrical coupler with respect with the two transversal axes.

$$\begin{aligned} k_1(f) &= k_1(f)^* \Rightarrow k_1(f) = \pm |k_1(f)|\,, \\ t_1(f) &= -t_1(f)^* \Rightarrow t_1(f) = \pm j\,|t_1(f)|\,, \end{aligned}$$

and thus $k_1(f)$ is pure real and $t_1(f)$ pure imaginary.

5.2 Modeling the SRFP resonator

5.2.1 Modeling the reflection and transmission between ports 1 and 3 as illustrated in fig. 5.1

Following the discussion of the last section, we choose to model the coupler region with the following matrix:

$$\begin{pmatrix} b_1 \\ b_2 \end{pmatrix} = \begin{pmatrix} t_1(f) & k_1(f) \\ -k_1(f)^* & t_1(f)^* \end{pmatrix} \begin{pmatrix} a_3 \\ a_4 \end{pmatrix}, \tag{5.12}$$

and the same way we have

$$\begin{pmatrix} b_3 \\ b_4 \end{pmatrix} = \begin{pmatrix} t_2(f) & k_2(f) \\ -k_2(f)^* & t_2(f)^* \end{pmatrix} \begin{pmatrix} a_1 \\ a_2 \end{pmatrix}, \tag{5.13}$$

and furthermore,

$$\begin{aligned} a_2 &= e^{-jkL_2} e^{-\alpha L_2} r_{hr} b_2, \\ a_4 &= e^{-jkL_4} e^{-\alpha L_4} r_{hr} b_4, \end{aligned} \tag{5.14}$$

where r_{hr} is the facet field reflection coefficient, $n_2 L_2$ is the optical length of waveguide 2 , $n_4 L_4$ is the optical length of waveguide 2, α is the absorption coefficient and k is the wave vector. We would like to have the expression for the transmitted light b_3 and reflected light b_1 for a given input light a_1. Therefore, we assume that,

$$a_3 = 0. \tag{5.15}$$

Using equations (5.12, 5.13, 5.14, 5.15), we get

$$\begin{aligned} \frac{b_1}{a_1} &= \frac{k_1 e^{-jkL_4} e^{-\alpha L_4} r_{hr}(-k_2^*)}{1 - t_2^* t_1^* e^{-jkL_2} e^{-\alpha L_2} e^{-jkL_4} e^{-\alpha L_4} r_{hr}}, \\ \frac{b_3}{b_1} &= \frac{t_2 - t_1^* e^{-jkL_2} e^{-\alpha L_2} r_{hr} e^{-jkL_4} e^{-\alpha L_4} r_{hr}}{1 - t_2^* t_1^* e^{-jkL_2} e^{-\alpha L_2} r_{hr} e^{-jkL_4} e^{-\alpha L_4} r_{hr}}. \end{aligned} \tag{5.16}$$

5.2.2 T matrix of the structure

In theory we would like to test the device shown in fig. 3.1. However, in reality we have to test the device shown in fig. 5.5, where in addition to the high reflection facets of the SRFP resonator we also have the facets reflection created at the interfaces of the chip and which are the result of the discontinuity of the index of refraction between the air and the one of the guiding layer. Fig. 5.5 represents the actual device where in addition of the HR facets we also have r_1 and r_3 that are created by the discontinuity in index of refraction between air and the chip. One way of getting rid of r_1 and r_3, would be that the waveguide would have an angle with the facet different than 90°. In order to do so, one simple way would be to use the T matrix formalism, [40]. In order to obtain the T matrix of the structure shown in fig. 5.5, we would have to multiply the T matrices of each "substructure", which are the T matrix of:

- The interface 3 (interface between waveguide 3 and air): $T_{3/air}$
- The waveguide 3: T_3

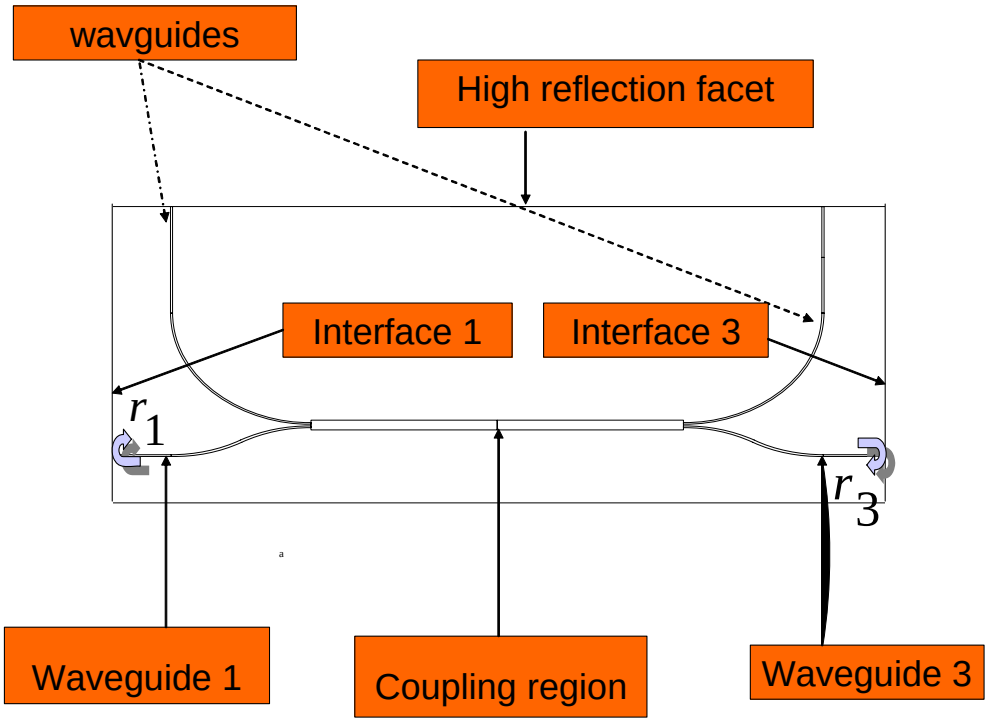

Figure 5.5: Representation of the actual device where in addition of the HR facet we also have reflection resulting from the boundary between the wavguide and air ($r_1$and r_3).

- The SRFP resonator: T_{SRFP}
- The waveguide 1: T_1
- The interface 1 (interface bewteen waveguide 1 and air): $T_{1/air}$

So the T matrix of the structure shown in fig. 5.5 is:

$$T = T_{1/air}T_1T_{SRFP}T_3T_{1/air}.$$

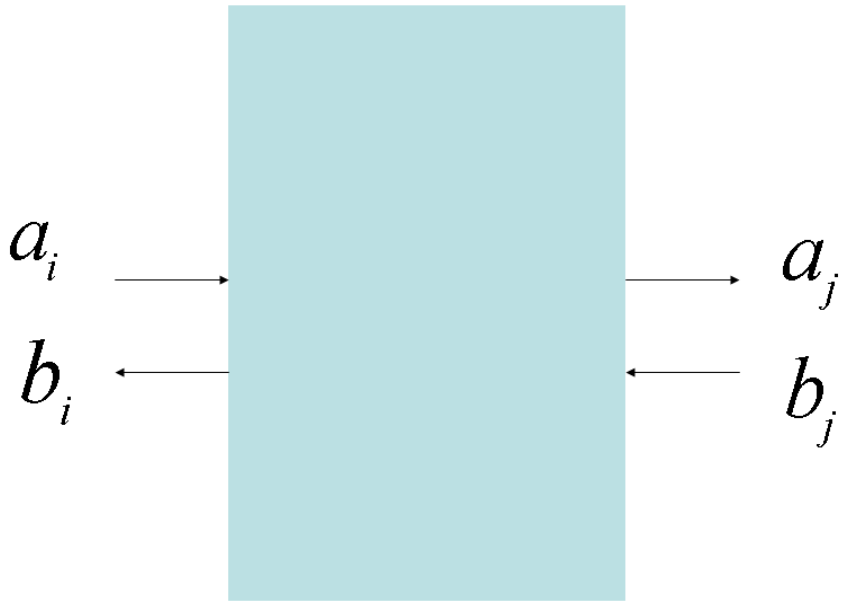

Figure 5.6: Representation of the field flux at port i and port j of an unknown device.

T matrix of the SRFP resonator

In order to write down the expression of the T matrix of the structure shown in fig. 5.5, we need first to define the T matrix of each "substructure" composing the structure of fig. 5.5, and more especially we need to define the T matrix of the SRFP resonator. In general a T matrix is relating the field flux at a certain plane (for example plane 1) to the flux at another plane (for example plane 2), as illustrated in fig. 5.6. The way that the field in port i is related to the field in port j is:

$$\begin{pmatrix} a_i \\ b_i \end{pmatrix} = \begin{bmatrix} T_{ii} & T_{ij} \\ T_{ji} & T_{jj} \end{bmatrix} \begin{pmatrix} a_j \\ b_j \end{pmatrix}. \tag{5.17}$$

In general, for any two-port device the T matrix can be written as

$$T = \frac{1}{t_{ij}} \begin{bmatrix} 1 & -r_{ij} \\ r_{ij} & t_{ij}t_{ji} - r_{ij}r_{ji} \end{bmatrix}, \tag{5.18}$$

where

t_{ij} stands for the transmission coefficient from port i to port j.

t_{ji} stands for the transmission coefficient from port j to port i.

r_{ij} stands for the reflection coefficient of a field entering the device from port i.

r_{ji} stands for the reflection coefficient of a field entering the device from port j.

In the case of an SRFP resonator as shown in fig. 5.5 the ports i and j are respectively the ports 1 and 3. So we need to write down the transmission and reflection coefficients between port 1 and port 3 of the SRFP resonator.

$$
\begin{aligned}
t_{13} &= \left(\frac{b_3}{a_1}\right)_{a_3=0}, \\
t_{31} &= \left(\frac{b_1}{a_3}\right)_{a_1=0}, \\
r_{13} &= \left(\frac{b_1}{a_1}\right)_{a_3=0}, \\
r_{31} &= \left(\frac{b_3}{a_3}\right)_{a_1=0}.
\end{aligned}
$$

T matrix of interfaces 1 and 3 as shown in fig. 5.5

The generic form of the transfer matrix at the interfax of two different media as illustrated in fig. 5.7 is

$$
T = \frac{1}{t_{ij}} \begin{bmatrix} 1 & r_{ij} \\ r_{ij} & 1 \end{bmatrix}, \tag{5.19}
$$

where

- t_{ij} stands for the transmission coefficient from medium i to medium j which is the same as from j to i.
- r_{ij} stands for the reflection coefficient at the interface looking from medium i.

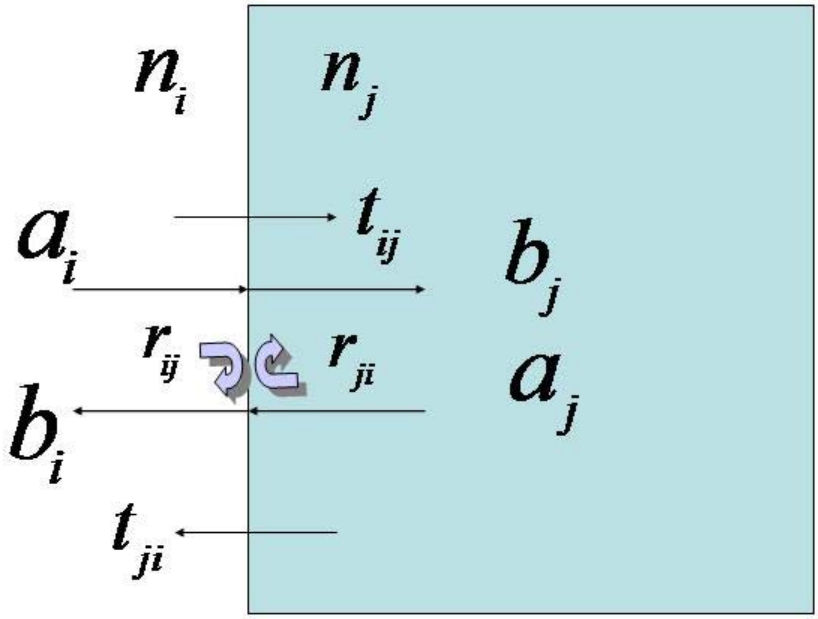

Figure 5.7: Illustration of the interface of two different media (i and j) with respective indexes of refraction n_i and n_j.

- r_{ji} stands for the reflection coefficient at the interface looking from medium j. equation (5.19) is a special case of equations (5.18) where

$$\begin{aligned} r_{ij} &= \frac{n_i - n_j}{n_i + n_j}, \\ t_{ij} &= t_{ji}, \\ |r_{ij}|^2 + |t_{ij}|^2 &= 1. \end{aligned}$$

T matrix of waveguides 1 and 3 as illustrated in fig. 5.5

The generic form of the transfer matrix relating the electromagnetic flux at two different planes distant to each other of a distance L_A is

$$T = \begin{bmatrix} e^{j\Phi_A} & 0 \\ 0 & -e^{j\Phi_A} \end{bmatrix},$$

where

$$\Phi_A = \frac{n_A 2\pi f L_A}{c} + j\alpha_A L_A,$$

is the delay phase happening for a field of frequency f traveling a medium with physical length L_A and index of refraction n_A and loss coefficient α_A. C designates the speed of light.

T matrix of the structure shown in fig. 5.5

Now we can write the T matrix of the whole structure:

$$T = \begin{bmatrix} T_{11} & T_{12} \\ T_{21} & T_{22} \end{bmatrix} = T_{1/air} T_1 T_{SRFP} T_3 T_{1/air}.$$

Using the T matrix we can deduce the reflection and the transmission expression of the structure shown in fig. 5.5, where the reflection coefficient is $\frac{T_{21}}{T_{11}}$ and the transmission coefficient is $\frac{1}{T_{11}}$.

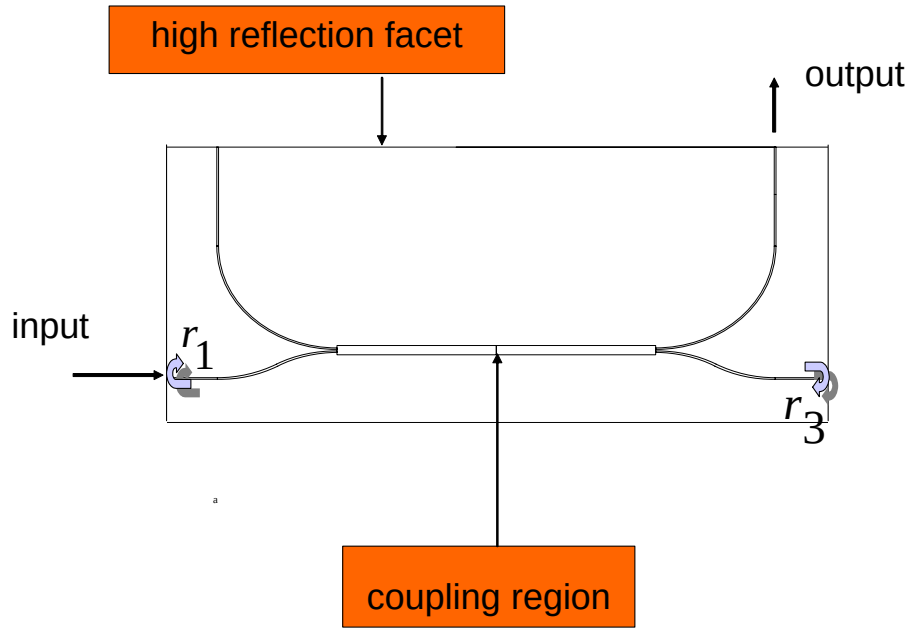

Figure 5.8: Representation of a schematic where the output is located on the side of the high reflection coating.

5.3 Modeling the reflection and transmission between ports 1 and 4

We are examining here the field that gets transmitted through the facets that are supposed to have a high reflection coating, see fig. 5.8. Similar to before we have to write down the T matrix that relates the input to the output as depicted in fig. 5.8. Similarly to the previous case, the T matrix

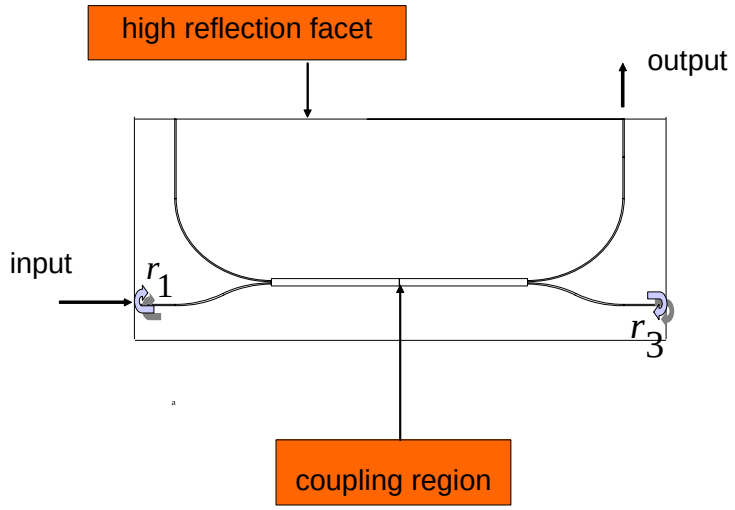

Figure 5.9: Depicts the structure where the input is the field a_1 and the output field is b_4.

$$T = T_{1/air} T_1 T_{Input(1)\_Output(4)} T_4 T_{4/air} \tag{5.20}$$

is composed of different T matrices of subsections, where

- $T_{air/1}$ is the T matrix of interface 1 (interface between air and waveguide 1).
- $T_{Input(1)\_Output(4)}$ is the T matrix of the structure shown in fig. 5.9, where the input is the field $a_1$and the output field is b_4.
- T_4 is the T matrix of waveguide 4.
- $T_{4/air}$ is the T matrix of interface 4 (interface between waveguide 4 and air).

5.3.1 T matrix of the structure depicted in fig. 5.9

We first have to write down

$$\left(\frac{b_4}{a_1}\right)_{a_4=0};$$
$$\left(\frac{b_1}{a_1}\right)_{a_4=0};$$
$$\left(\frac{b_4}{a_4}\right)_{a_1=0};$$
$$\left(\frac{b_1}{a_4}\right)_{a_1=0}$$

in order to describe the T matrix of the structure shown in fig. 5.9. Using the previous equations, we find that:

$$\begin{aligned}
\left(\frac{b_4}{a_1}\right)_{a_4=0} &= -k_1^*(1+\frac{t_1^* t_1 e^{-jkL_2} e_1^{-\alpha L_2} e^{-jkL_3} e^{-\alpha L_3} r_{hr} r_3}{1+k_1 k_1^* e^{-jkL_2} e^{-\alpha L_2} e^{-jkL_3} e^{-\alpha L_3} r_{hr} r_3}, \\
\left(\frac{b_1}{a_1}\right)_{a_4=0} &= t_1 t_2 e^{-jkL_3} e^{-\alpha L_3} r_3 - \frac{t_1 e^{-jkL_3} e^{-\alpha L_3} r_3 k_2 e^{-jkL_2} e_1^{-\alpha L_2} r_{hr} k_1^* e^{-jkL_3} e^{-\alpha L_3} r_3 t_2}{1+k_2 k_1^* e^{-jkL_2} e^{-\alpha L_2} e^{-jkL_3} e^{-\alpha L_3} r_{hr} r_3}, \\
\left(\frac{b_4}{a_4}\right)_{a_1=0} &= t_1^* t_2^* e^{-jkL_2} e^{-\alpha L_2} r_{hr} \left(1 - \frac{k_1^* e^{-jkL_3} e^{-\alpha L_3} r_3 k_2 e^{-jkL_2} e^{-\alpha L_2} r_{hr}}{1+k_2 k_1^* e^{-jkL_2} e^{-\alpha L_2} e^{-jkL_3} e^{-\alpha L_3} r_{hr} r_3}\right), \\
\left(\frac{b_1}{a_4}\right)_{a_1=0} &= \left(\frac{t_1 e^{-jkL_3} e^{-\alpha L_3} r_3 k_2 e^{-jkL_2} e^{-\alpha L_2} r_{hr} t_1^*}{1+k_2 k_1^* e^{-jkL_2} e^{-\alpha L_2} e^{-jkL_3} e^{-\alpha L_3} r_{hr} r_3} + k_1\right).
\end{aligned}$$

Using equation (5.18) which expresses the general form of a transfer matrix between two ports (i and j), we deduce the T matrix of the structure shown in fig. 5.9, which is

$$T = \frac{1}{\left(\frac{b_4}{a_1}\right)_{a_4=0}} \begin{bmatrix} 1 & -\left(\frac{b_1}{a_1}\right)_{a_4=0} \\ \left(\frac{b_1}{a_1}\right)_{a_4=0} & \left(\frac{b_4}{a_1}\right)_{a_4=0}\left(\frac{b_1}{a_4}\right)_{a_1=0} - \left(\frac{b_1}{a_1}\right)_{a_4=0}\left(\frac{b_4}{a_4}\right)_{a_1=0} \end{bmatrix},$$

$$T = \frac{1}{t_{14}} \begin{bmatrix} 1 & -r_{14} \\ r_{14} & t_{14}t_{41} - r_{14}r_{41} \end{bmatrix}.$$

We can write the T structure that relates the inputs to the outputs, fig. 5.8,

$$T = T_{1/air}T_1T_{Input(1)\_Output(4)}T_4T_{4/air} = \begin{bmatrix} T_{11} & T_{12} \\ T_{21} & T_{22} \end{bmatrix}.$$

Chapter 6

Case Where the SRFP Resonator is a Lossless and Symmetrical Resonator

From a theoretical point, it is interesting to study the case where the SRFP resonator is a lossless and symmetrical resonator. The assumption that the resonator is symmetrical is expressed by

- $L_2 = L_4$

and

- The coupling region is symmetrical.

The assumption that the resonator is lossless is expressed by

- The waveguides are lossless,

$$\alpha = 0,$$

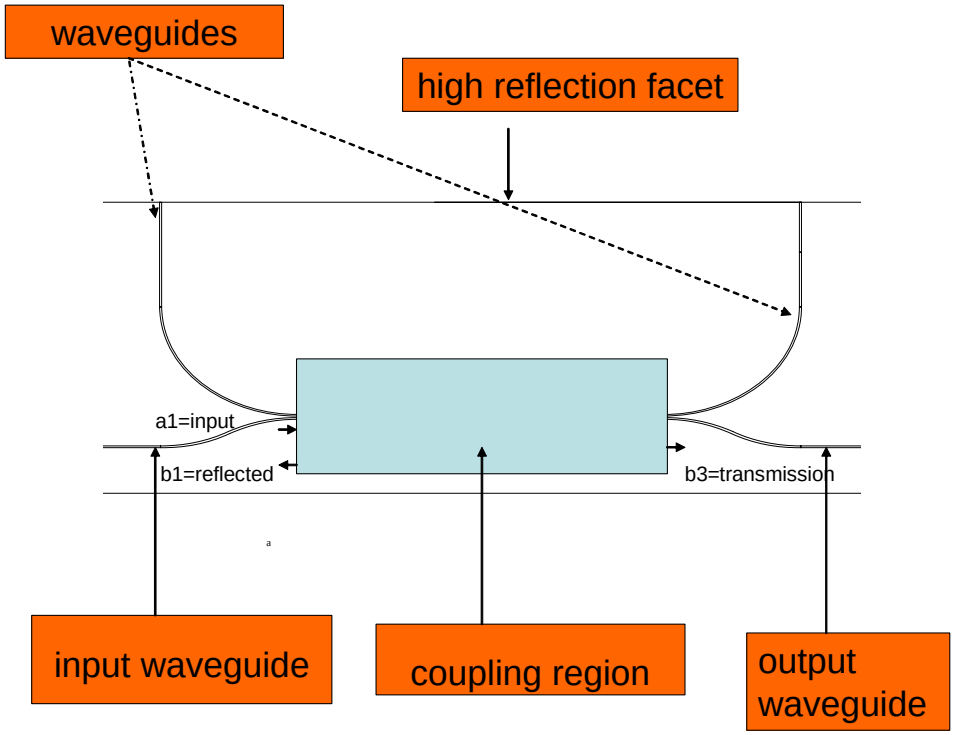

Figure 6.1: Representation of an SRFP resonator where a_1 is the input field, b_3 the transmitted field, and b_1 is the reflected field.

and

- The high reflection facet is perfect, $r_{hr} = 1$.

We choose as the input field of the resonator a_1, the output field b_3, and the reflected field b_1, as shown in fig. 6.1. The reflection coefficient of the structure shown in fig. 6.1 is $\frac{b_1}{a_1}$, and its transmission coefficient is $\frac{b_3}{a_1}$. The scattering matrix that relates the outputs of the device to the input is expressed as

$$S = \begin{bmatrix} r_{13} & t_{13} \\ t_{31} & r_{31} \end{bmatrix},$$

where

$$r_{13} = \left(\frac{b_1}{a_1}\right)_{a_3=0} = \frac{k_1 e^{-jkL_4} e^{-\alpha L_4} r_{hr}(-k_2^*)}{1 - t_2^* t_1^* e^{-jkL_2} e^{-\alpha L_2} e^{-jkL_4} e^{-\alpha L_4} r_{hr}}$$

is the reflection of port 1,

$$t_{13} = \left(\frac{b_3}{a_1}\right)_{a_3=0} = t_2 + \frac{-k_2 t_1^* k_2^* e^{-jkL_2} e^{-\alpha L_2} r_{hr} e^{-jkL_4} e^{-\alpha L_4} r_{hr}}{1 - t_2^* t_1^* e^{-jkL_2} e^{-\alpha L_2} e^{-jkL_4} e^{-\alpha L_4} r_{hr}}$$

is the transmission from port 1 to port 3,

$$r_{31} = \left(\frac{b_3}{a_3}\right)_{a_1=0} = \frac{k_2 e^{-jkL_2} e^{-\alpha L_2} r_{hr}(-k_1^*)}{1 - t_2^* t_1^* e^{-jkL_2} e^{-\alpha L_2} e^{-jkL_4} e^{-\alpha L_4} r_{hr}}$$

is the reflection of port 3,

$$t_{13} = \left(\frac{b_1}{a_3}\right)_{a_1=0} = t_1 + \frac{-k_2 t_1^* k_2^* e^{-jkL_2} e^{-\alpha L_2} r_{hr} e^{-jkL_4} e^{-\alpha L_4} r_{hr}}{1 - t_2^* t_1^* e^{-jkL_2} e^{-\alpha L_2} e^{-jkL_4} e^{-\alpha L_4} r_{hr}}$$

is the transmission from port 3 to port 1. Assuming that the combination of the SRFP resonator and the coupling region is lossless, it signifies that the scattering matrix of the structure is unitary. In addition the assumption that the resonator is symmetrical means that the transmission and reflection coefficient of fig. 6.1 are the

same that the ones of fig. 6.2, which represents the SRFP resonator where a_3 is the input field, b_1 is the transmitted field, and b_3 is the reflected field. Therefore, the scattering matrix can be written either in the two following forms:

$$S = \begin{bmatrix} r & t \\ -t^* & r^* \end{bmatrix} = \begin{bmatrix} r_{13} & t_{13} \\ t_{31} & r_{31} \end{bmatrix},$$

where $t_{13} = t, t_{31} = -t^*$ and $r_{13} = r, r_{31} = r_{13}^*$.

Since we know that our device is symmetrical then $r_{13} = r_{31}$ and $t_{13} = t_{31}$. That means $t = -t^*$ and $r = r^*$.So

$$\begin{aligned} r_{13} &= r_{31} \in \mathbb{R}, \\ t_{13} &= t_{31} = \pm j \left| t_{13} \right|, \end{aligned}$$

- $$S = \begin{bmatrix} r & t \\ t^* & -r^* \end{bmatrix} = \begin{bmatrix} r_{13} & t_{13} \\ t_{31} & r_{31} \end{bmatrix},$$

where $t_{13} = t$, $t_{31} = t^*$ and $r_{13} = r$, $r_{31} = -r_{13}^*$. Since we know that our device is symmetrical then $r_{13} = r_{31}$ and $t_{13} = t_{31}$. That means $t = t^*$ and $r = -r^*$. In both cases we can see that there is a difference of phase of $+\frac{\pi}{2}$ between the reflected field and the transmitted one. As illustrated in fig. 6.3 the condition of having a difference of phase between the transmitted and the reflected fields is fulfilled under the condition that the SRFP resonator is a lossless and symmetrical device. Fig. 6.4 represents the difference of phase between the transmitted and the reflected field in the case that the SRFP resonator is symmetrical but not lossless since $R_{hr} = 90\%$.

It can be seen that in the case where the SRFP resonator is symmetrical but not lossless since the high reflection facet is just equal to 90% the difference of phase between the reflected and the transmitted fields could be assumed to be equal to $+\frac{\pi}{2}$. However this phase condition is harder to satisfy as soon as the device deviates from the symmetry condition. That teaches us about the advantage of the SRFP resonator to satisfy the phase condition over any other symmetrical device. Indeed the fact that the difference of phase between the reflected and the transmitted phase is $+\frac{\pi}{2}$ is not intrinsic just to the SRFP resonator but rather to any lossless and symmetrical resonator as long as there is both a transmitted and reflected field. However, the net advantage of the SRFP over any other resonator is its ability to satisfy with a higher degree of accuracy the symmetrical condition. Indeed, in the case of a conventional Fabry-Perot resonator, it is not an easy task to have a symmetrical device since both mirrors should be similar. However in the case of the SRFP resonator we have the mirror for both waveguides, which guarantees with great accuracy the symmetrical condition. In the case of a grating structure, that is even a more complicated task since each period of the grating should be exactly the same. In this thesis, we are not exhibiting different applications for such phase features. However, we are convinced that this specific phase feature of the device is of great use for many different applications.

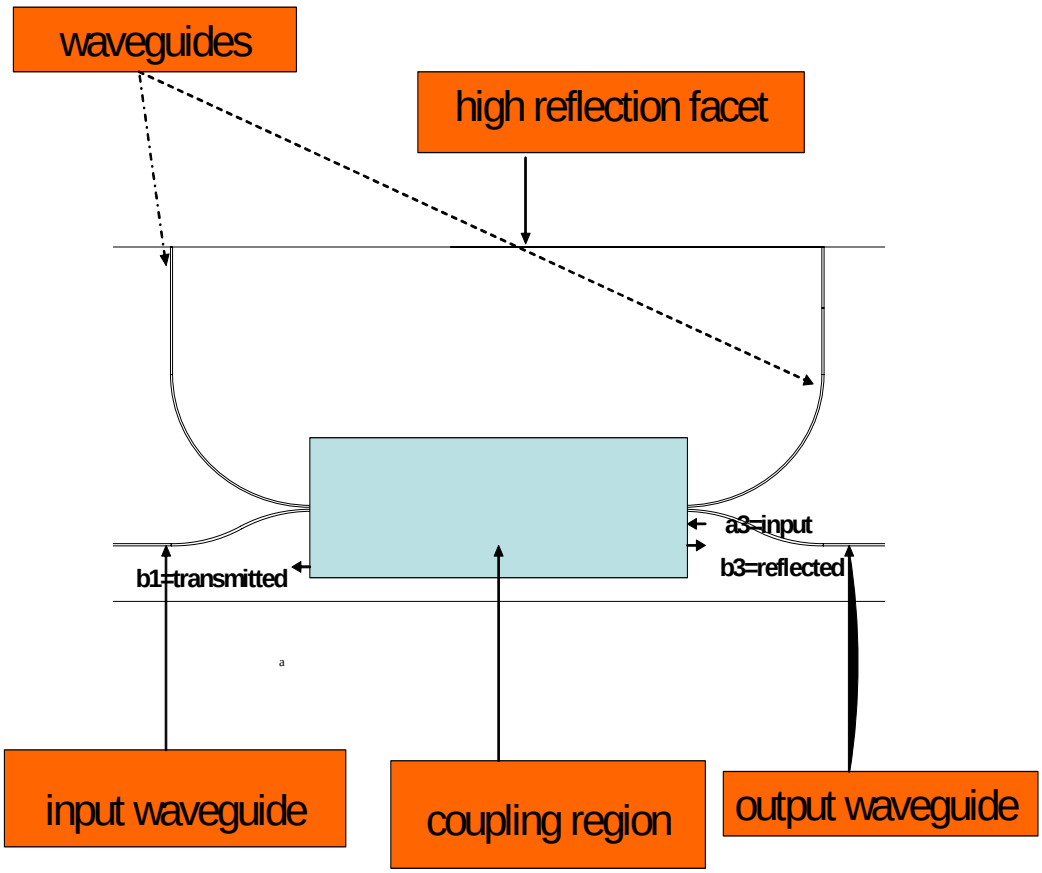

Figure 6.2: Representation of an SRFP resonator where a_3 is the input field, b_1 is the transmitted field and b_3 is the reflected field.

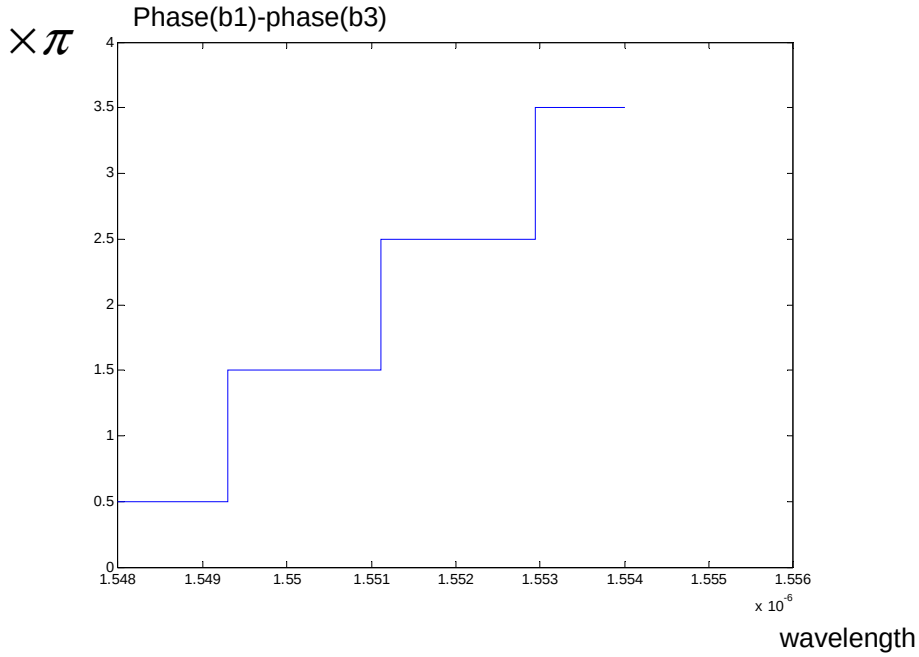

Figure 6.3: Representation of the difference of phase between the reflected field and the transmitted one when the resonator is symmetrical and lossless, which means that r_{hr}=1.

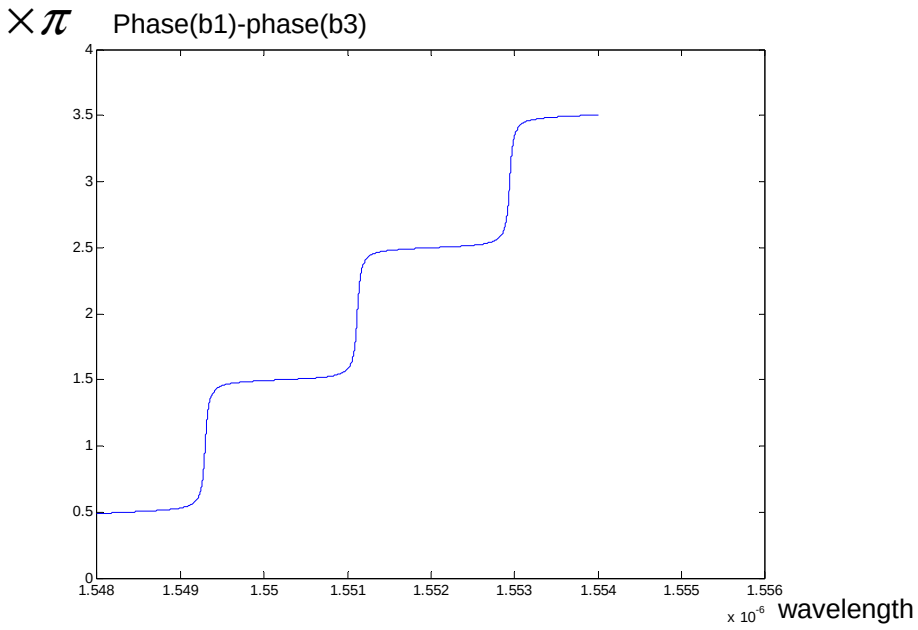

Figure 6.4: Representation of the difference of phase between the reflected and the transmitted fields in the case that the SRFP resonator is symmetrical but not lossless since the reflection of the HR is 90%.

Chapter 7

Characterization of the Waveguide

In order to make a consistent design of our structure we should be able to evaluate accurately the electromagnetic field profile and characteristic within the waveguide. For this purpose, we assume the translational invariance of the material properties such as refractive index, material loss/gain, etc; along the axis of the waveguide. These properties of the material determine the optical mode profile, the propagation constants associated with each mode, polarizations, and cutoff conditions.

7.1 Slab waveguide

In the one-dimensional slab case shown in fig. 7.1, we can obtain an exact solution by solving the Helmholtz equation (7.1):

$$\nabla^2 U(x,y) + \left[\widetilde{n}^2 k_0^2 - \widetilde{\beta}^2\right] U(x,y) = 0, \tag{7.1}$$

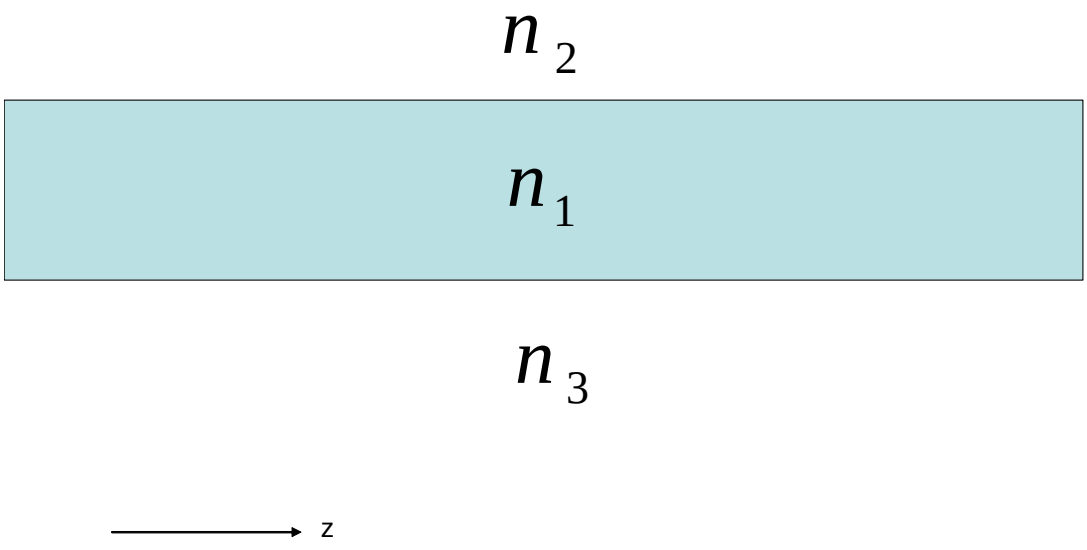

Figure 7.1: Schematic of a three-layer slab waveguide. Indices are assumed to be uniform in the z-direction.

where $U(x, y)$ is the complex amplitude of the electric field, k_0 is the propagation constant in the free space, $\widetilde{n}$ is the effective index of refraction, and $\widetilde{\beta}$ is the propagation constant. An exact solution can be obtained by solving equation (7.1) for uniformity in each of the three regions and then matching the boundary conditions at the interferences [40].

7.2 Effective index technique for two-dimensional waveguides

In practice, waveguiding happens in two-dimensional schemes both in the lateral y-direction and in the transverse x-direction. These schemes are called either two-dimensional or channel waveguide. Then we should solve,

$$\nabla^2 E(x,y) + \left[\widetilde{n(x,y)}^2 k_0^2 - \widetilde{\beta}^2\right] E(x,y) = 0, \tag{7.2}$$

where $\widetilde{n(x,y)}$ is now a function of both x and y. However, it is impossible to find an exact analytical solution when matching the lateral boundary conditions for all values of x. With some consistent assumptions one can still find an analytical expression that is close to the real physics.

7.2.1 Large index discontinuity assumption

Under the assumption of very strong refractive index discontinuities at the active-cladding interfaces, the boundary conditions can be set around the perimeter since the field within the active region will fall to zero at the boundaries. Then we can express the field within the active region as the superposition of the field in the two-dimensional transverse and lateral slab waveguides.

$$E(x,y) = E_0 \cos(\frac{\pi m_x x}{d}) \cos(\frac{\pi m_y y}{w}), (\Delta n \longrightarrow \infty)$$

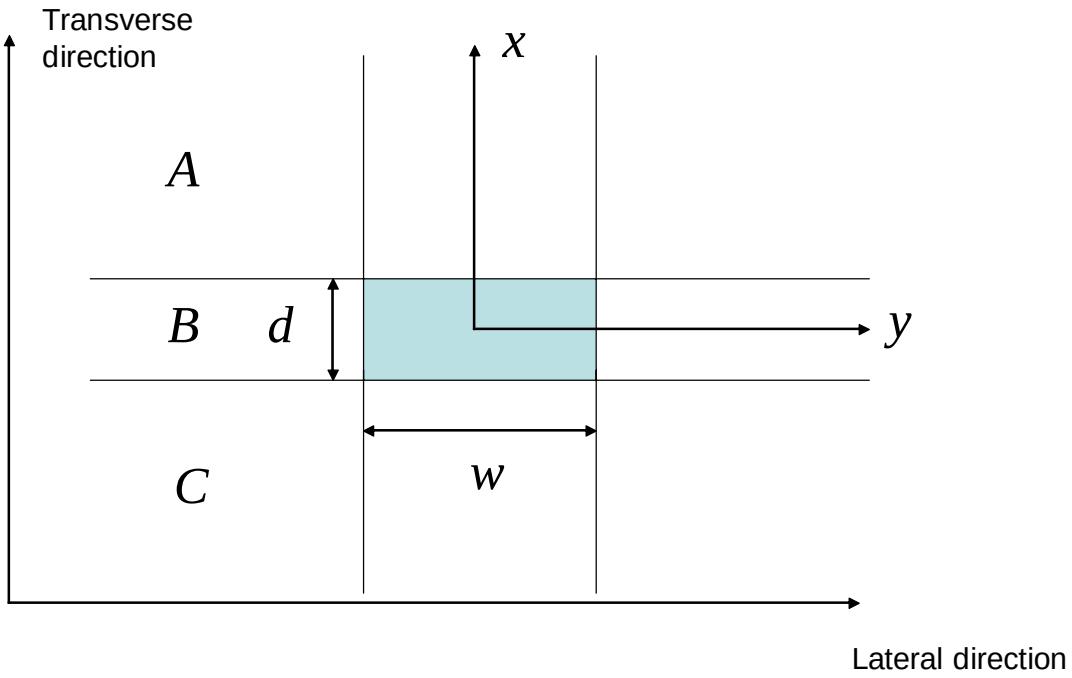

Figure 7.2: View of the cross section of the waveguide. The different transverse regions are denoted A, B, C, and the lateral ones 1, 2, 3 [40].

Since the assumption of large index discontinuities cannot be made all the time, we should solve the problem numerically. One of these numerical techniques is called the effective index technique.

7.2.2 Effective index technique

The effective index technique is based upon a sequential solution of the field of the structure shown in fig. 7.2. In order to express the overall channel waveguide mode shape in each of the three lateral regions, this technique uses the simple (uniform y) slab mode solution along x. Then this solution is used to solve the simple (uniform x) slab mode solution along y. When the contrast of index of refraction between the

core and the cladding is high and $\frac{w}{d} >> 1$, this technique is the most accurate.

The solution sequence for the effective index is as follows:

1. We first distinguish between the longer dimension (y in our example) and the shorter (x-dimension) one. We assume that the region is uniform in the longer dimension (y). We then solve the three layer slab problem across the shorter dimension using n_a,n_b, n_c and obtain three effective indices ($\overline{n_1}, \overline{n_2}, \overline{n_3}$).

2. We solve the three layer slab problem across the longer dimension using ($\overline{n_1}, \overline{n_2}, \overline{n_3}$), assuming that the regions are uniform across the shorter dimension (x). The result is a final effective index for the two-dimensional problem. This is used for the lateral k_y and γ . The net axial propagation constant, β always satisfies

$$\beta^2 = [k_0 n_b]^2 - (k_x^2 + k_y^2)$$

This figure is strictly for TE modes and many problems can not be solved accurately by using the effective index method.

7.3 Numerical finite-difference eigenmode solver

Many problems cannot be accurately solved by the effective index method. A straightforward alternative solution to equation (7.2) uses the finite-difference technique. The first step in this finite-difference procedure is the selectivity of a computational window with the following restrictions:

1. Need to limit the size of the domain for computational efficiency.

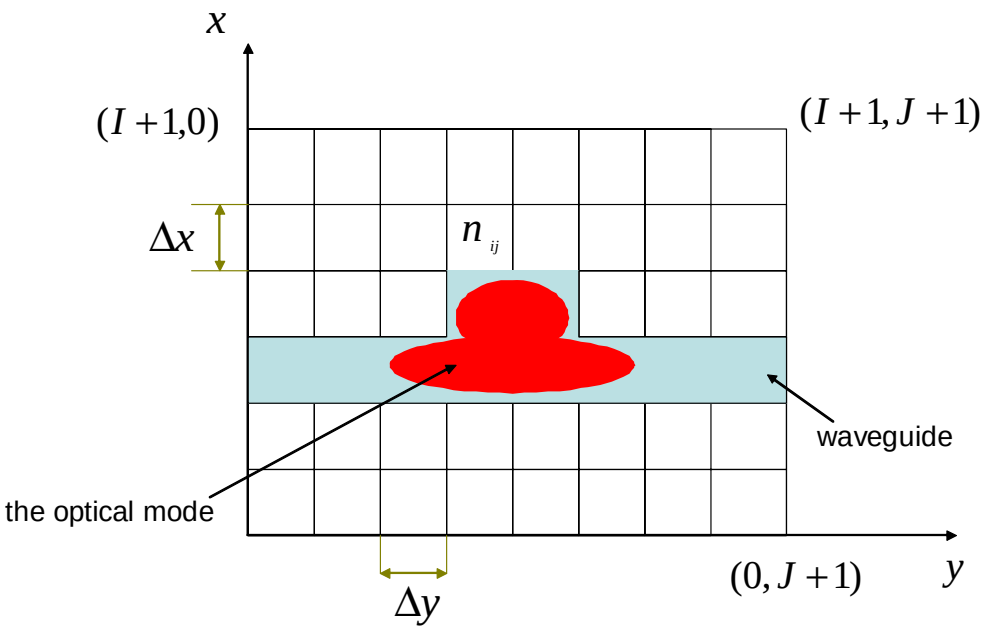

Figure 7.3: Illustration of a finite difference grid over a buried-rib waveguide.

2. The domain should be large enough to contain the field distribution that we want to calculate.

The second step is to discretize the computational window using a grid as indicated in fig. 7.3, given by

$$x = i\Delta x, x = 0, \ldots I + 1,$$
$$y = j\Delta y, y = 0, \ldots J + 1.$$

This grid discretization can be either uniform or nonuniform. The lateral normalized field $E(x, y)$ will be found at the nodes of the grid by converting equation (7.2) into a set of finite difference equations specified at the grid points. So we have to solve the following equation:

$$\frac{\partial^2 E(x,y)}{\partial x^2} + \frac{\partial^2 E(x,y)}{\partial y^2} + k_0^2 \left[\widetilde{n(x,y)}^{\,2} - \overline{n}^2 \right] E(x,y) = 0, \tag{7.3}$$

where $\widetilde{n(x,y)}$ is the lateral index profile and $\overline{n}$ the modal effective index. We need to approximate the partial derivatives using the finite-differences. This is accomplished by using a second-order Taylor series expansion of the fields in adjacent grid points, given by

$$\begin{aligned} E(x+\triangle x, y) &= E(x,y) + \triangle x \frac{\partial E(x,y)}{\partial x} + \frac{(\triangle x)^2}{2} \frac{\partial^2 E(x,y)}{\partial x^2} + ... \\ E(x-\triangle x, y) &= E(x,y) - \triangle x \frac{\partial E(x,y)}{\partial x} + \frac{(\triangle x)^2}{2} \frac{\partial^2 E(x,y)}{\partial x^2} + ... \end{aligned}$$

By adding the two previous equations, and neglecting the terms with greater than two, we will obtain

$$\frac{\partial^2 E(x,y)}{\partial x^2} \approx \frac{E(x+\triangle x, y) - 2E(x,y) + E(x-\triangle x, y)}{(\triangle x)^2}. \tag{7.4}$$

We neglect the high-order terms since we assume that the grid spacings are sufficiently small. The corresponding expression for the partial derivative with respect to y is

$$\frac{\partial^2 E(x,y)}{\partial y^2} \approx \frac{E(x, y+\triangle y) - 2E(x,y) + E(x, y-\triangle y)}{(\triangle y)^2}. \tag{7.5}$$

Using equations (7.4) and (7.5), equation (7.3) can be written in discretized form as

$$\frac{E(x+\triangle x,y)-2E(x,y)+E(x-\triangle x,y)}{(\triangle x)^2}+$$

$$\frac{E(x,y+\triangle y)-2E(x,y)+E(x,y-\triangle y)}{(\triangle y)^2}+$$

$$k_0^2\left[\widetilde{n(x,y)}^2-\overline{n}^2\right]E(x,y)=0.$$

This equation will be rewritten in the form

$$\frac{E_j^{i+1}-2E_j^i+E_j^{i-1}}{(\triangle x)^2}+\frac{E_{j+1}^i-2E_j^i+E_{j-1}^i}{(\triangle y)^2}+k_0^2\left[\widetilde{n(x,y)}^2-\overline{n}^2\right]E_j^i=0,$$

where by denoting

$$\begin{aligned}
E_j^i &= E(x,y),\\
E_j^{i+1} &= E(x+\triangle x,y),\\
E_j^{i-1} &= E(x-\triangle x,y),\\
E_{j+1}^i &= E(x,y+\triangle y),\\
E_{j-1}^i &= E(x,y-\triangle y).
\end{aligned} \tag{7.6}$$

The scalar wave equation equation (7.3) can be discretized to provide the matrix form,

$$\frac{E_j^{i-1}}{k_0^2\Delta x^2}+\frac{E_{j-1}^i}{k_0^2\Delta y^2}-(\frac{2}{k_0^2\Delta x^2}+\frac{2}{k_0^2\Delta y^2}-(n_j^i)^2)E_j^i+\frac{E_{j+1}^i}{k_0^2\Delta y^2}+\frac{E_j^{i+1}}{k_0^2\Delta x^2}=\overline{n}^2E_j^i. \tag{7.7}$$

To complete the problem we need to specify the boundary conditions. Different choices exist [69] but the simplest choice is to set the fields to zero around the border of the computational window. As long as the field is essentially confined within the computational window, it is a fair approximation to consider the field to be null around the window border. The set of algebric finite-difference equation (7.7) can be cast in the form of a matrix eigenvalue problem,

$$A.E = \overline{n}^2 E,$$

where A is a matrix of dimension $I.J \times I.J$ where I, J are the integer numbers of grid points along the x and y axes, E is a length $I.J$ column eigenvector containing the field $E(x, y) = E_j^i$ at all the points on the 2 D grid. The details of these calculations are represented in [69]. $\overline{n}^2$ is the eigenvalue associated with the eigenvector E and represents the effective index of refraction.

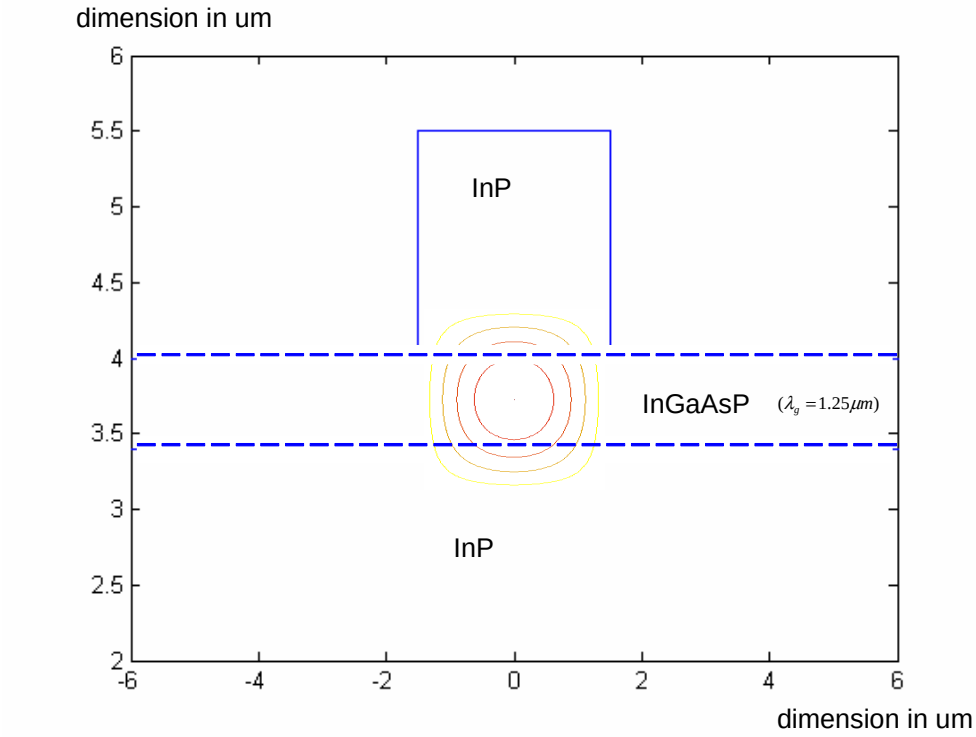

Figure 7.4: Beam profile of the fundamental TE mode obtained by using the numerical finite differential method that we implemented. The lines in blue illustrate the outline of the different material layers composing the ridge waveguide. The structure of the ridge waveguide is the one shown in fig. 1.5. The effective index for the mode shown is $n_{eff} = 3.36$. Depending on the width and the length of the ridge, we can either get a single or multi-mode waveguide.

Chapter 8

Fabrication

In this chapter we will discuss the fabrication of the device. The choice of the material, design of the wafer, and choice of gas for the etching will be described in the following sections.

8.1 Choice of the material

There is an increasing demand for integrating different modules such as source, modulator, and other components on the same chip. For optical communication, these devices need to operate at the wavelengths around 1.55 μm at which the propagation loss of silica is a minimum [41]. The SRFP resonator introduced earlier can be realized in a number of different dielectric materials. In the present work, we focus upon the $In_{1-x}Ga_xAs_yP_{1-y}$. III-V semiconductor alloy, because it allows for the manipulation of the relative fractions x and y of the elements during the semiconductor growth process, leading to the tuning of the energy bandgap. For material lattice, matched to InP, bandgap wavelengths in the range of 1.0-1.65 μm are available [70]. The lattice parameters are similar to those of ternary InGaAs and quaternary In-

GaAsP alloys. Thus, InP is a good substrate for optical integrated circuits operating around 1.55 μm. Besides, it is possible to implement electronic devices as well optical devices on the same chip due to the high thermal conductivity of the material. We should also keep in mind that the III-V materials have a direct bandgap, allowing them to be integrated as a gain medium in different embodiments. Depending upon the growth conditions of the crystal, the emission intensity of such materials can change [60]. For these reasons we have decided to demonstrate the device in an InP based material. However, one could decide to fabricate the device in other materials. Besides, the range of applications of the device is not restrained to those related to a WDM application.

8.2 Choice of the gas for etching

The InP and InGaAsP etching is essential for fabricating our device. Structure definition in our material must be carried out by dry etching when profile anisotropy is required (independent of crystal orientation), particularly for high aspect ratios. Various plasma etch tools and dry etch approaches have been reported in the literature [47][46][44][61][51][55][53]. We analyzed those methods and concluded which ones met the majority of our device dry etching needs, [44]. The etching had to meet several requirements, most important being [45]:

- High selectivity.
- Good control of the etch depth and etch profile. For an exact definition of the geometry of the microstructures, it is necessary that etch depth and etch profile be well-controlled, [46].
- The material must be etched with sufficient selectivity compared to the masking material.

8.2.1 Several etches

Plasma etching of group III-V semiconductors (GaAs, GaAsP, InP) is of current interest because of the importance of these compounds in photonic communication, and high speed and discrete electronic technology. Generally, these compounds had been etched until the early 1980s in chlorine or its mixtures [47][48][49],[50]. In the early 1980 many papers praised the advantages of plasma systems using gases based on different chlorine derivative. Klinger and Greene [51] discussed the etching of GaAs material (which may be similar to the one of InP) in $CCl_{4-x}F_x (x = 0, 2, 4)$ and mixed $CCl_{4-x}F_x$/Ar discharges. They concluded that the rate limiting step of the reactive ion etching in the halocarbon discharges (especially those containing F) was not the removal of absorbed C but rather the removal of Ga. Moreover, they found that the ion-induced chemical played an important role and if one minimized ion bombardment effects (such as in high pressure barrel reactors) the etch rate in CF_4 discharges is reduced to less than a measurable value. They observed the accumulation of carbon on the target surface during the RIE in $CCl_{4-x}F_x$ discharges. They believed that the carbon deposition occurred due to the impact dissociation of halocarbon ions ($CCL_x^+$and/or CF_x^+ , depending on the etch gas) and the dissociation chemisorptions of halocarbon radicals (CCl_x and/or CF_x).

8.2.2 The carbon tetrachloride etch

Burton and Smolinsky [52] examined the use of CCl_4 as an etching agent for a III-V material. A correlation between Cl atom emission intensity with the etching rates of GaP and GaAs (but not InP) was proven. This result led to the conclusion that CCl_4 is the primary etchant for GaAs and GaP, but that other CCl_x species must also play an active role in the etching of InP. That is why the authors of [47] focused their effort on understanding CCl_4 plasma etching of InP. They observed carbon

deposition and showed that this deposition is largely responsible for controlling the etching rates. They concluded that the rate limiting step in CCl_4 plasma etching of InP and GaAs is the diffusion of reactants and products through a plasma deposited chlorocarbon layer. In order to avoid this problem, chlorine derivative gases with carbon have been proposed, such as Cl_2 [53]. However, phosphorus depletion from (110) surfaces of InP by exposure to Cl_2 gas has been suggested [54]. Reactive ion etching of III-V materials using $SiCl_4$ as the etching gas has been demonstrated [55]. One advantage of $SiCl_4$ over chlorinated halocarbons is that it will not produce chlorinated polymer films, which can contaminate the sample, the etching chamber and the pump fluids. On the other hand a layer of oxidized Si or chloride could be deposited on the substrate. This necessitates an additional step, which may consist of either immersing the substrate in an HF solution or bombarding it with Ar. The ultimate problem is the contamination and redeposition of nonvolatile compounds. RIE using gases that do not contain halogen have been analyzed too. One example is the use of Cl_2, which exhibits phosphorus depletion and indium residues on the surface, [54]. However, that exhibits phosphorus depletion and indium residues on the surface. A derivate compound of F-discharge has also been used, but in some cases it stops etching due to the formation of an involatile group III fluoride, which makes the surface inert. So we can say that until the mid 1980s the most serious etchants of III-V material had been halogen derivatives. They exhibited notable drawbacks:

- Formation of residue on the surface of the wafer that slows or literally stops the etching, and which can also contaminate the chamber.
- Generally rough surface morphology is observed, [56] [57].

The creation of a rough surface generates additional loss for the guided light due to scattering, leading to a decrease in intensity proportionally to the roughness of

the waveguide.

- Some of these gases are toxic and corrosive.

8.2.3 The use of CH_4/H_2 etching

In the late 1980s and the early 1990s, papers had been published suggesting the use of CH_4/H_2 mixtures [58]. CH_4/H_2 plasma has been shown to provide certain advantages over some of the halogenated etchants. The feedstock gases are of low toxicity and are not corrosive (as opposed to Cl_2 and BCl_3), although they are flammable. There is no known threat to the ozone layer, as there is with the chlorofluorocarbons. The polymer that deposits on mask surfaces gives high etch selectivity between InP and the mask, whereas chlorinated gases can etch the photoresist, SiO_2 and SiN_x, at significant rates. The polymer film that deposits on the chamber walls is less hygroscopic than chlorinated surfaces. Besides, the etching walls are smoother compared to the walls generated by gas mixtures containing chlorine. Surface analysis shows that under etching conditions that maximize the InP, there is a hydrocarbon coverage on the InP surface, and the surface is significantly depleted of P. The etch rate is limited by the flux to the surface of hydrocarbon reactants responsible for In desorption. Polymer deposition generates particulates and contaminates the chamber, which necessitates periodic chamber vacuuming O_2 plasma cleaning. In addition, like most plasma processes, reproducible etching rates are achieved only after seasoning the reactor by depositing polymer on the chamber walls. One of the minor disadvantages of this chemistry is the production of phosphine as an etching product. The quantities produced are 100-1000 times less than those during a typical InP metal-organic chemical vapor deposition growth run; standard MOCVD scrubbing practices can be used to safely detoxify the effluent [58]. But even though the CH_4/H_2 mixture overcomes the general rough surface obtained with a Cl_2-based

mixture, the major limitation with its use is the slow etch rates, which are typically ≤ 500 $A^0 \times min^{-1}$ for dc biases of < 350 V and pressure ≤ 60 mTorr [60].

8.2.4 Introduction of HI/H_2

Gaseous discharges of HI/H_2 mixtures [61] etche in an anisotropic manner at much faster rates while still retaining a smooth, residue-free surface. The mixture displays very high selectivity for etching over common masking materials such as photoresist, and the etch rates are approximately a factor of 8-10 faster than those obtained with a mixture under the same conditions [62]. Due to the absence of any carbon residue, there is no heavy polymer deposit on the mask within the chamber, which is characteristic of plasma [63].

8.2.5 Fabrication

The SRFP resonator fabrication process, illustrated in fig. 8.1, proceeded as follows (described in depth in [64]):

1. A 120 μm Si etch mask layer was deposited by plasma-enhanced chemical vapor deposition.

2. 550 μm of polymethylmethacrylate (PMMA) electron-beam resist was applied by spin-coating and then baked. Several SRFP geometries were patterned into the PMMA layer using an electron beam writer. The electron beam writer was operating at accelerating voltage of 100 KV and 10 nA beam current. Patterns were written with exposure doses of 625, 650, 675, 700 $\mu c/cm^2$.

3. The development of the patterned PMMA film was carried out in a solution of 1:3 MIBK: IPA for 60 s.

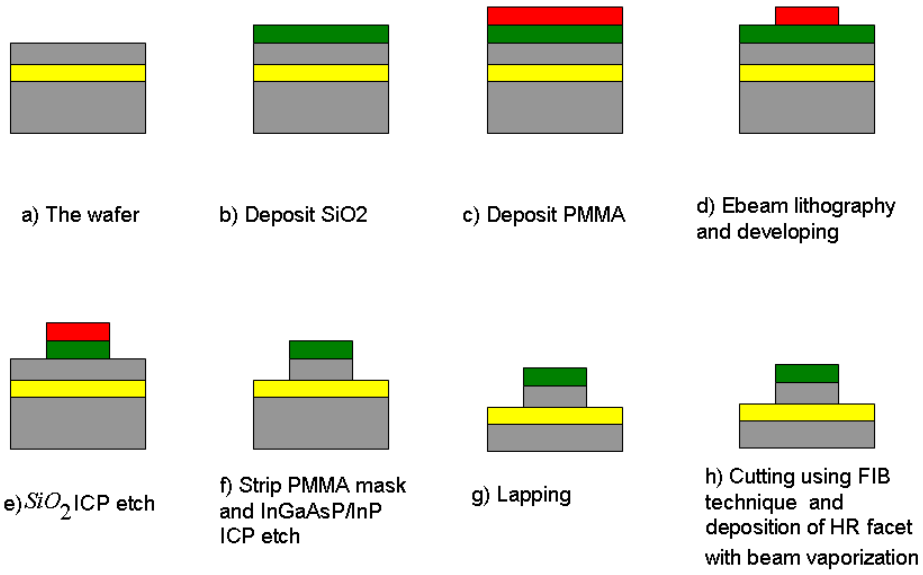

Figure 8.1: Illustration of the different steps of fabrication.

4. The PMMA patterns were transferred into the etch mask layer. The S_iO_2 was etched by inductively coupled plasma reactive ion etching (ICP-RIE) using C_4F_8 plasma.

5. The remaining PMMA was removed with a gentile plasma etching step.

6. The patterned layer then served as a hard mask for transfer into the active membrane, using a low voltage ICP-RIE etch as we had analyzed it previously. In the etch recipe used, the gas flow was 10/6 sccm, the chamber pressure was 5mTorr , and the ICP and rf electrodes were driven with 950 W and 30 W. The plasma dc self-bias was 100 V, and the etch rate was 325 nm/min.

7. In our specific application we do not need to remove the SiO_2 since it can be used as a protection layer and does not change the optical beam. If we would like to get rid of it, we can use a buffered hydrofluoric (HF) acid solution.

8. The wafer was lapped using Al_2O_3 powder. The thickness of the wafer was brought to 100 μm in order to allow a better cleaving.

9. Cutting the facet using focus ion beam (FIB) technique.

10. HR coating deposition.

Chapter 9

Choice of the Coupling Region

We have to choose the nature of the coupling region that couples light from the main waveguide to the SRFP resonator. As we discussed, we have chosen to fabricate the device on an InP semiconductor-based material. In this case the index of refraction of the material is relatively high (around 3.4) and therefore the light is relatively confined within the waveguide core. There are several candidates for the coupling region.

9.1 Adiabatic coupler

In general, an adiabatic process is a slowly varying process where the variation is slow enough that there is no transition between energy levels. Therefore, as the system is changed from one stage to another, there is no change in level populations. In the special case of Integrated Optical Circuits (IOC), the variation is the physical variation of the waveguide structure. This means that if a mode is initially excited all the power stays in the same mode as the waveguide structure changes. For that to

happen the mode shape has to change as the waveguide structure changes [66]. Fig. 9.1 illustrates different cases of adiabatic couplers. In other schemes of coupling, the quality of the coupler heavily depends upon the exact dimensions of the length and the width of the coupling region. In contrast, an adiabatic coupler is very tolerant to these parameters. However, an adiabatic coupler is not usually an appropriate choice for a photonic integrated circuit especially for material where the intrinsic loss is high, such as in III-V materials. The reason is that in order to have a slow varying change of the optical mode shape a longer coupling length is required compared to other couplers for similar performance. Thus an adiabatic coupler is not necessarily an appropriate choice for a photonic integrated circuit (PIC). But it seems to be appropriate for devices where the dimensions are bigger than a few mm.

9.2 Evanescent coupler

Another commonly used type of coupler is the evanescent coupler. There are mainly two types of evanescent couplers, the in plane lateral evanescent directional coupler [67] and the vertical evanescent coupler [68]. The two waveguides are not physically connected to each other. Each initially separate guide acts as a dielectric perturbation for the others. The perturbation causes the coupling between the mode of one waveguide to the mode of the other [67]. This scheme of coupling is essentially used in cases of low index contrast waveguides where the optical mode is not strongly confined within the core but where their tails can perturb the mode of the adjacent waveguide and the opposite one. However, in the case of high index contrast waveguides the tight confinement of the optical mode within the waveguide requires the coupling gap be made extremely small around 100 nm for a coupling length of the order of 100μm. Fabrication of features of the order of 100 nm requires ebeam lithography and very accurate etch techniques. Due to the very small gap between the two waveguides

the fabrication tolerance of the device is very important meaning a small change of the order of magnitude of 0.1 μm would drastically change the performance of the device. The vertical evanescent coupling configuration has the advantages that the gap between the two waveguides and can be precisely controlled via epitaxial crystal growth [71], physical vapor deposition [72], and spin-coating of dielectric materials [73]. The disadvantage of this technique is the very complex and difficult chain of fabrication requiring several steps of fabrications, in contrast with a simple planar fabrication requiring only one step of lithography.

9.3 TMI coupler

Two-mode interference (TMI) couplers consist of two single-mode input waveguides figs. 9.2, [74]-[80]. The structure can be considered to be a directional coupler in which the gap between the guides in the coupling region has been reduced to zero. As for an ordinary directional coupler, the eigenmodes of the "coupling section" consist of one symmetric and one antisymmetric mode. The energy that was originally concentrated in the "top" half of the guide is found in the "bottom" half at distance given by

$$L_\pi = \frac{m\pi}{(\beta_s - \beta_{as})} = \frac{m\pi}{\Delta\beta},$$

where m is a positive odd integer, and β_s is the propagation constant of the symmetric mode and that of the antisymmetric mode. It is then clear that the energy at the output of the two-mode section can be switched from the top half to the bottom half of the guide if we are able to change $\Delta\beta$ [80]. Fig. 9.3 illustrates the distribution of energy along the axis. However, requirements of high power coupling efficiency and proper mode excitation from the single-mode waveguide input to the TMI section

limit the branching angle of the access waveguides to very small values typically < 2 deg. Due to the finite resolution of the lithographic process, part of the area between the access waveguides (shaded region in fig. 9.2 will be filled in a non-reproducible way. This introduces considerable uncertainty in the actual length of the TMI section, causing spread in coupler performance. Moreover, due to the proximity of the input waveguides, extra modal coupling occurs. An alternative to all these solutions is the multi-mode interference coupler, which is easier to fabrication (especially compared to the vertical evanescent coupler), has high bandwidth (devices having a bandwidth of 100 μm operating in the infrared have been demonstrated [81]), and is highly compact. But the major advantage of the MMI coupler compared to other couplers is that it is appropriate for coupling high index contrast waveguides.

9.4 The multi-modes interference (MMI) coupler

The MMI coupler is composed of single-mode input waveguides, a multi-mode waveguide and single-mode output waveguides, fig. 9.4. The MMI coupler concept is based upon the self imaging property of a multi-mode waveguide, where the electromagnetic field profile at the waveguide input is produced at periodic intervals along the waveguide propagation direction [83]. For a strongly guided, step-index multi-mode waveguide, it can be assumed that the penetration depth of each transverse mode into the cladding is equal and negligible. Thus, within the paraxial approximation, the distribution of propagation β_ν is quadratic,

$$\beta_\nu \sim \sqrt{n_r^2 k_0^2 - \frac{\pi^2 (\nu+1)^2}{W_{MMI}^2}} \sim k_0 n_r - \frac{\pi^2 (\nu+1)^2}{2 k_0 n_r W_{MMI}^2}$$

with,

$$k_z = \beta_\nu, k_z \sim \frac{\pi\left(\nu+1\right)}{W_{MMI}}, \tag{9.1}$$

where n_r is the effective refractive index under the ridge, which can be obtained using the effective index approximation [85] [86]. This allows us to reduce the problem to a two-dimensional problem. Fig. 9.5 illustrates the index profile and the field profile across the cross section the MMI coupler. W_{MMI} is the physical width of the MMI coupler, k_0 is the wave number in free space. We also made the approximation that

$$k_0 << n_r k_y. \tag{9.2}$$

Since we have a high contrast index profile, we can assume that the transverse field at the input of the multi-mode section is completely contained within the width of the MMI. Let assume that the multi-mode has M modes. Then the total lateral field profile $h_x\left(y, z=0\right)$ at the input of the MMI section can be decomposed as a linear combination of the fields $h_{x,\nu}\left(y\right)$ of the guided modes so,

$$h_x\left(y, z=0\right) = \sum_{\nu=0}^{m-1} c_\nu h_{x,\nu}\left(y\right), \tag{9.3}$$

where c_ν is the relative contribution of each mode and is given by

$$c_\nu^2 = \frac{\int \left|h_x\left(y, z=0\right) h_{x,\nu}\left(y\right)\right| dy}{\sqrt{\int \left|h_x\left(y, z=0\right)\right|^2 dy \int \left|h_{x,\nu}\left(y\right)\right|^2 dy}}.$$

We have neglected in equation (9.3) the x dependence of the field because the planar guide supports only one mode in this direction. Therefore the total lateral

field profile $h_x(y, z = 0)$ at any distance z along the axis of the MMI section can be decomposed as a linear combination of the fields $h_{x,\nu}(y)$ of the guided modes with their respective phase factors,

$$h_x(y, z) = \sum_{\nu=0}^{m-1} c_\nu h_{x,\nu}(y) e^{-j\beta_\nu z},$$

where β_ν is the propagation constant of the mode υ and is given by equation (9.1). Under the condition of high contrast that results in strongly confined field we can use the paraxial approximation and therefore $h_{x,\nu}(y)$ can be written as $\cos(\frac{m\pi}{W_{MMI}}y)$. So $h_x(y, z)$ can be written as

$$h_x(y, z) = \sum_{\nu=0}^{m-1} c_\nu \cos(\frac{m\pi}{W_{MMI}}y) e^{-j\beta_\nu z}.$$

That shows that a symmetric intensity pattern is repeated periodically at intervals of Λ along the guide, where $\Lambda = \frac{n_r W_{MMI}}{\lambda_0}$. It can also be shown that N images of a symmetric field from the input guide are formed in the plane $z = \frac{\Lambda}{N}$,and the images are equally spaced across the multi-mode guide, with a pitch $\frac{W}{N}$ [87]. Fig. 9.5 illustrates the total field distribution within an MMI section. It is important that the multi-mode section supports a sufficient number of guided modes to make accurate imaging of the input field. This number is decreased by miniaturizing the MMI. In general we can write down the expression of possible $h_x(y, L_{MMI})$:

$$h_x(y, L_{MMI}) = \begin{array}{c} \sum_{\nu=0}^{m-1} c_\nu h_{x,\nu}(y) \\ \sum_{\nu=0}^{m-1} (-1)^{\nu+1} c_\nu h_{x,\nu}(y) \\ \sum_{\nu=even} j(-1)^q c_\nu h_{x,\nu}(y) + \frac{j(-1)^q+1}{2} h_x(y,0) \end{array}$$

$$for\ L_{MMI} = \begin{array}{c} (2q)3L_\pi \\ (2q+1)3L_\pi \\ (q+\frac{1}{2})3L_\pi \end{array}$$

As the self-imaging depends on the interference of different modes the coupling length L_c between the first two lowest order modes of the MMI coupler is used as a characteristic dimension,

$$L_c = \frac{\pi}{\beta_0 - \beta_1} = \frac{4}{3} n_r \frac{W_{eq}^2}{\lambda}, \tag{9.4}$$

where β_0 and β_1 correspond to the propagation constants of the two first modes, and W_{eq} corresponds to the equivalent width of the MMI coupler. In the case of a strongly guided structure, W_{eq} is equal to the physical length of the MMI coupler, W_{eq}˜W_{MMI}. equations (9.4) shows that

- When $L_{MMI} = (2q)3L_\pi$, the field at the entrance is reproduced at the end of the MMI section (self-imaging effect), and the coupler is in the bar state.
- When $L_{MMI} = (2q+1)3L_\pi$, the field at the end of the MMI section is in an x-z plane mirror image of the field at the entrance, and the coupler is in the cross state.
- When $L_{MMI} = (q+\frac{1}{2})3L_\pi$, the field at the end of the MMI section is a linear combination of the original field at the entrance and its x-z plane mirror image with relative phase of $\frac{\pi}{2}$, which means that the coupler operates in the 3 dB

coupler state. It has been shown in [74] that if the modes 2, 5, 8,... in the MMI section are not excited, i.e, if $c_\nu = 0$ for $\nu = 2, 5, 8$,then similar resonances as stated by equation (9.4) occur for MMI section lengths that are multiples of L_π (restricted multi-mode resonance) instead of $3L_\pi$ (this is typically referred to as one of general interference), thus allowing the design of couplers with MMI section three times shorter; this is what is called the restricted multi-mode interference.

9.5 Restricted interference multi-mode resonance

Fig. 9.6 depicts the top view of a 3 dB MMI coupler based upon the restricted interference multi-mode resonance

$$L_{MMI} = \frac{3n_r}{4} W_{MMI}^2. \tag{9.5}$$

In the case where the cross section of the waveguide is the one shown in fig. 1.6 (a) and where the width on the single mode waveguide is $w = 3$ μm, then $W_{MMI} = 18$ μm. Knowing that $n_{eff} = 3.26$, then using equation (9.5) we find that $L_{MMI} = 520$ μm. We fabricated a set of different of MMI whose lengths vary from $L_{MMI} = 500$ μm to $L_{MMI} = 540$ μm by changing the length of the coupler by 5 μm successively each time. Fig. 9.7 represents the SEM picture of an MMI coupler that we fabricated.

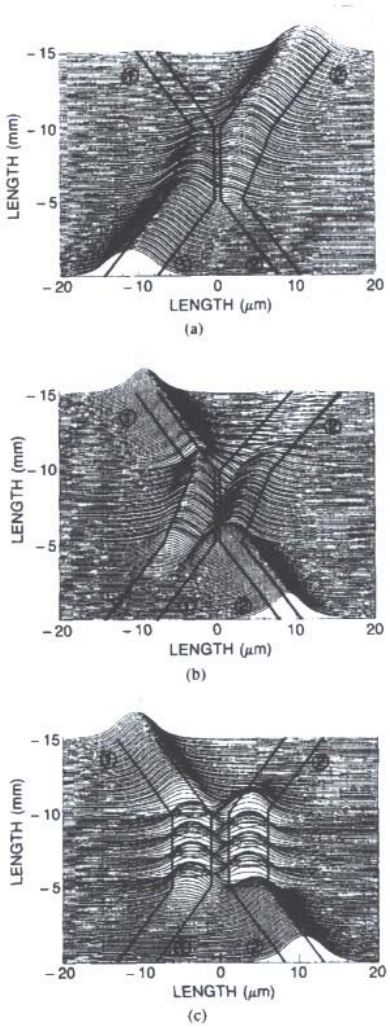

Figure 9.1: (a) and (b), simulations of light (power) propagation along an asymmetric adiabatic coupler directional coupler and (c), along a symmetric directional coupler. The light is coupled through the input guide at the bottom [66].

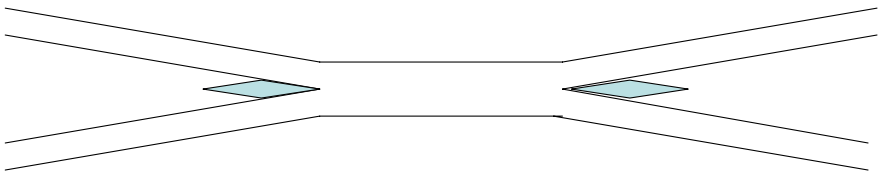

Figure 9.2: Representation of a classical two-mode interference (TMI) coupler.

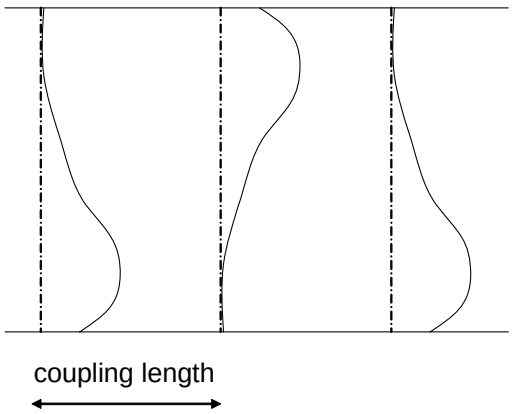

Figure 9.3: Energy distribution along the propagation direction in a two-mode waveguide due to the interference between modes [80].

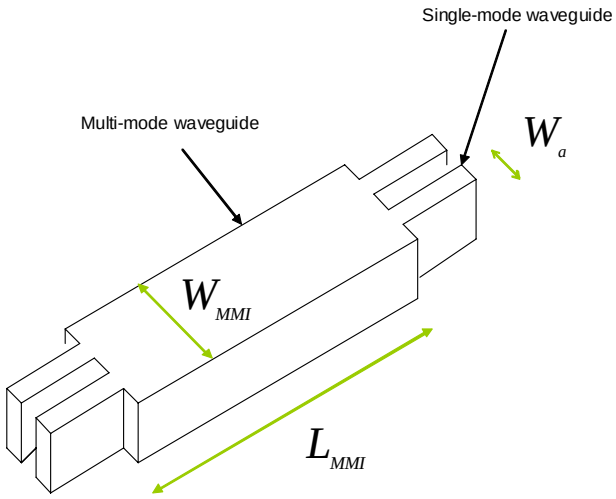

Figure 9.4: Illustration of a 2 X 2 MMI coupler where the input and output waveguides are single-modes and where the center waveguide supports multi-mode. The propagation happens along the z-axis [84].

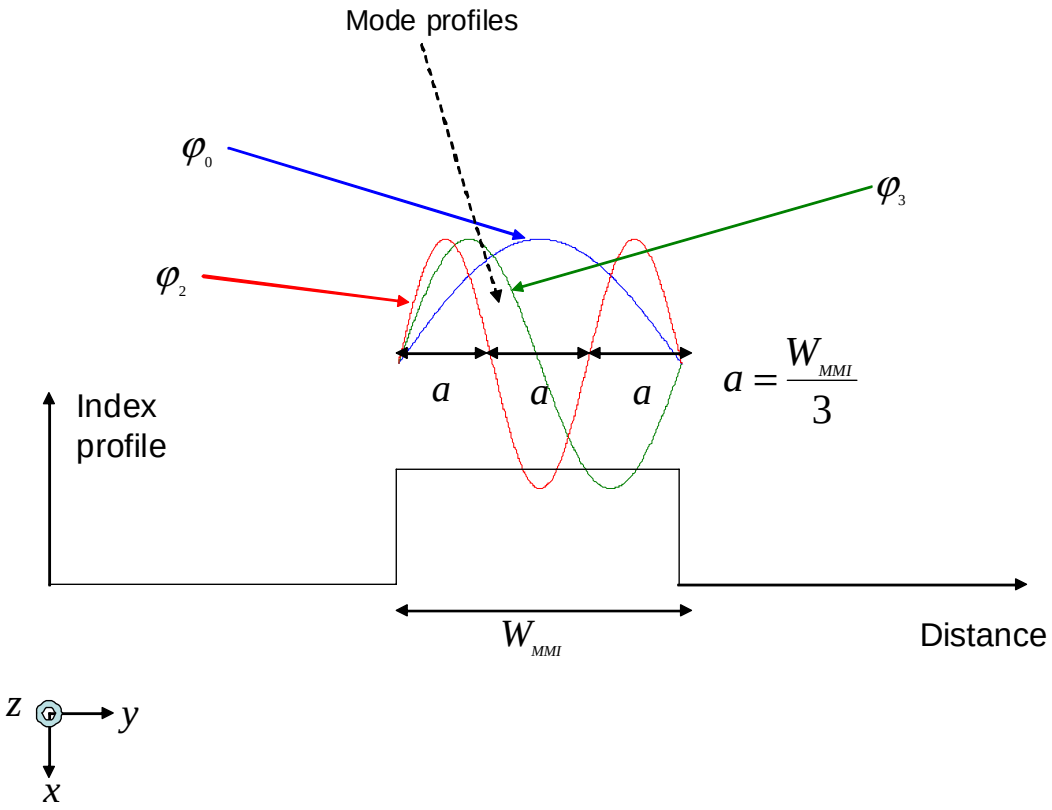

Figure 9.5: The cross section profiles of different modes.

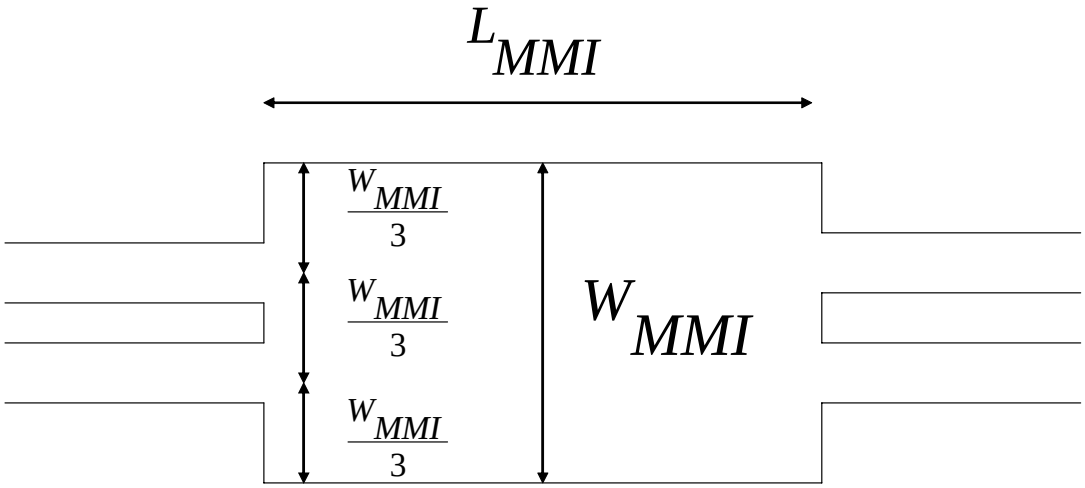

Figure 9.6: Top view of a 3 dB MMI coupler based on the restricted interference theory.

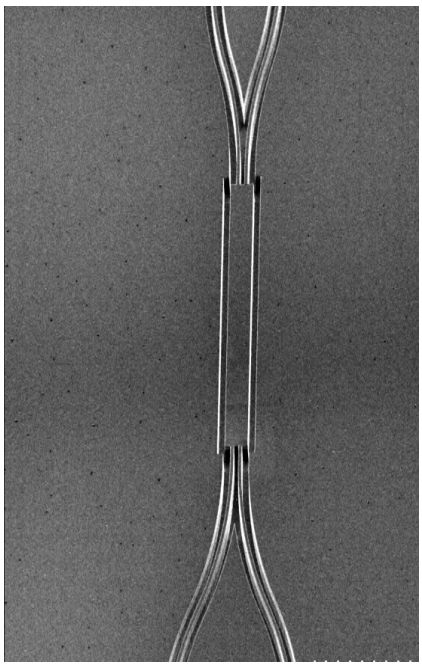

Figure 9.7: SEM picture of a fabricated MMI coupler.

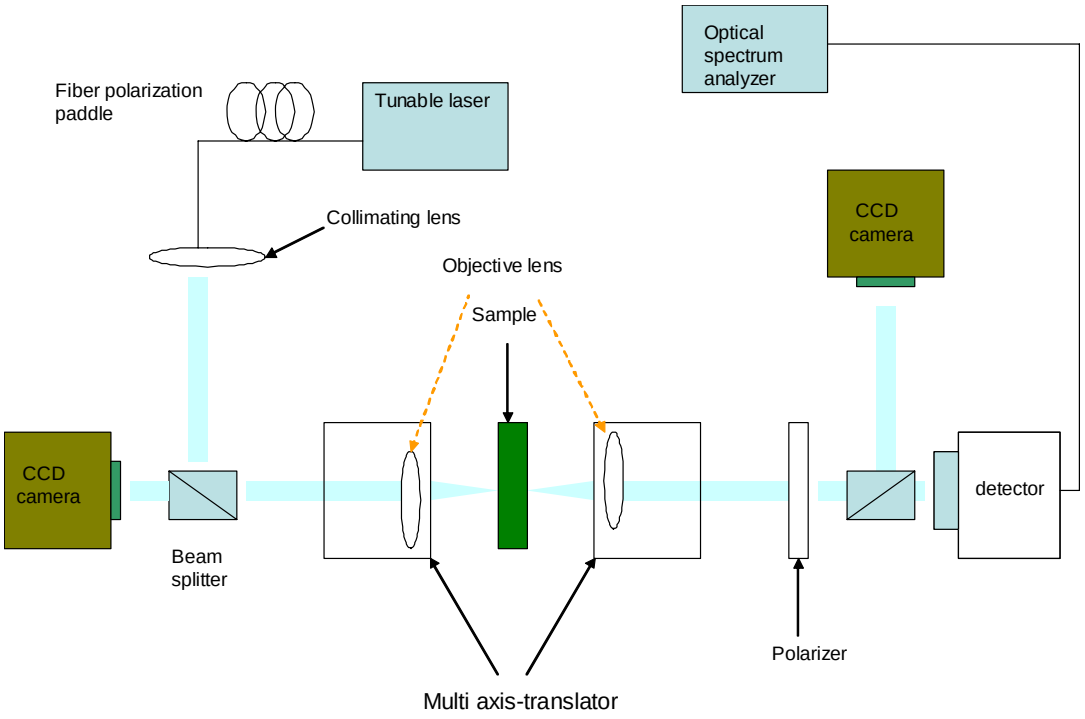

Figure 10.1: Representation of the testing bench.

Chapter 10

Testing

The optical setup shown in fig. 10.1 is used to characterize the SRFP. A tunable laser lasing from 1440 nm to 1640 nm and delivering few milliwatts was used. The laser is used on an automatic mode and sweeps the whole range at a speed of 5 nm/s. The laser is coupled to single-mode fiber. The polarization of the light inside the fiber is controlled with a set of fiber paddles. The light coming out of the fiber is then collimated for free space. A linear polarizer is used to select the correct polarization. The light is then coupled into the waveguide facet of the device through an aspheric lens (50-60)X (NA=0.65). Another aspheric lens is used to collect light from the resonator. For careful positioning of the lenses focal plane relative to the input and output facets, the lenses are mounted on micrometer translation stage. The micrometer have five axes and a resolution of 0.02 μm. For optimizing the input and output coupling conditions, an infrared vidicon camera is useful for viewing the optical mode profile. In order to measure the transmitted light through the device, a photo detector is placed at the output. The entire optical tool used had an anti-reflection (AR) coating for the range of wavelength of operation.

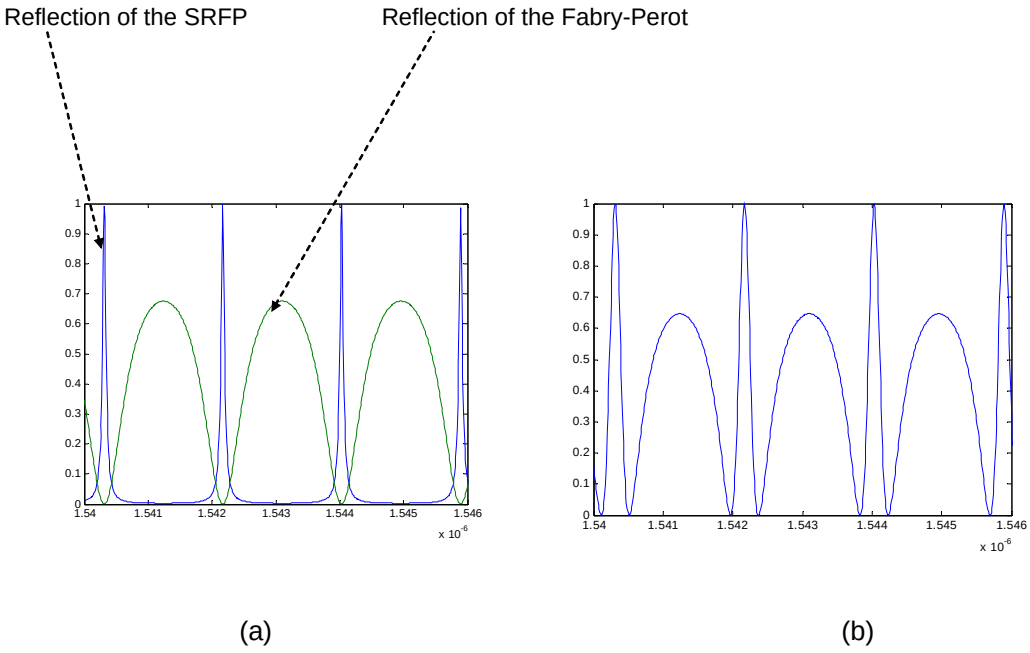

Figure 10.2: (a) Represents the reflection spectrum of the FP and the SRFP separately and (b) represents the reflection spectrum of the structure shown in fig. 5.5.

10.1 Preliminary simulation

With the help of the T matrix formalism, we made different numerical simulations of the structure shown in fig. 5.5 for a broad range of cases. Our goal was to see in which cases we were more able to detect the response of the SRFP and to differentiate its contribution to the responses of the structure shown in fig. 5.5. The simulations showed that the best case is where the length of the Fabry-Perot obtained with the combination of waveguides 1, 3 and facets r_1, r_3 is the same or a multiple of the

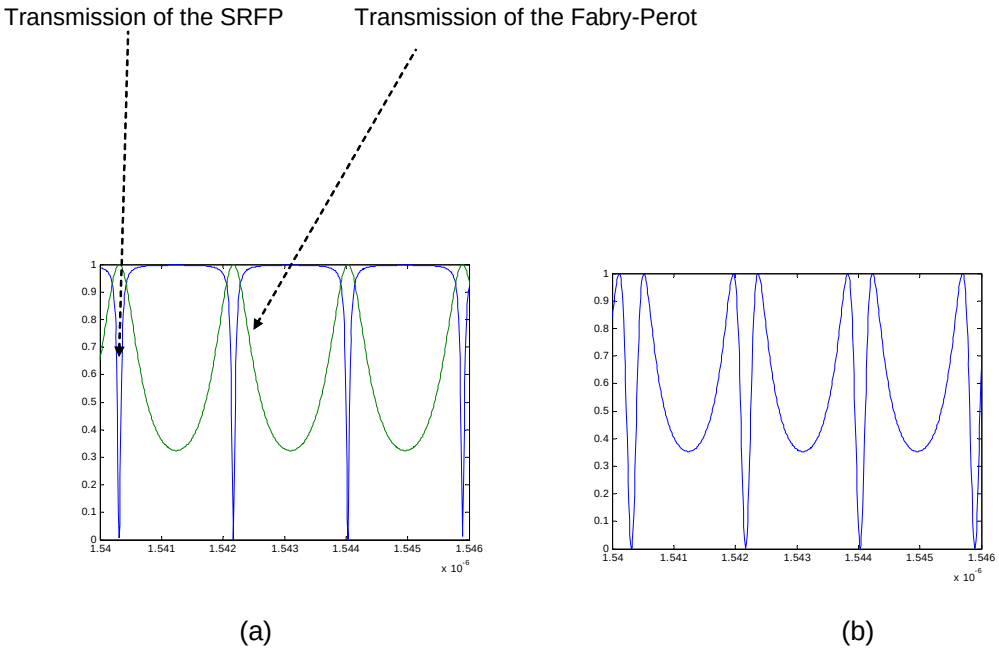

Figure 10.3: (a) Represents the transmission spectrum of the FP and the SRFP separately and (b) represents the transmission spectrum of the structure shown in fig. 5.5.

length of the SRFP resonator. In other words, when

$$L_1 + L_3 = L_2 + L_4.$$

One special case of the previous condition is

$$L_1 = L_3 = L_2 = L_4,$$

which means that the structure is symmetrical. That means that the FSR of the Fabry-Perot (without the presence of the SRFP) and the FSR of the SRFP (without the presence of the Fabry-Perot) are the same. Figs. 10.2, 10.3 depict the (reflection,

transmission) spectrum of the SRFP (without the presence of the Fabry-Perot) and the Fabry-Perot (without the presence of the SRFP) alone. It appears that a similar spectrum as shown in fig. 10.2 (b) and fig. 10.3 (b) could be obtained by just superimposing the responses of a Fabry-Perot and SRFP resonator. A node of the SRFP, Fabry-Perot corresponds to a peak of the Fabry-Perot SRFP.

10.2 Testing an ~3 dB SRFP resonator with low reflection coating

10.2.1 Testing the MMI coupler

We first tested a series of MMI couplers, which are fabricated as depicted in fig. 9.7. In addition to being interested in testing how well the couplers were working, we were also interested in looking at the interference fringes created by the discontinuities at the interfaces between the waveguides and air. Until now interest has been in looking primarily at the performance of the coupler and has ignored the interference pattern, just averaging the obtained result. The device depicted in fig. 9.7 is similar to an SRFP resonator where the HR coating is replaced by a reflection resulting from the difference of index of refraction between the waveguide and air, as illustrated in fig. 10.4. By testing the different fabricated MMI couplers we were able to measure:

- The characteristic of the coupler itself.

  and

- The characteristic of the SRFP resonator when the reflection coating does not have high reflection. We proceed here to the measurement of the reflected and transmitted lights through the device, fig. 10.4.

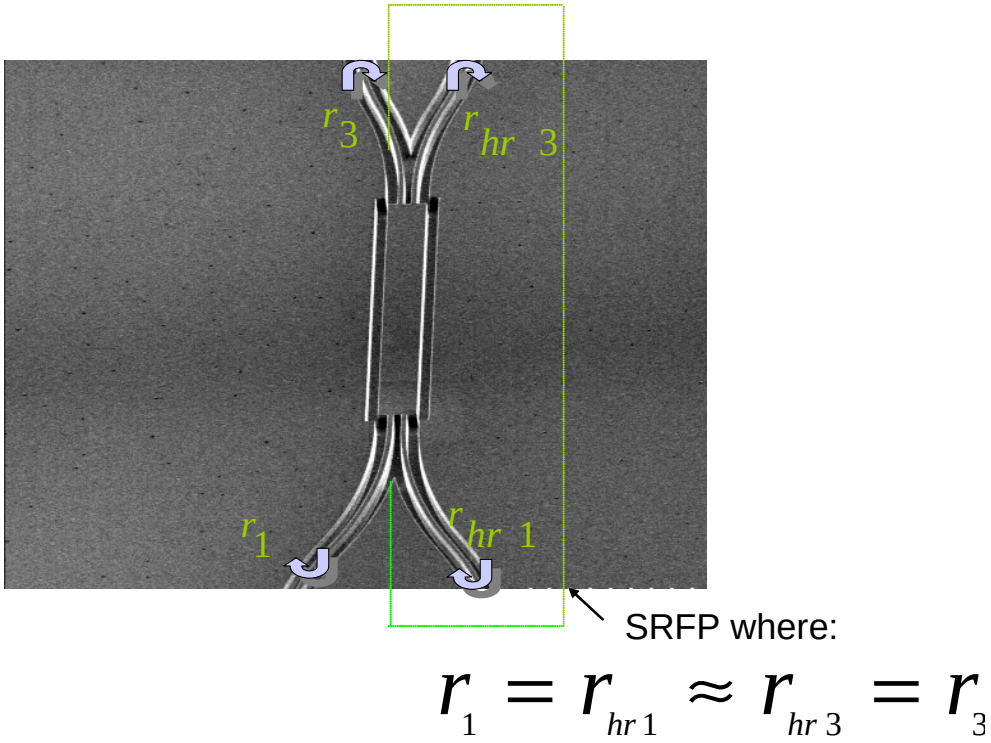

Figure 10.4: Analogy between a simple MMI coupler and an SRFP resonator.

10.3 Testing an ~3 dB SRFP resonator with high reflection coating

We report the measurement of an SRFP resonator with an estimating 3 dB coupler and a high reflection of 95% that was obtained with the deposition of different layers of AlO_3. A picture of the SRFP resonator is shown in fig.10.11. Using the T matrix model of the structure shown in figs. 5.5 was useful as a design tool guide. It tells

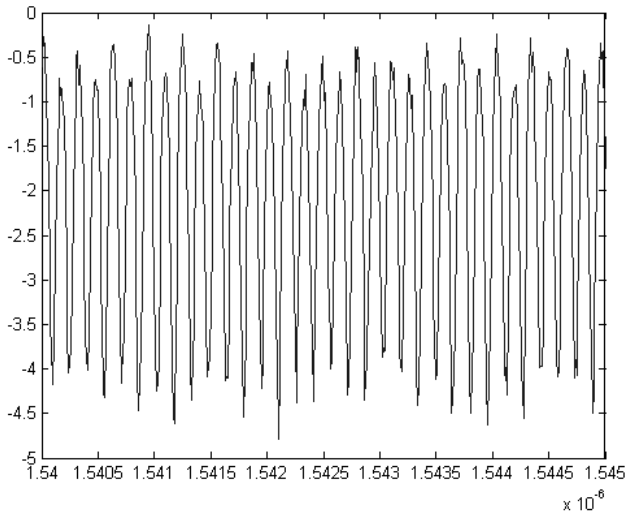

Figure 10.5: Plot in decibel (db) of the normalized reflection spectrum of the device shown in fig. 10.4 versus wavelength. Between two consecutive strong modes there is a less strong mode. This has been predicted by simulations and characterizes the existence of an SRFP inside an FP. Even in this case where the reflection coating of the SRFP has a low value, which corresponds to the reflection created between the waveguide and air interfaces, one can distinguish the contribution of the SRFP alone to the spectrum shown above. The coupler has been designed to be a 3 dB coupler. However, testing has shown that the coupling is 51% instead of 50%.

us that in order to be able to detect and differentiate the intensity spectrum of the SRFP from the ones created by the discontinuity of the waveguides (1, 3) and air, we should design our structure in such way that $L_1 = L_2 = L_3 = L_4$. In order to do so, we put marks at the places we wanted the cleaving to happen. For an accurate cleaving we used sophisticated tools.

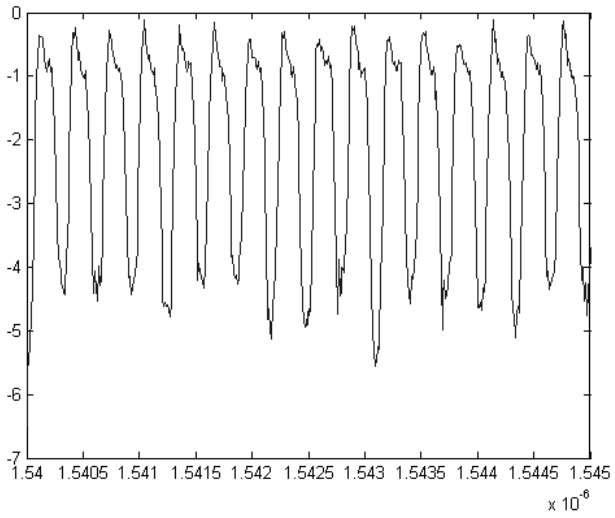

Figure 10.6: Plot in decibel of the normalized transmission spectrum of the device shown in fig. 10.4 versus wavelength. As can be seen the shape of the spectrum corresponds to that has been predicted by simulations. Similar to the reflection where we could distinguish the contribution of the SRFP alone, here also the contribution of the SRFP from the transmission spectrum shown can be easily distinguished.

10.4 Testing an SRFP with low coupling coefficient and with a high reflection coating

Finally we report on the measurement of an SRFP resonator with a high reflection facet of ~ 95 % and relatively low coupling (k ~ 0.2).

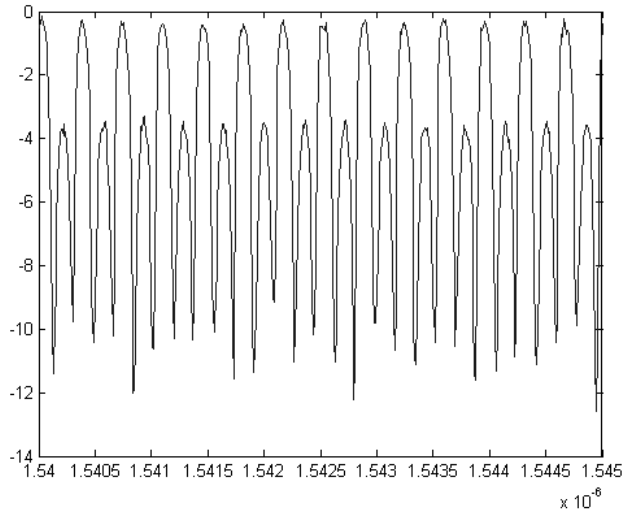

Figure 10.7: Plot in decibel of the normalized reflection spectrum of an SRFP, where the coupler has been designed to be a 3 dB coupler. The contribution of the SRFP, which corresponds the strong peaks can be clearly seen.

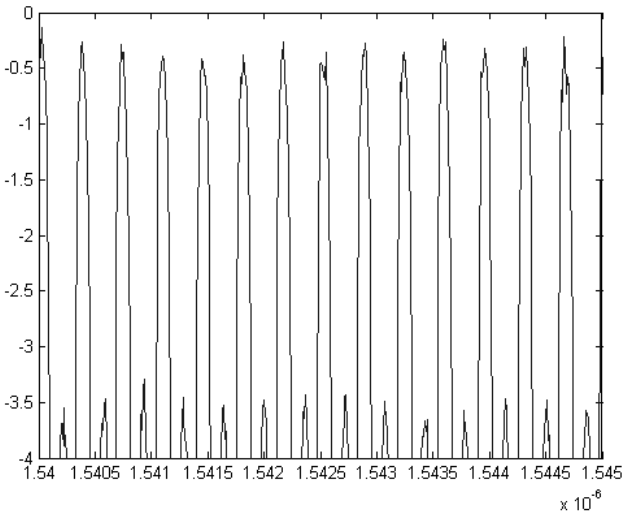

Figure 10.8: Close-up of fig. 10.7 showing the intensity contribution of the SRFP.

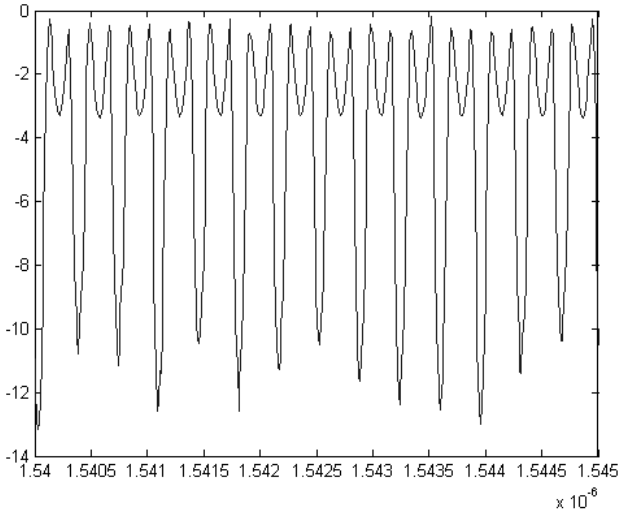

Figure 10.9: Plot in decibel of the normalized reflection spectrum of the device shown in fig. 10.11. The coupler has been designed to be a 3 dB coupler. The contribution of the SRFP corresponds to the strong peaks.

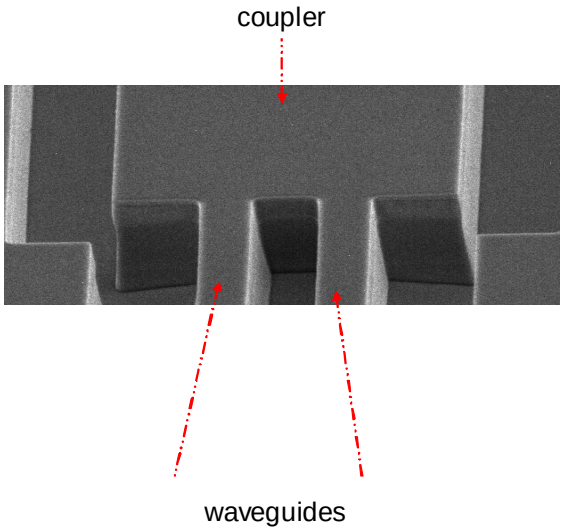

Figure 10.10: Close-up of the MMI coupler used in the SRFP.

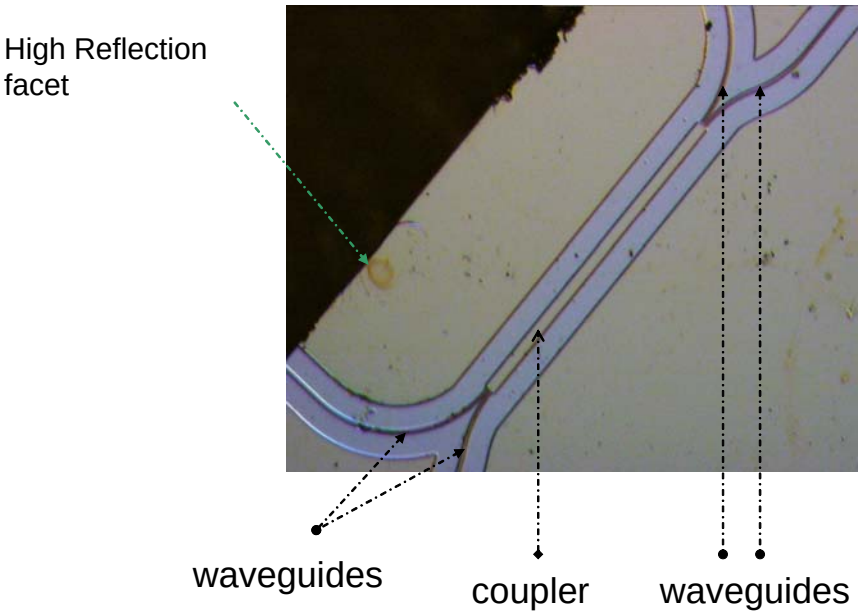

Figure 10.11: Picture of a fabricated SRFP.

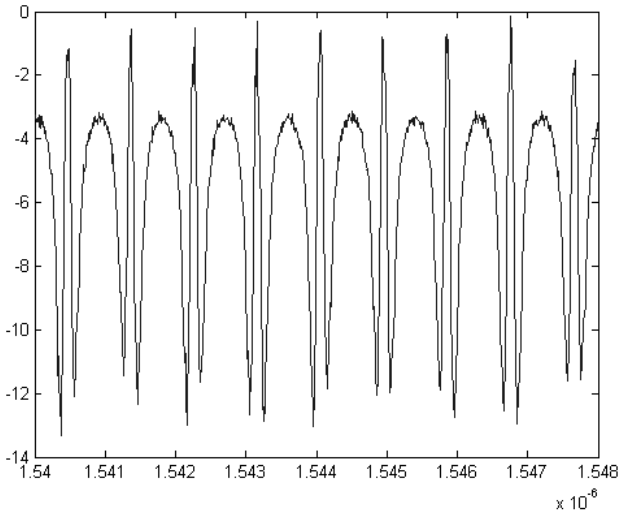

Figure 10.12: Plot in decibel of the normalized reflection spectrum of a device with high reflection coating and low coupling coefficient. The coupler has been designed to be a low coupler. The contribution of the SRFP corresponds to the strong peaks.

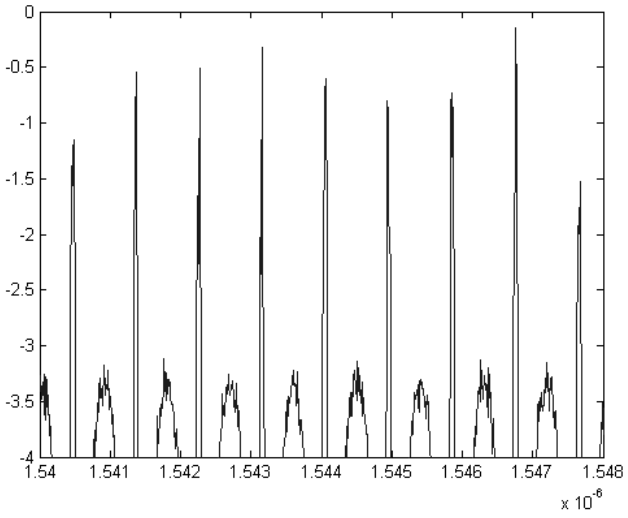

Figure 10.13: This is a close-up of the plot shown in fig. 10.12 in order to emphasize on the contribution of the SRFP to the intensity.

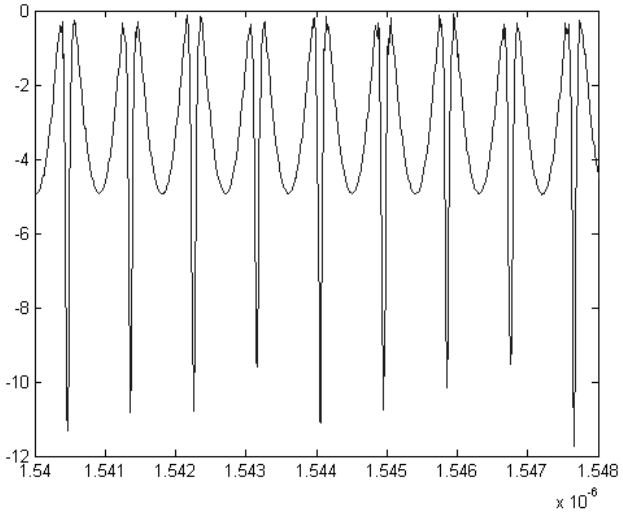

Figure 10.14: Plot in decibel of the normalized transmission spectrum of the device shown in fig. 10.15. The coupler has been designed to be a low coupler. The contribution of the SRFP corresponds to the strong peaks.

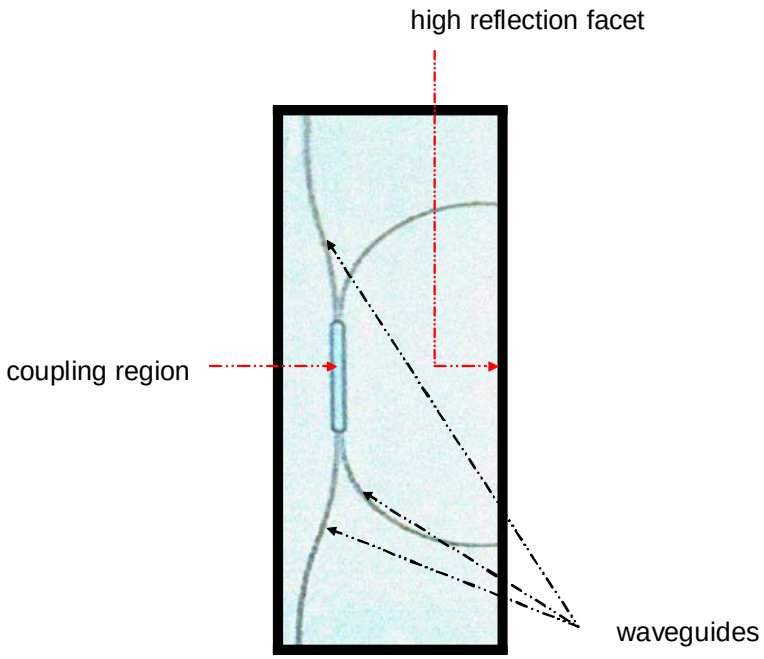

Figure 10.15: Top view of a fabricated SRFP resonator

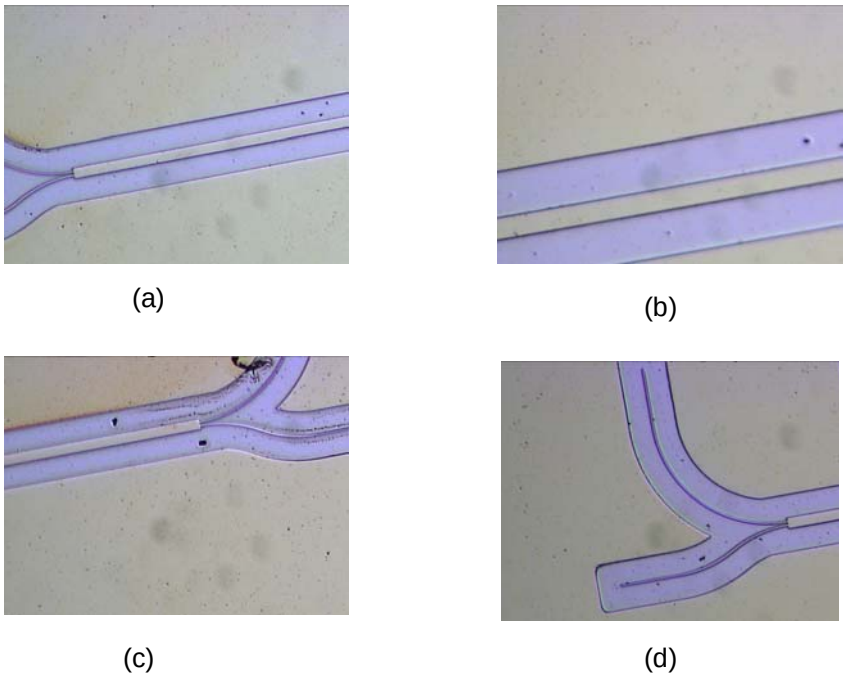

Figure 10.16: (a)-(c) represent the pictures of an SRFP resonator; (d) represents an SRFP resonator before cutting the edges

Chapter 11

SRFP Resonators Used in Delay Line Schematics

Due to limited time, we cannot investigate in depth the properieties of the SRFP resonator and different combinations of it. Delay time is crucial in many (optical and microwave) applications, some of which are

- Optical time division multiplexed [75](OTDM).
- Optical buffering.
- Phase array.

There are two major ways of creating a delay time:

The simplest way is to physically implement, which is very hard to integrate on a chip and for which tunability is hard to achieve.

The other way consists of using resonators. In that scheme, delay time can be obtained either by the material resonance where the group velocity becomes very

small, or by forcing light to travel several times a physical distance. If

$$H(w) = |H(w)|\, e^{j\phi_H}$$

is the spectrum of the resonator the time delay associated to it, is defined as

$$\tau = -\frac{d\phi_H}{dw}.$$

A resonator could be modeled as infinite impulse response (IIR), since they are based on closed loop structure. They can be divided in two groups:

Case 1 Minimum phase filter (MPF):

A filter is said to be a minimum phase filter if

$$H(z) = \frac{A(z)}{B(z)}$$

has all its poles and zeros inside the unit circle $z = 1$. The minimum phase filter are stable by definition since the poles must also be inside the unit circle; the inverse $\frac{1}{H(z)}$ is also stable when $H(z)$ is minimum of phase. $H(z)$ is minimum of phase if both $A(z)$ and $B(z)$ are minimum of phase. $B(z)$ is said to be minimum of phase if all its roots ε_i are inside the unit circle, i.e, $\varepsilon_i < 1$. Minimum-phase signals are maximally concentrated toward 0 among the space of causal signals having a given magnitude spectrum. As a result of this property minimum signals are sometimes called minimum-delay signals. In a minimum phase filter, the phase $\phi_H(w)$ is the related to the amplitude by a Hilbert transform. Therefore, large group delays are possible where there are changes in amplitude. That implies that time delay is accompanied with amplitude distortion. The minimum phase case is the one in which the impulse response $[h_0, h_1, ...]$ decays instead of grows. Minimum phase signals are maximally concentrated toward time 0 among the space of causal signals. As a result of this property MPF signals are also called *minimum delay signals*.

Examples of IIR MPF are:

- Fabry-Perot.
- Apodized fiber Bragg grating.

Case 2 Non-Minimum phase filter (Non MPF):

In these filters there are not specific relations between the amplitude and the phase. All-pass filters (APF) are an example of Non MPF. Fig. 1.3 depicts an APF based on ring resonator. APF filters have a constant amplitude response and a phase response that can be made arbitrarily. In Non MPF it is possible to have group delay while avoiding amplitude distortion. In both cases of MPF and Non MPF large time delay comes at the price of finite bandwidth over which the delay is achieved. SRFP seems to be an adequate device for delay time applications, since in transmission the SRFP can behave like a non-minimum phase IIR.

11.1 SRFP can be a non-MPF in transmission

Similar to [75]-[79], the transmission field of an SRFP $\frac{b_3}{b_1}$ expressed in equation (5.16), can be written as

$$H(z) = \frac{t_2 - \gamma z^{-2}}{1 - t_2^* \gamma z^{-2}},$$

where

$$z^{-1} = e^{-j\beta L}$$

is the delay and

$$\gamma = t_1^* e^{-\alpha L_2} r_{hr} e^{-\alpha L_4} r_{hr}.$$

$H(z)$ posseses two poles, located in

$$z_p = \pm\sqrt{t_2^*}$$

and two zeros, located in

$$z_z = \pm\sqrt{\frac{\gamma}{t_2}}.$$

When $|t_2| < |\gamma|$, the zeros lie outside the unit circle and a maximum phase behavior is achieved. The SRFP could be used optimally for dispersion compensation and delay time applications. When $|t_2| = |\gamma|$ the transmission vanishes at the resonance. When $|t_2| > |\gamma|$ the SRFP is a minimum phase filter (MPF).

11.2 Comparing the delay time of an SRFP with that of an FP and ring resonators

Since it supports standing waves, an SRFP resonator would exhibit higher time delay than a similar ring resonator with the same physical length and coupling coefficient. For the same physical length, an SRFP has an FSR that is twice than a ring with the same length since the light has to traverse twice the same trajectory in an SRFP resonator that it traverses once in a ring resonator. So an SRFP resonator could be used in every application requiring APF, and would probably increase notably the efficiency of the current state of the art device based upon ring resonators APF. Comparing an SRFP to a similar Fabry-Perot, the SRFP exhibits higher delay time in transmission since it is a non-minimum phase filter, while the Fabry-Perot is a minimum delay filter.

11.3 A 3 x 3 coupling region

We introduce here the concept of a 3 x 3 coupler having high coupling coefficient between the two resonators, and low coefficient between each resonator and the waveguide. Fig. 11.2 depicts a configuration among many others of a structure based upon the use of SRFPs. The delay time can be further enhanced in cases where the coupling coefficient between two SRFPs facing each other is high and the one between the SRFP and the main waveguide is low. It would mean that the propagation of light, which happens along the axe of the main waveguide, is slowed down. The structure of fig. 11.2 should increase notably the delay time. We can also think of using a chain of the previous setup where the delay times are additive, fig. 11.2

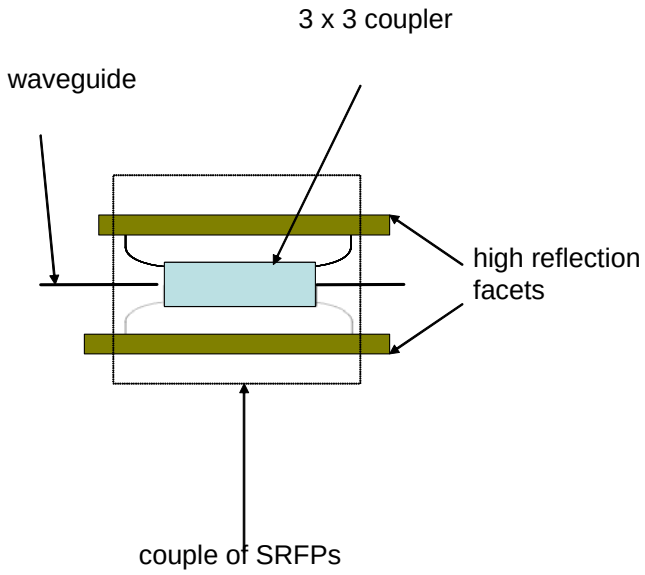

Figure 11.1: Configuration where two SRFP resonators and a waveguide are coupled to each other with the help of 3 x 3 coupler.

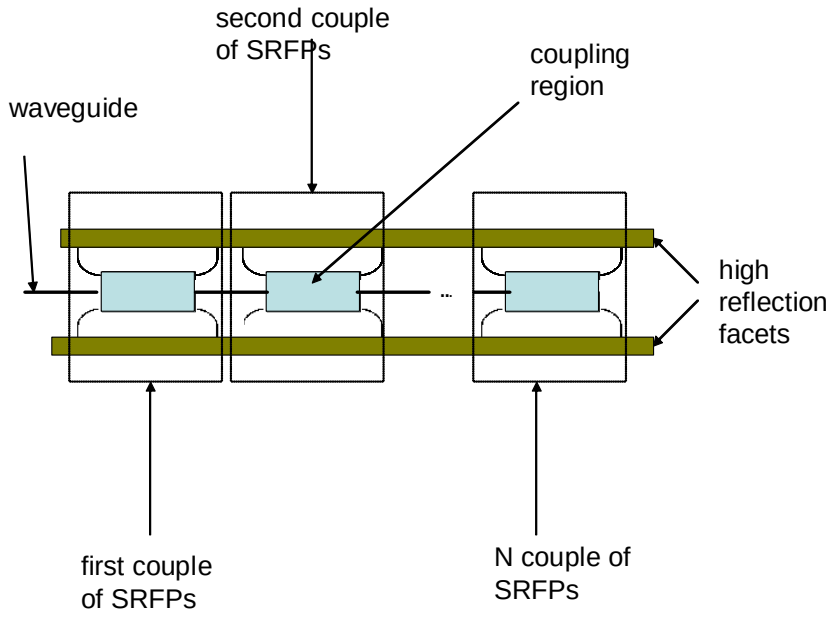

Figure 11.2: Depicts a configuration among many others of a structure based upon a heavy use of SRFPs. Most probably, this structure would exhibit a very high delay time. This would be further enhanced in the case where the coupling coefficient between two SRFP facing each other is high and the one between the SRFP and the main waveguide is low. In that case the light is traveling from one resonator to the resonator facing it. It would mean that the light would have a much slower propagation speed along the axes of the main waveguide.

Chapter 12

Combination of an SRFP Resonator with Other Resonators and Interferometers

In order to enhance the characteristic of the SRFP one could combine it with other well-known resonators and interferometers. One interesting combination is the use of a Mach-Zehnder interferometer inside an SRFP resonator.

12.1 Resonator obtained with the combination of a Mach-Zehnder interferometer and an SRFP resonator

The performance of the SRFP resonator can be further enhanced by including a Mach-Zehnder interferometer inside the resonator, fig. 12.4. The SRFP exhibits

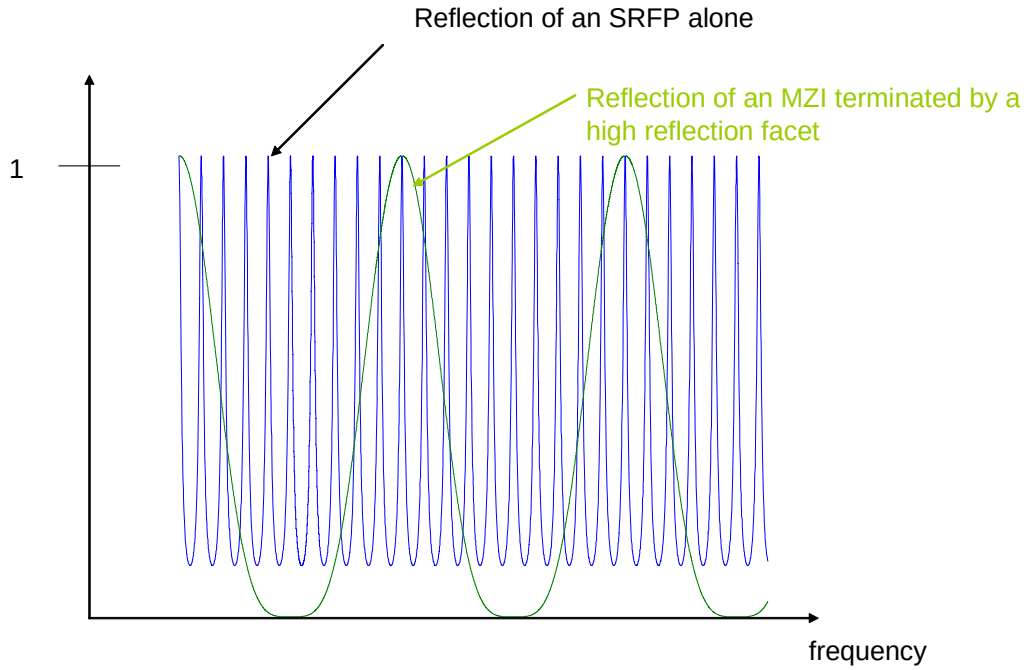

Figure 12.1: Spectrum of an MZI terminated by an high reflection facet and the reflection spectrum of an SRFP resonator.

its own (transmission, reflection) spectra having a substantially uniform peak at all resonant frequencies. The free-spectral range of an SRFP is related to its optical length. Accordingly, tuning can be achieved by shifting the peaks by an adjustment of the index of refraction in a portion of the SRFP waveguide. That could be done for example through current injection. In some applications one would like to have a tunable frequency mirror with a high mode suppression ratio (MSR). The MSR defines the energy of the strongest mode over the next strongest one. With the help of an MZI we can further enhance the performance of the SRFP in terms of MSR and tunability, assuming that the tunability range of the SRFP used alone is equal to its

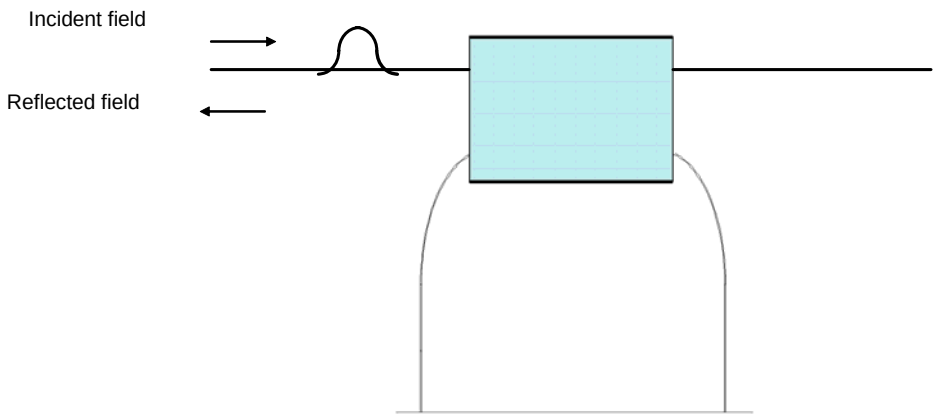

Figure 12.2: The MZI is located outside the SRFP.

free-spectral range. The MZI includes an upper arm and a lower arm that are used to establish a path length differential for the light entering. To describe intuitively the tunability mechanism one may look at the performance of the unbalanced MZI and the SRFP resonator individually and then in combination. As shown in fig. 12.1, we can use the MZI response as a rough filter and the SRFP resonator response as a fine filter. Fig. 12.3 shows the spectrum of the structure shown in fig. 12.2 where the MZI is located outside the SRFP resonator. In fig. 12.5, the spectrum of the structure shown in fig. 12.4 is plotted, where the MZI is located inside the SRFP resonator. The MZI alone produces a periodic frequency selectivity, where the large free-spectral range MZI selects a particular wavelength, which is higher that the

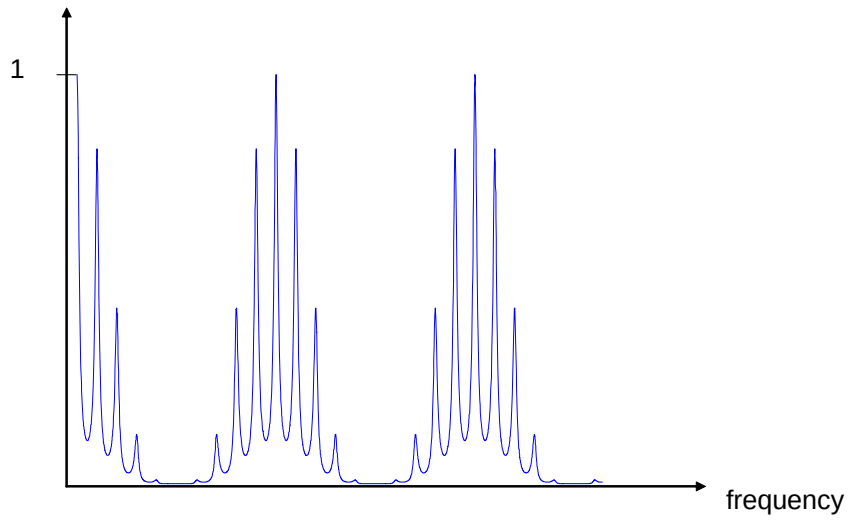

Figure 12.3: Intensity spectrum reflection of the device shown in fig. 12.2.

FSR of the SRFP resonator and which therefore defines the tunability range of the device obtained by the combination of the SRFP resonator and the MZI. However the MZI alone does not provide sufficient discrimination between neighboring cavity modes on account of its low finesse [5], [89]-[91]. Since the finesse of the MZI is constant in order to increase its selectivity (meaning the slope of its spectrum), one could decrease the FSR of the MZI. However, doing so means reducing the range of tunability of the device. So the MZI used alone does not give enough selectivity and an increase of the selectivity while maintaining the wide range of tunability are required. The SRFP provides the required selectivity. The SRFP resonator, with a small free-spectral range and higher finesse selects a particular cavity mode within

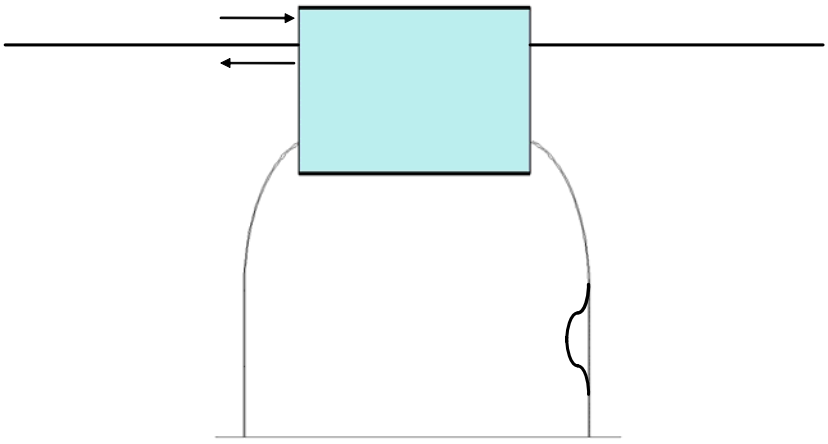

Figure 12.4: Structure where an MZI is located inside the SRFP resonator.

the wavelength region selected by the MZI. The frequency tunability is obtained by changing the difference of optical length between the two arms of the MZI, and the SRFP cavity defines the finesse of the reflector. We also assumed that the parameter are chosen such that the peaks of the SRFP resonator corresponds to the peaks of the MZI filter, which also correspond to a cavity mode of the SRFP resonator.

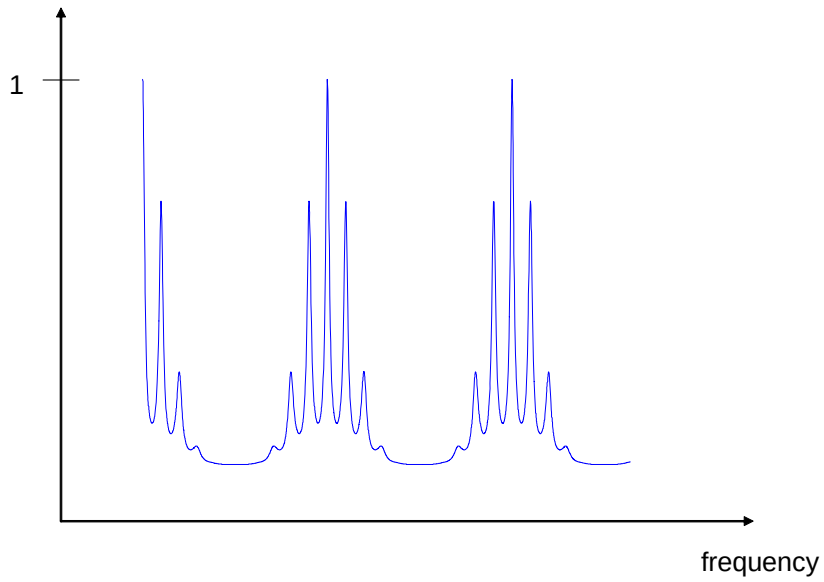

Figure 12.5: The reflected intensity spectrum of the structure shown in fig. 12.4.

12.2 Comparison of two different embodiments combining an SRFP resonator and an MZI

We would like to compare the responses of the structures shown in fig. 12.2 and fig. 12.4. In fig. 12.6 the responses are compared in the case where the MZI is located inside the SRFP (fig. 12.4) where the discrimination between the strongest peak and the next strongest peak is even further enhanced that in the case the MZI is not located inside the SRFP, fig. 12.2. This can have a real advantage in many applications, as will be discussed later.

12.3 Study of the back reflection

A study of the foregoing analysis can show that the presence of an imperfect high reflection facet, r_3, as illustrated in fig. 12.8, does not significantly deteriorate the resonator response. In addition, the effect of a back reflection, r_3, is to improve the performance of the resonator in terms of reflection and free-spectral range (the spacing between two consecutive peaks of the same intensity). Thus, the free-spectral range can be increased by changing the back reflection, rather than the resonator optical length. Figs. 12.9 and 12.10 illustrate different cases where the presence of a back reflection is an advantage. The green curve represents the reflection field without the back reflection and the blue one with the back reflection. As shown, in the case where the lengths of waveguides 1, 3 ,4 are a multiple of each other, the reflection of the SRFP is greatly enhanced in terms of intensity and FSR by the presence of the back reflection.

12.4 Other embodiments combining an SRFP resonator with other resonators

In the previous sections we studied a few embodiments using combinations of SRFPs with other resonators. There are many other embodiments that could be of interest in future applications. Fig. 12.11 depicts several of these embodiments.

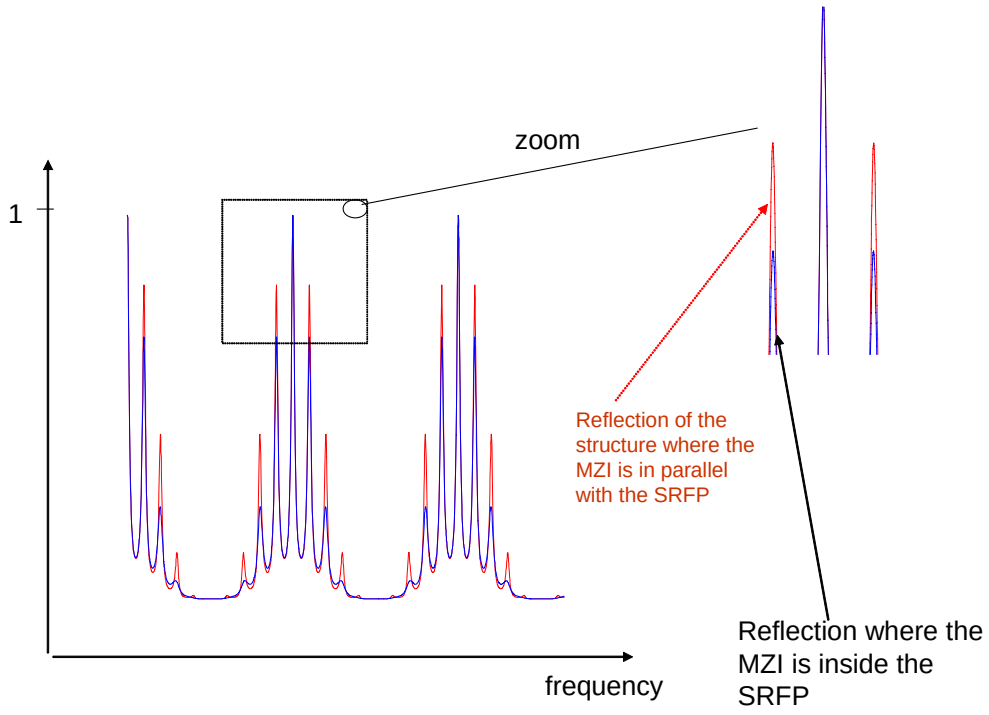

Figure 12.6: Comparison of the response of the structure where the MZI is located outside the SRFP resonator (shown in fig. 12.2) and the structure where the MZI is located inside the SRFP (shown in fig. 12.4). In the case where the MZI is located inside the SRFP, the difference between the strongest mode and the next strongest mode is further enhanced.

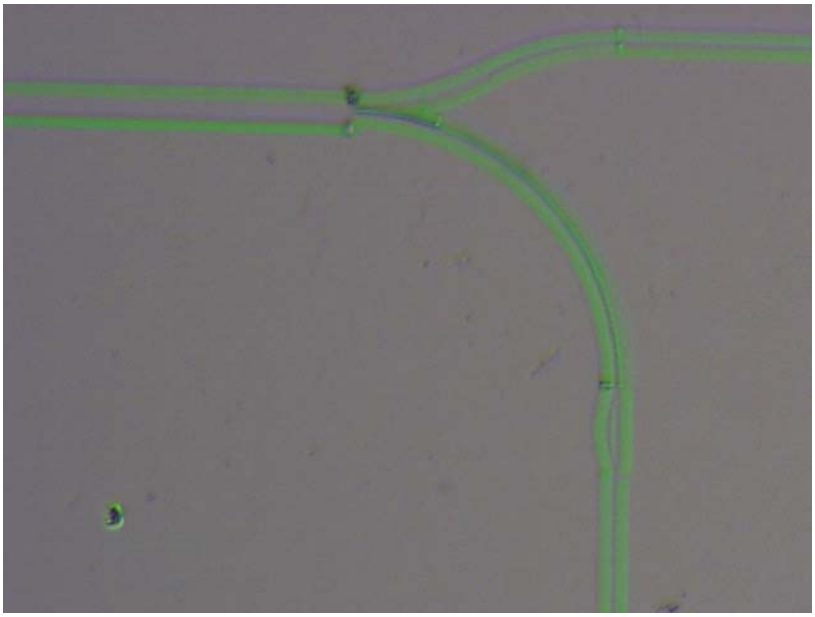

Figure 12.7: Mach-Zehnder interferometer inside SRFP resonator. This picture has been obtained after devloping the electron beam lithography.

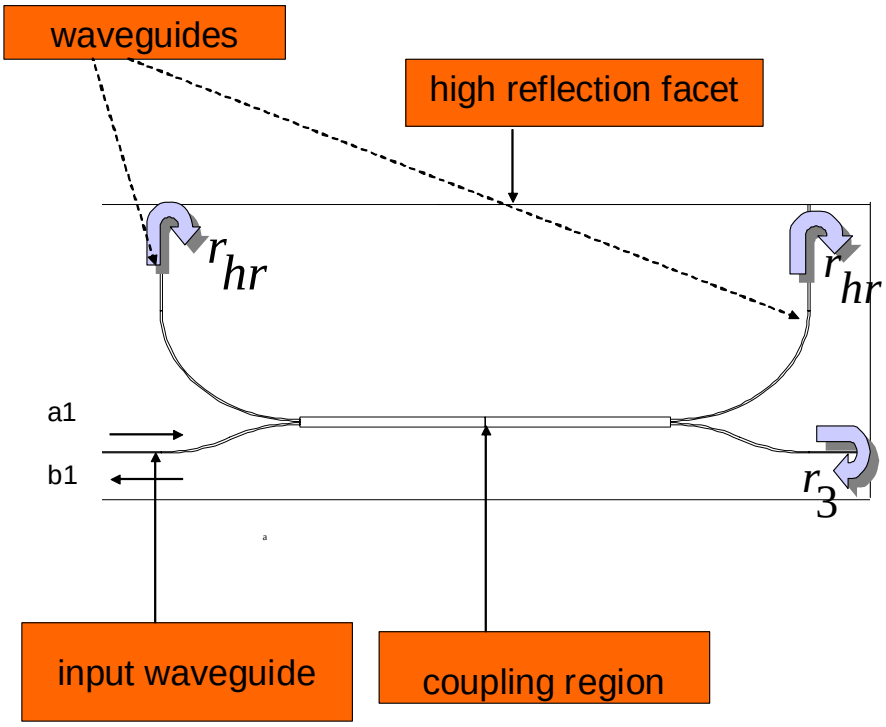

Figure 12.8: Illustration of an embodiment combining an SRFP resonator and back mirror.

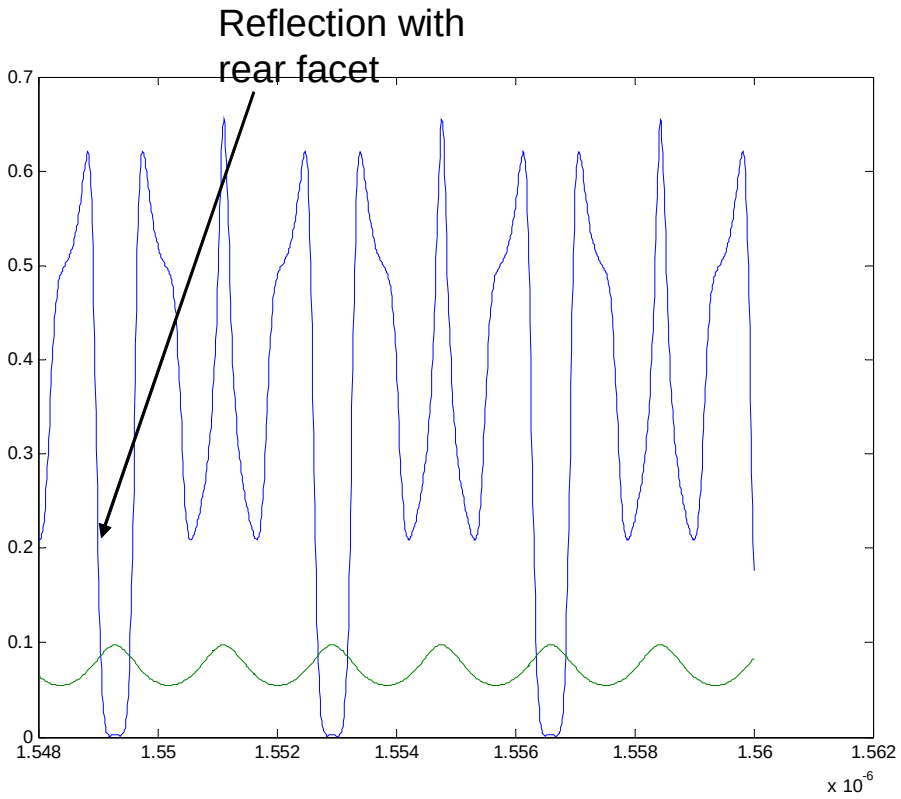

Figure 12.9: Illustration of both the reflection intensity with and without a rear facet versus the wavelength. The rear facet reflection is assumed to be equal to 0.99 and HR facet reflection corresponding to the natural reflection appearing between the semiconductor air interface and $L_3 = 4L_2$.

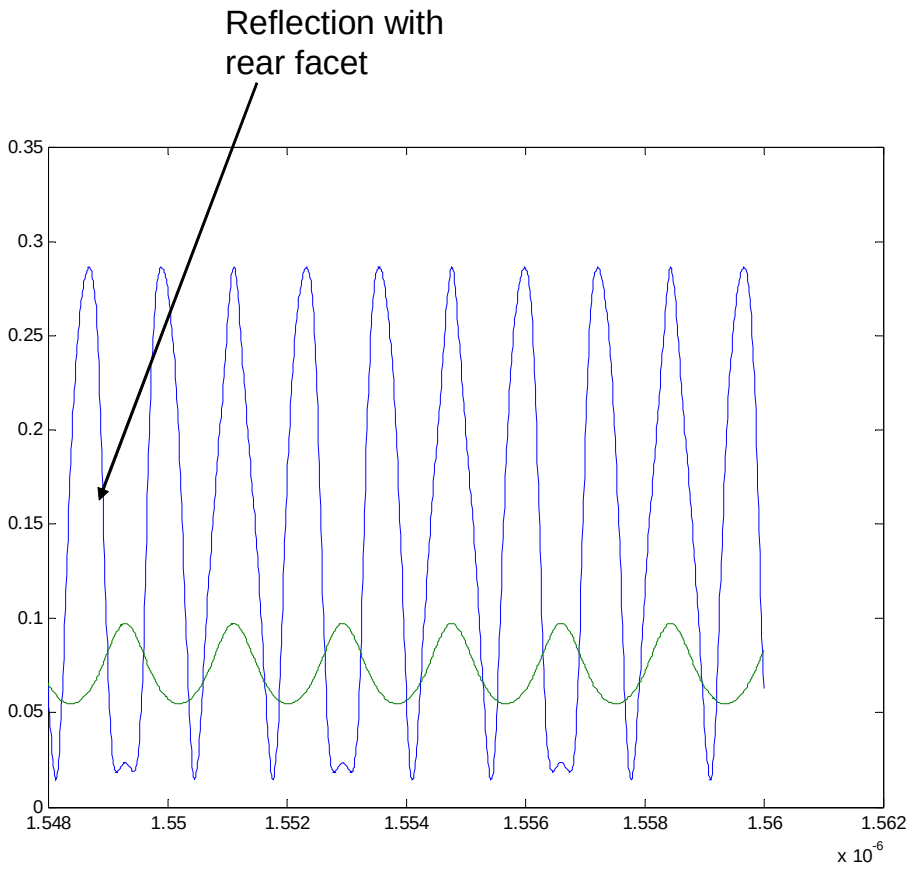

Figure 12.10: Illustration of both the reflection intensity with and without a rear facet. The rear facet reflection is assumed to be equal to the SRFP facet reflection HR facet reflection, which corresponds to the natural reflection appearing between the semiconductor air interface and $L_3 = 4L_2$.

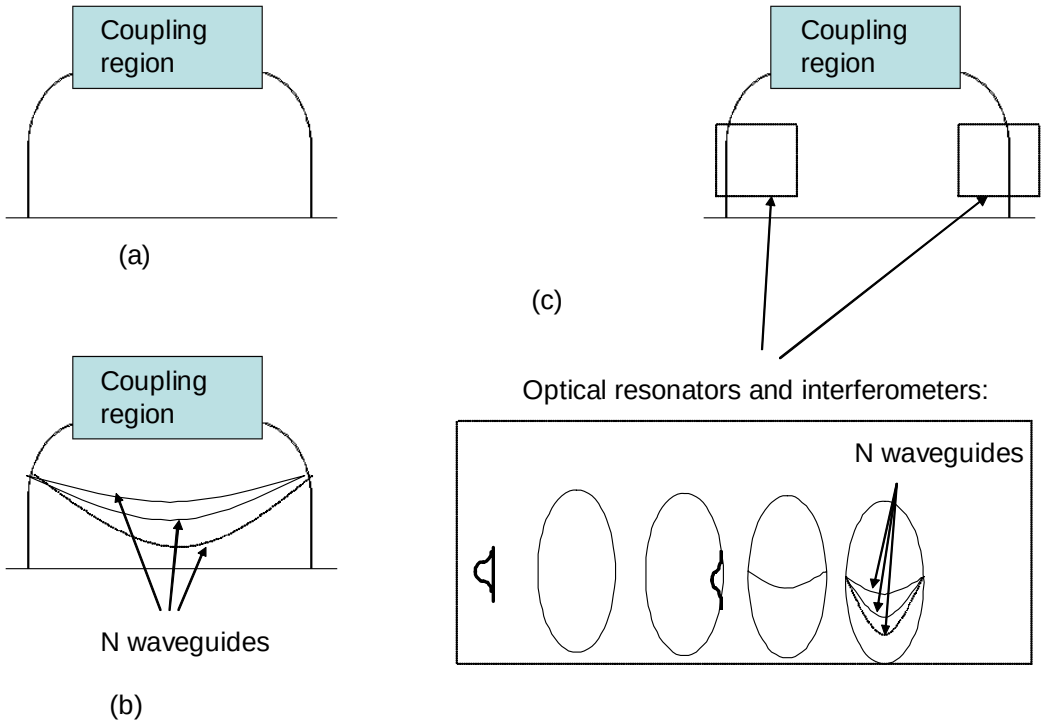

Figure 12.11: Case (a) depicts a single SRFP, (b) depicts the combinations of an SRFP with waveguides of different lengths, (c) depicts combinations of an SRFP with other resonators and interferometers. The dashed box represents several examples (among many others) of resonators and interferometers that could be combined with the SRFP.

Chapter 13

SRFP Resonator Used as Modulator

Fig. 13.1 proposes a modulator, which operation is similar to the one described in [39], but differs from it by replacing the ring resonator with an SRFP resonator. The modulation is obtained either:

- By modulating the coupling coefficients. One way of doing so it to use an MZI within the coupling region as depicted in fig. 13.1. Between the two arms of the MZI a phase shift is introduced.
- By modulating the loss (or the gain) within the SRFP resonator.

The advantage of such a modulator over the conventional modulators such as an MZI is it requires a small phase shift between the two arms of the MZI to switch from an "on" state to an "off" state, therefore requiring less energy and switching time between on and off. This structure exhibits the same kind of advantages as

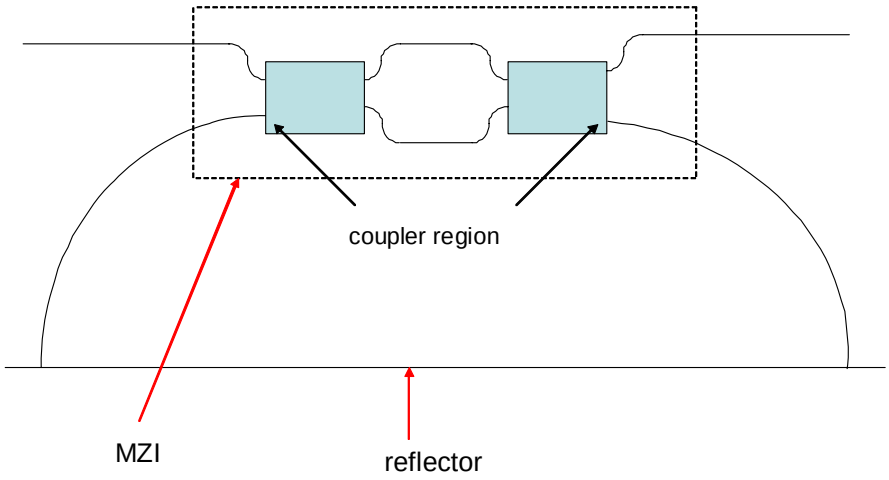

Figure 13.1: An SRFP modulator obtained with the help of an MZI within the coupling region.

the device described in [39]; however, there are several advantages in using an SRFP resonator instead of a ring resonator.

The main advantage of the structure that we proposed over the one using a ring resonator [39] is that the device can be used either as a modulator in transmission or reflection, whereas the modulator combining the ring resonator and the MZI can just be used in transmission.

Chapter 14

Different Laser Applications of the SRFP Resonator

Presented here are some novel tunable semiconductor lasers. One of the many advantages of these embodiments is the requirement for only simple planar fabrication technology. Thus, embodiments of these devices require no grating structure or moving parts. Using a complex field approach, it can be demonstrated that relatively wide tunability, high optical power, and large mode suppression ratio (MSR) can be achieved through a careful design employing a simple architecture. The mode suppression ratio exhibited by some proposed embodiments (even in the case of a bad coupling, e.g. approximately 3 dB , coupling between the gain chip and the tunable mirror) is still higher than that obtained with standard designs of tunable lasers based on interferometer techniques. Such standard designs exhibit typical MSRs around 30 to 40 dB . For an ordinary Fabry-Perot cavity in a laser device, lasing is a function of the cavity optical length and typically only occurs near the top of the gain profile of the gain medium. Because adjustment of the cavity optical length is limited, there is no simple technique for tuning over a wide range. In addition, the cavity typically has a relatively broad gain profile, making it possible to have lasing

at more than one frequency. In order to select a single frequency for operation, it is necessary to introduce a frequency-selective mirror device.

14.1 Analysis of a laser using a single SRFP resonator with an MZI

Fig. 14.1 illustrates a top view of two tunable laser embodiments including an SFRP tunable element, an MZI (and a reflective facet in case (b)). The tunable laser device comprises a tunable feedback element within a Fabry-Perot cavity. The tunable feedback element comprises an MZI within an SRFP resonator. There is a gain medium within a waveguide bounded by reflective facets, a rear facet, and a front facet at opposing ends of the gain medium. The front facet, bounding the opposing end of the cavity, comprises the output of the tunable laser device (MZI+SRFP). As is well known in the art, the gain medium can include a phase shifter to adjust phase of the laser mode to coincide with a gain peak in order to tune the laser. This fundamentally applies to all laser embodiments presented herein. There are different means of coupling the gain medium to the tunable feedback element. However, the nature of the coupling is not important for the description of the device. So the proposed tunable element is created by the combination of an MZI inside an SRFP resonator cavity. As discussed earliear, the large free-spectral range MZI selects a particular wavelength region within the gain bandwidth, but this interferometer does not provide sufficient discrimination between neighboring cavity modes [5]- [91]. But first we must understand qualitatively how the laser shown in fig. 14.1 works.

14.2 Qualitative description of the tunable laser

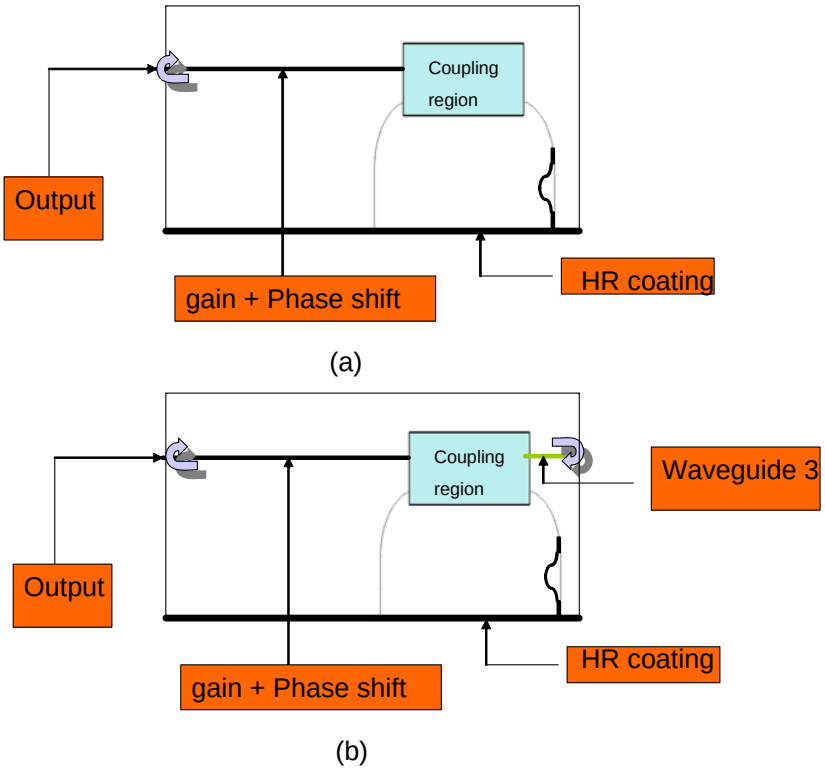

Figure 14.1: Illustration of the top view of a tunable semiconductor laser where the tunable frequency mirror is obtained with the combination of an MZI inside an SRFP resonator (a). In (b) in addition to the combination of an MZI with an SRFP we also use a rear facet.

To describe intuitively the tunability mechanism one may look at the performance of the unbalanced MZI and the SRFP resonator individually and then at the combination of the two. For a laser that consists simply of a gain medium and a straight extension ending with a flat mirror, the acceptable frequencies (cavity modes) are those that satisfy equation (14.1):

$$\nu = \frac{mc}{(n_g L_g + n_l L_l)}, \tag{14.1}$$

where n_g and n_l are the propagation constants and L_g and L_l are the physical lengths of the gain and extension sections respectively. But, in the best case scenario the

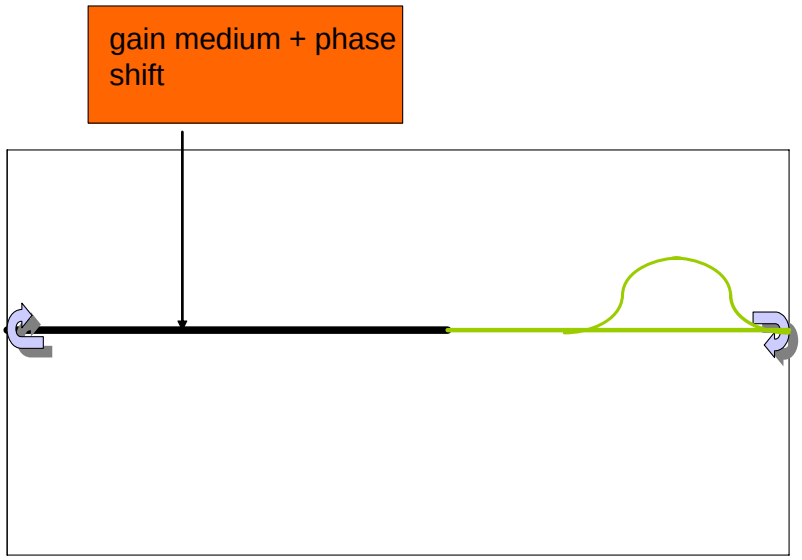

Figure 14.2: Depicts a tunable laser, where the tunable mirror is composed with the combination of an MZI in addition to a reflection.

range of tunability available is equal to the FSR of the Fabry Perot resonator composed with the combination of the gain medium and of its rear and front facet. In reality, such a range of tunability is not possible since changing the optical length of the gain medium would also shift the gain profile spectrum. In this case one would like to have a laser delivering sufficient power, therefore the length of the gain medium would have to be extended, which would result in a decrease of the available tunable range (since the FSR will decrease as the length of the medium increases). In order to achieve single frequency operation, it is necessary to introduce a frequency selective feedback element such as the MZI, as depicted in fig. 14.2. Consider an

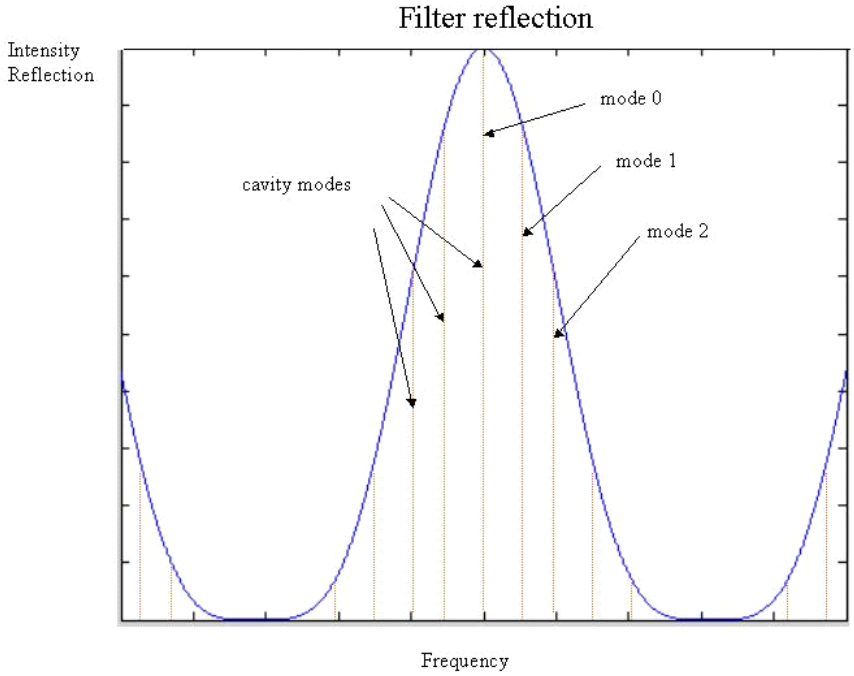

Figure 14.3: Illustration of the mode filtering by the MZ interferometer filter.

MZI with an upper and lower arm length. In the structure shown in fig. 14.2, the MZI reflectance is a periodic function of the optical frequency f :

$$R = \cos(\pi f \frac{\Delta(nL)}{c})^4,$$

where $\Delta(nL)$ is the difference of optical path length between the two arms, f the optical frequency, and c the speed of light. A 2π phase change in one arm tunes the filter by one free spectral range, $FSR = \frac{C}{\Delta(nL)}$. The optical path length difference $\Delta(nL)$ is the key parameter of the MZI filter. The cavity mode selection by the MZ interferometer is shown schematically in fig. 14.3. In an optimum case the peak of the MZI corresponds to a cavity mode. For a given device length, larger FSR results in a larger tuning range, but at the expense of the selectivity between the

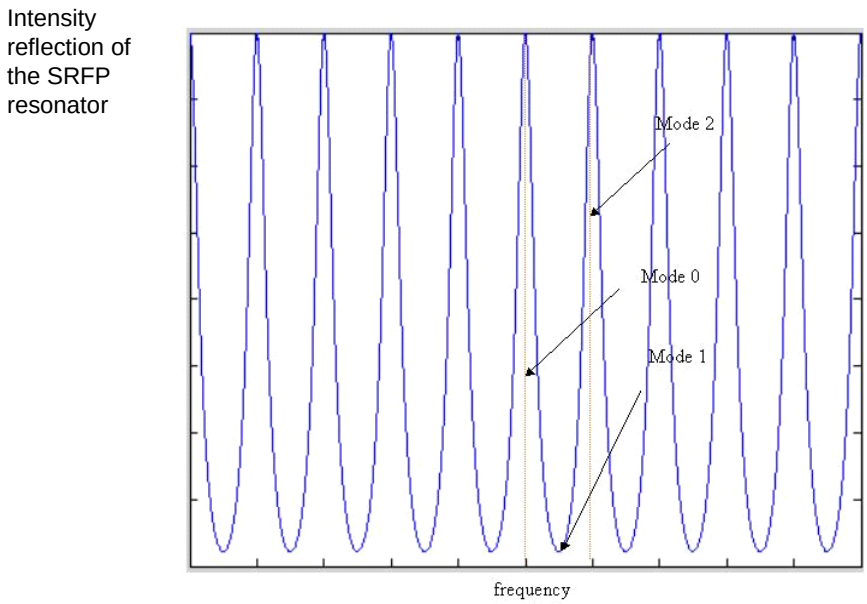

Figure 14.4: Illustration of the reflected intensity from the SRFP resonator and the location of the different modes of the device.

main and the side modes. Therefore, considering the concept of mode suppression ratio (MSR), which expressed the ratio of the energy stored in the main mode over the energy stored in the side mode, one sees that devices similar to the one shown in fig. 14.2 as the Y-branch laser, do not have high MSR due to the low finesse of the MZI.

14.2.1 Adding the SRFP resonator to the MZI

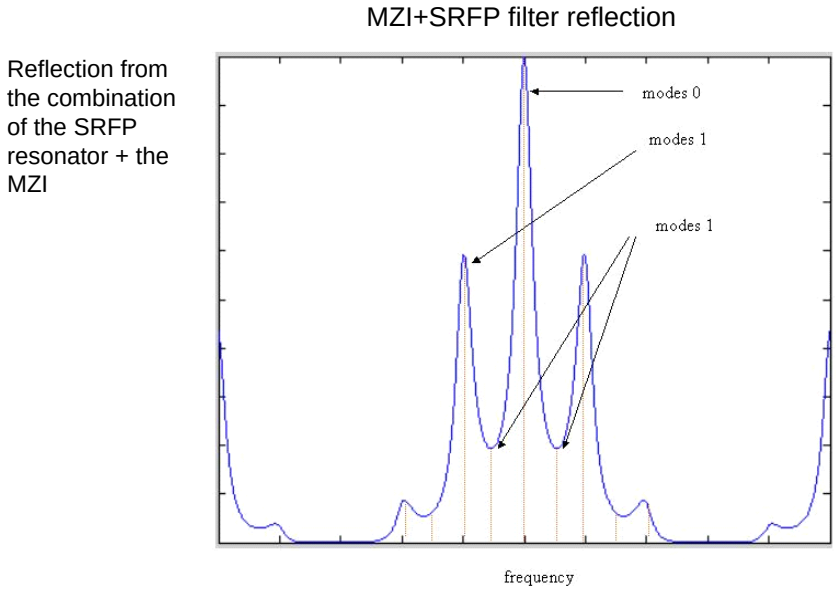

Figure 14.5: Illustration of the filtering of the modes of the laser by the combination of the SRFP resonator and the MZI.

The MZI used alone does not give enough selectivity. An increase of the MSR while maintaining the wide tuning range is required. Therefore, a more sensitive cavity side modes filtering is needed. The ring resonator in series with the MZI provides the needed selectivity. The reflection of the SRFP is shown in fig. 14.4. The SRFP resonator exhibits the advantage of being readily integrated with other components in an optical circuit. As shown in figs. 14.3 and 14.4, in an optimum design one of the peaks of the SRFP corresponds to the peak of the MZI filter, which corresponds to a cavity mode. This mode, which is called mode 0, will be the lasing mode. In order to understand the operation of the SRFP resonator we assume the worst case,

in which each one of the SRFP peaks corresponds to a cavity mode. The SRFP resonator should be designed in a way to filter all the cavity modes between the main mode and the next ring resonator peak. That means if mode 0 is the lasing mode, mode 1 the next cavity mode, and mode 2 the cavity mode that is aligned with the next peak of the SRFP, mode 2 should become the side mode. Without the use of the SRFP resonator, mode 1 is the side mode, as shown in fig. 14.3.With this implementation, the MSR is no longer a function of the ratio of mode 0 over mode 1, but a function of the ratio of mode 0 over mode 4, making the MSR a function of the SRFP resonator FSR and MZI gain envelope.

14.3 Engineering a single SRFP laser

This section covers the engineering of the tunable frequency mirror together with the gain section in order to produce a widely tunable single-mode laser as described in fig. 14.1. Although embodiments of the laser can be constructed as hybrid devices with distinct elements separately fabricated and integrated together, the devices can advantageously be used to form optical devices through monolithic fabrication in a simpler more cost-effective manner. One can examine a specific design in which the active medium is a III-V material system operating at approximately 1.55 μm wavelength. For this specific exemplary numerical application, an MZI free-spectral range (FSR) of approximately 1,248 GHz (equivalent to a tunability range of approximately 1,248 GHz (10 nm)) is chosen. A fine wavelength selection of approximately 50 GHz is considered. This is the frequency difference between two consecutive frequencies of the laser channels and, in turn, corresponds to the total combined length of the SRFP resonator of approximately 1 mm. It can also be assumed that the gain medium is substantially removed from the tunable filter so that the waveguide loss reaches a maximum value of approximately 10 dB/cm, are substantially equal and

equal to approximately 0.97, and are essentially equal to 0.7. The main reflection of the tunable filter is taken to correspond to a cavity mode, which is the laser mode. The 10 dB/cm loss is applied as a worst case estimate for evaluation purposes; realistic losses may be lower in many applications, depending upon manufacturing and other considerations. Referring to fig. 14.5, it is also assumed that the separation of the cavity modes is such that the reflection of the adjacent cavity mode from the tunable filter element is lower than that of the cavity mode, coinciding with the next strongest reflection peak of the tunable filter element. In the calculation of the MSR, a worst scenario is assumed in which both the strongest and next strongest field reflection peak spectrum of the tunable filter element correspond to a cavity mode. The contribution of the filter reflection to the energy stored in each mode is included only in order to calculate the single contribution of the tunable filter element in the MSR. This means that these calculations represent a pessimistic view where the same gain is present both for the main and side modes. In reality, this is not truly the case because the side-mode gain is relatively flat. Fig. 14.6 (a) illustrates the intensity coming back from the tunable frequency element versus frequency of the exemplary embodiment of fig. 14.1 (a). A fine wavelength selection FSR of approximately 50 GHz and an MZI FSR of approximately 1,248 GHz are applied. In addition, an intensity coupling between the gain-tunable element of approximately 0.49 and a waveguide loss of approximately 10 dB/cm are also used. The considered gain medium parameters of the exemplary embodiment of fig. 14.1 (a) are approximately 0.2 μm thickness, 3 μm width, 300 μm length and have a material loss of approximately 80/cm. The gain versus carrier density characteristic of the active medium is associated with a transparency carrier of approximately $5\times10^{-16}\text{cm}^3$. According to [40], the threshold current is given by

$$I_{th} \tilde{} \frac{qVBN_{tr}^2}{\eta_i} e^{\frac{2(<\alpha_i>+\alpha_m)}{\Gamma g_0}},$$

where V is the volume of the η_i the quantum efficiency (in our case its value is approximately 0.7), N_{tr} is the transparent coefficient of approximately $2\times10^{18}\text{cm}^{-3}$,

α_i is the gain medium intrinsic loss (approximately 80 cm^{-1}), B the bimolecular recombination coefficient (usually $10^{-10}cm^3/s$ for most III-V materials of interest). A passive waveguide loss of approximately 10 dB/cm, a confinement factor of approximately $\Gamma = 0.7$ and a differential gain of approximately $5\times10^{-16}cm^2$ are also applied. The mirror loss is given by the following:

$$\alpha_m = \frac{1}{L_{activemedium}} \ln\left(\frac{1}{r_3 r}\right),$$

where $r_3 = \left|\frac{b_3}{a_3}\right|$ is the reflectivity from the strongest peak of the tunable frequency mirror, $r = 0.3922$ is the output facet field reflectivity of the tunable laser. Fig. 14.6 (b) is a plot of the MSR versus the current in amperes for the exemplary embodiment of fig.14.1 (a). According to [40], the MSR can be given by

$$MSR(db)\tilde{}10\log_{10}\left[\frac{\Delta\alpha + \Delta g}{\partial G} + 1\right], \tag{14.2}$$

where ∂G is the separation between the mirror loss and the net modal gain for the main mode and is given by

$$\partial G\tilde{}\frac{10^{-3} I_{th}}{I - I_{th}}\ cm^{-1}. \tag{14.3}$$

$\Delta\alpha = 91.4\ m^{-1}$ is the loss margin and $\Delta g = 0$ is the modal gain margin. Proceeding in this way, $I_{th} = 20.2$ mA. Fig. 14.6 (c) is a plot of the output power in watts versus the input current in amperes for the exemplary embodiment of fig. 14.1 (a). The output power is given by

$$P_0 = \eta_i \left(\frac{\alpha_m}{<\alpha_i> + \alpha_m}\right) \frac{h\upsilon}{q} (I - I_{th}) \ \ for\ (I > I_{th}), \tag{14.4}$$

where h is the Planck constant. A much greater MSR can be achieved if the 3 dB coupler is replaced with a low coupling coefficient coupler.

14.4 A laser using SRFP resonators on opposite sides of the gain medium

Fig. 14.7 illustrates a top view of an exemplary laser embodiment where both resonators comprise SRFP resonators. The resonant frequencies of the laser are those that correspond both to the resonant frequencies of the two SRFP resonators and to a cavity mode of the gain medium. The frequency tunability of the laser is obtained by changing the difference of optical path length of one of the SFRP resonators to employ a Vernier effect as described above. As with the underlying SFRP resonators a laser according to the embodiment of fig. 14.7 employs relatively simple fabrication technology and does not require any grating structure or moving parts. When compared with a known double ring-resonator coupled laser (DR-RCL), [92] the waveguides composing the SFRP resonators obtain lower curvature. This not only better facilitates fabrication but also reduces the losses related to the bending of the waveguides. Also, because the FSR of resonators in general is inversely proportional to the length of the cavity, if a high FSR resonator is desired, the length of the resonator should be decreased. In the case of ring resonators, the minimum affordable length of the resonator will be effectively determined by the waveguide's bending loss. Because the waveguide's bending is lower in the present SFRP resonators than in ring resonators, a higher resonator FSR should be obtainable with the laser shown in fig. 14.7. The laser of fig. 14.7 comprises three main regions: a gain medium and two passive SRFP resonators. There are different techniques for coupling the gain medium to the SRFP resonators as previously discussed. However, the nature of the coupling is not critical for the analytical study of the laser. The gain medium provides light amplification. Each SRFP resonator has a uniform peak transmission at all resonant peaks if we exclude material dispersion. Their FSR is related to their optical length. The two SRFPs have slight different optical lengths,

thus providing the mode selection and the wavelength tuning mechanism. Therefore, the two SRFP resonator tuning technique (which is based on the Vernier technique) is achieved by aligning the peaks in the two sets of resonator combs with the adjustment of index in one or both SRFP resonators. The proposed device can be compared to both the known sampled grating-distributed Bragg reflector (SG-DBR) laser and to the double ring-resonator coupled laser (DR-RCL). However, the laser shown in fig. 14.7 uses SRFP resonators, on opposing sides of the length of gain medium. In contrast, SG-DBR lasers employ sampled gratings on opposite sides of a length of gain medium and DR-RCL uses ring resonators on opposite sides of a length of gain medium. As we have studied in depth in the first chapter the SRFP exhibits many advantages over both the ring and the Fabry-Perot resonator. One advantage of the SRFP resonator over the standard ring resonator is its support of standing waves (and larger waveguide bending curvature as previously discussed). This allows the device the use of only one coupling region in order to couple light from the SRFP resonator back to the gain medium. Further, the advantage of the SRFP resonator over the standard Fabry-Perot resonator is the use of only one facet. This eases the fabrication constraints on the SRFP resonator; the length of the SRFP may greatly differ from that of the chip. Thus, the FSR of the SRFP resonator is not strongly dictated by fabrication requirements as with conventional Fabry-Perot resonators. As SRFP resonators produce an essentially uniform peak transmission at all resonant peaks, the uniform thresholds and efficiencies between the different operating wavelengths are basically the same. Consequently, the laser of fig. 14.7 and the DR-RCL are nearly analytically equivalent and, accordingly, the laser should exhibit at least the same advantages in terms of performance (such as tunability and MSR) as the DR-RCL if manufactured properly. However, the performance of this laser should be higher in term of MSR because the reflection intensity of an SRFP has higher finesse than a ring resonator, especially when one uses the back reflection resulting from the discontinuity between the waveguide and air. In addition, the laser

of fig. 14.7 exhibits additional positive features. For example, it allows a reduction in the number of coupling regions as well as the elimination of absorption regions. Indeed, reflection problems related to the discontinuity between the absorption region and the passive waveguide in DR-RCL devices are avoided. Furthermore, as previously mentioned, the overall design has the advantage of planar fabrication and does require any grating structure or moving parts.

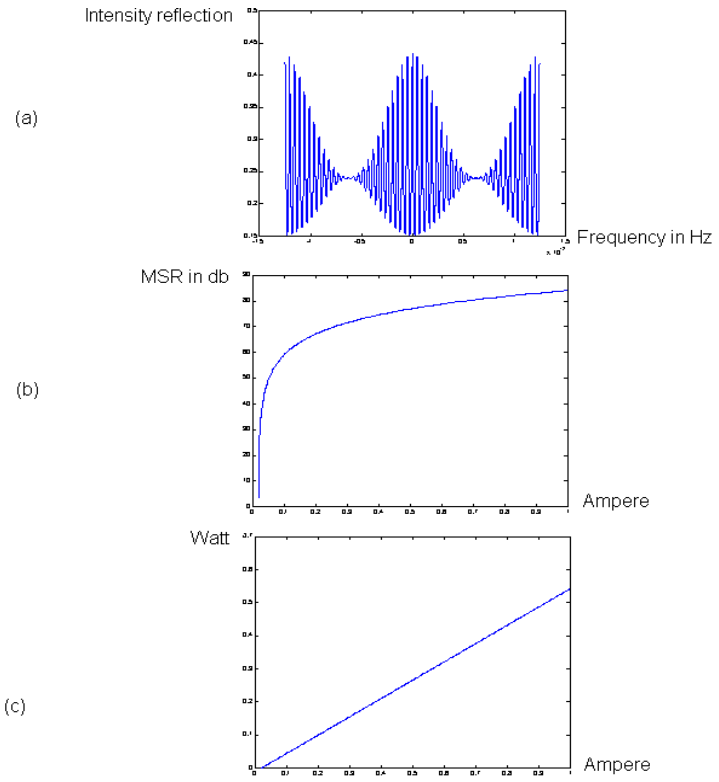

Figure 14.6: The set of fig. 14.6 is related to the numerical application treated in this paragraph. Fig. 14.6 (a) represents the intensity coming back from the tunable frequency element versus frequency, (b) represents the MSR in dB versus the current in ampere, (c) represents the output power of the device in watts versus injected current in amperes. We did not take into account nonlinear effects, which limit the output power.

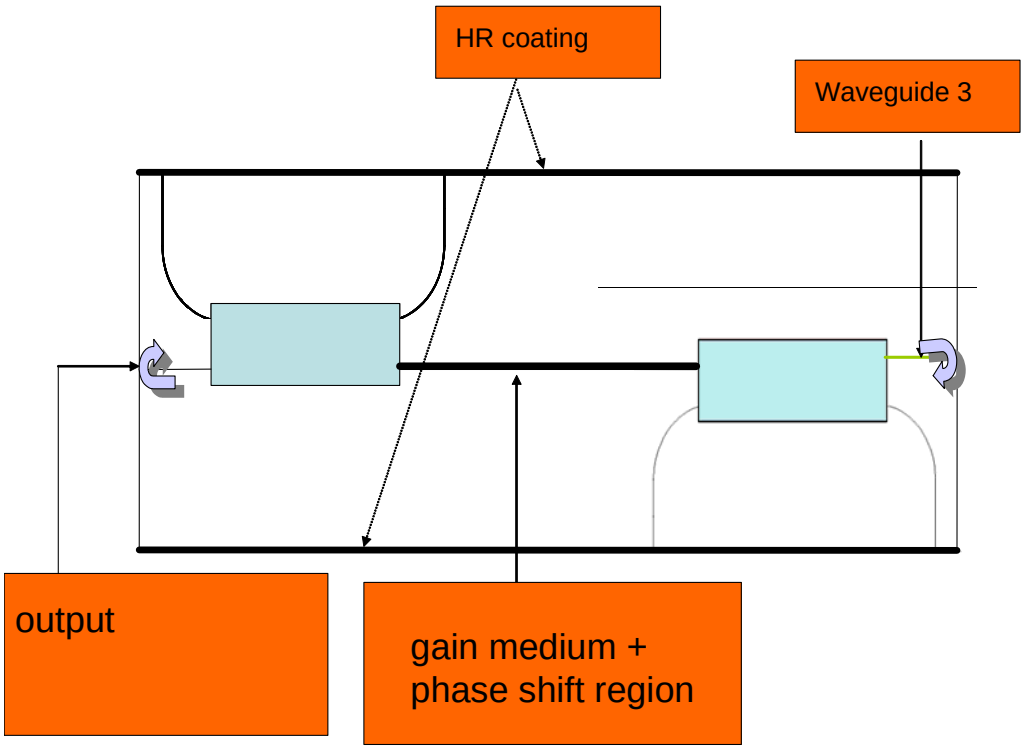

Figure 14.7: Laser embodiment where both resonators comprise SRFP resonators and are located on each side of the (gain and phase) medium. Depeneding on whether one would like to have a rear facet reflection, we can then decide whether to have the waveguide 3.

Chapter 15

Novel Laser Embodiments using Planar Fabrication and Based upon Interferometry Techniques Different from SRFP

The present chapter is directed to other novel laser embodiments based on interferometry techniques but not using SRFP. Those skilled in the art can apply the analytic framework used previously for an SRFP resonator to render a similar analysis for a first laser embodiment using a single ring resonator and a second laser embodiment using two MZIs. Both embodiments require only minimal coupling between elements, simplifying manufacturing when compared without prior laser designs.

15.1 Tunable lasers combining ring resonators

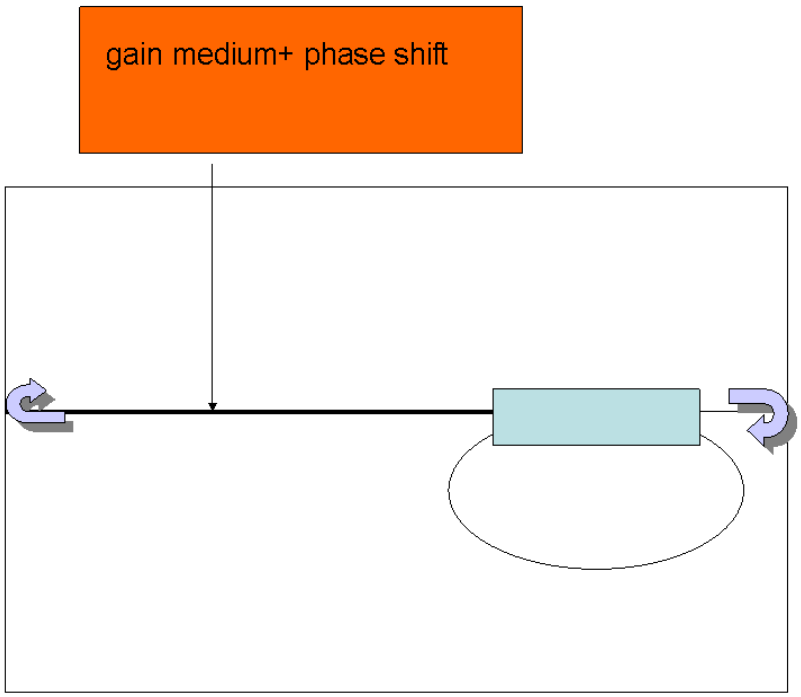

Figure 15.1: Top view of a tunable laser where the tunable frequency mirror is comprised of the combination of a ring resonator coupled to a semiconductor waveguide ended by a rear facet.

Various embodiments of the present invention employ ring resonators each having only a single coupling region with the gain medium. Other embodiments employ one or more pairs of ring resonators, each pair using a single coupling region. These lasers can be tuned through a variety methods. For example, tuning can be performed by changing the phase of the coupling coefficient between the gain medium and a ring resonator of the laser.

15.1.1 A single ring resonator

In one ring resonator laser embodiment as shown in fig. 15.1, a tunable laser comprises a semiconductor medium having a front and a rear facet and includes a lasing cavity. A gain medium is contained within the cavity of the semiconductor medium for amplifying light. A ring resonator is disposed within the semiconductor medium adjacent to the gain medium and a single coupling region for coupling the light between the gain medium and the ring resonator, the single coupling region contained within the semiconductor medium. A reflection from the ring resonator including a back reflection from the rear facet is tuned to the lasing cavity to produce lasing light from the front facet. In a further embodiment, an additional ring resonator is coupled to a 3×3 coupling region and a response from the additional ring resonator is included in the reflection to produce lasing light from the front facet, fig. 15.2. In order for the tunable frequency filter obtained with the combination of the two resonators, the 3×3 coupling region and the rear waveguide and facet, to have a high Q the coupling region should be designed such that the coupling between the two rings is high and the coupling between the waveguide and the rings low. In a further embodiment of the invention a tunable semiconductor laser uses the Vernier technique, where the two ring resonators are disposed on opposite sides of a gain medium, fig. 15.3. There are different ways of tuning the device:

- Changing the optical lengths of the rings.

- Changing the coupling coefficient of the coupling region.

- Changing the optical length of the rear waveguide

15.1.2 Laser obtained with the combination of ring resonators located on each side of the gain medium

This embodiment includes the elements of the one ring resonator laser above; however, an opposing ring resonator is disposed within the semiconductor medium adjacent to the gain medium towards an opposite end of the gain medium and an opposing single coupling region for coupling the light between the gain medium and the opposing ring resonator, the opposing single coupling region disposed within the semiconductor medium. The laser is tuned employing a Vernier technique between the ring resonator and the opposing ring resonator. In further embodiments, one or both of the ring resonator and opposing ring resonator can be a ring resonator pair coupled to the same coupling region.

15.1.3 Conclusion

All the lasers that we covered in this chapter have the advantage of readily lending themselves to planar fabrication and do not require any grating structure or moving parts. The gain medium provides light amplification and the ring resonators in combination with a back reflection from the rear facet exhibit an essentially uniform peak reflection at all resonant frequencies. The free-spectral range (FSR) is related both to the optical length of the ring resonator and the length of the waveguide between the ring and the rear facet. Each laser can be tuned by shifting the resonant frequencies of the ring resonators. Particularly, tuning of the laser can be obtained by changing the combination of the resonant frequencies resulting from the ring resonators and the back reflections from the rear facets. Alternately, this shift can be obtained, for example, by changing the optical length (circumference) of the ring resonators or by changing the phase of the coupling coefficient of the coupling region between the gain medium and the ring resonator. Tuning of some implementations

of the lasers may not be as wide as the lasers using an SRFP resonator. However, these lasers exhibit improved performance stability over other conventional designs of lasers using interferometry techniques.

15.2 A laser using two Mach-Zehnder interferometers

Another new embodiment of a tunable laser comprises two reflector elements coupled to a gain medium. A typical embodiment comprises a gain medium for amplifying light across a gain bandwidth and a semiconductor medium including a first reflector element coupled to receive light from the gain medium and comprising a first Mach-Zehnder interferometer (MZI) and a second MZI coupled in series and a second reflector element for receiving light from the first reflector element and returning the light to the first reflector element. The first MZI has a larger free-spectral range than the second MZI. The first MZI selects a wavelength region within the gain bandwidth and the second MZI selects a cavity mode within the wavelength region for producing lasing light at the cavity mode, fig. 15.4. Figs. 15.4 and 15.5 illustrate an exemplary embodiment of a tunable semiconductor laser. The tunable laser comprises a combination of a gain medium and two reflector elements. The gain medium can be implemented within a separate gain chip and coupled to the semiconductor medium of two reflector elements. The first reflector element can be described as a tunable filter element. The tunable reflector element can comprise the combination of at least two MZIs in series. The MZIs have different free-spectral ranges, i.e, as described above, one has a larger free-spectral range than the other, and operates as described above. The first MZI has a larger free-spectral range than the second MZI. In alternate embodiments, the second MZI can have

a larger free-spectral range than the first MZI. Frequency tunability of the device can be obtained by changing the difference of optical path length of the MZI with the larger free spectral range. The MZI with a large free-spectral range selects a particular wavelength region within the gain bandwidth, but this interferometer does not provide sufficient discrimination between neighboring cavity modes. The MZI with smaller free-spectral range then selects a particular cavity mode within the wavelength region selected by the MZI with larger free-spectral range. Lasing light is thus produced with the gain medium. The MZI with the smaller free-spectral range also defines the finesse of the reflector element. The second reflector element of the laser can comprise a loop that receives light from the first reflector element and returns it to the first reflector element as depicted in fig. 15.5. Alternately, the second reflector element can be a cleaved facet of the semiconductor medium as depicted in fig. 15.4. However, if the tunable element is fabricated in an amorphous medium, e.g., silicon, it can be difficult to cleave the facet at the end of the first reflector element that will perform as a high quality reflector. Accordingly, the loop used at the end of the second MZI can preferably serve as a reflector for implementations where the tunable element is fabricated in an amorphous silicon technology, fig. 15.5. This laser can be produced using simple planar fabrication technology, and does not require any grating structure or moving parts. The tunable element can be easily fabricated in a silicon technology. In contrast with other conventional designs, the laser minimizes the required coupling region in the whole structure. For example, one known design uses an MZI in series with a ring resonator that employs a coupling region between the waveguide and the ring resonator and also between the ring and the waveguide in addition to a coupling region between the gain and the passive medium. Indeed, the only coupling used in the laser is between the gain medium on the gain chip and the semiconductor (passive) medium including the tunable filter. The laser has the advantage of easy fabrication of the tunable filter only using photolithography technology for a silicon medium. In addition, the device exhibits

an improved mode suppression ratio over comparable lasers.

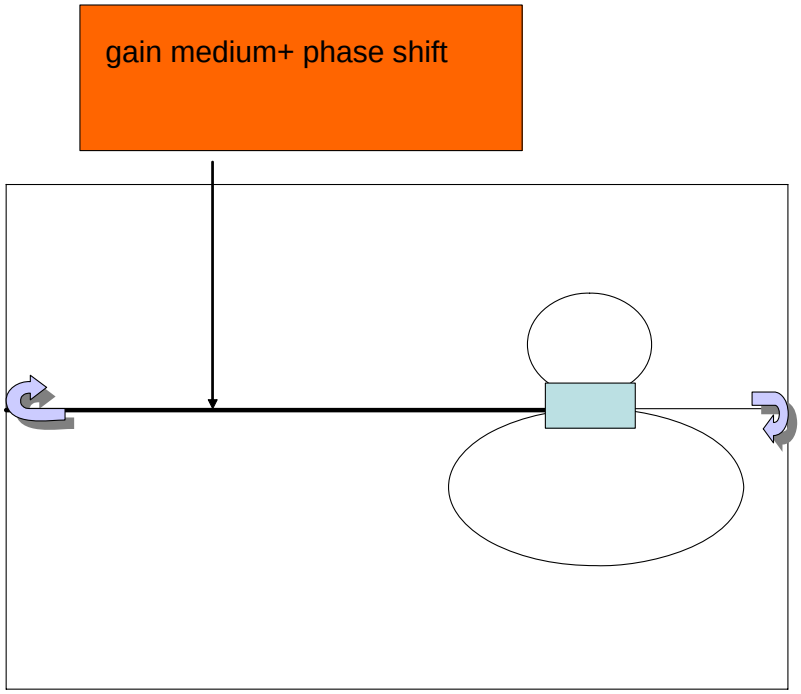

Figure 15.2: Top view of a tunable laser where the tunable frequency mirror is composed of two ring resonators coupled with the help of a 3 x 3 coupler to the same semiconductor waveguide ended by a rear facet reflection. A special design of the 3 x 3 coupler requires a high coupling efficiency between the ring resonators themselves and a low coupling coefficient between the ring resonator and the waveguide.

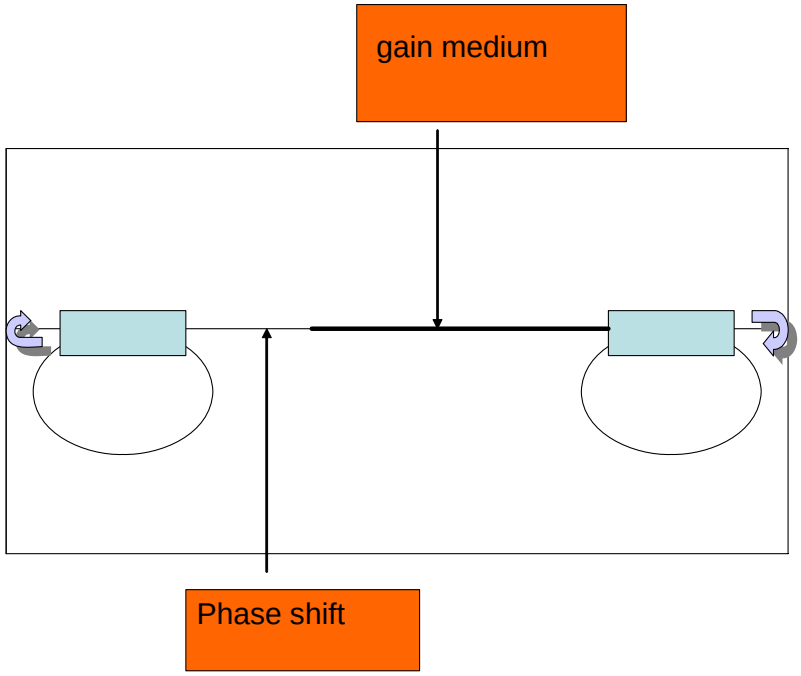

Figure 15.3: Laser embodiment based upon the Vernier technique and using a ring resonator as the tunable frequency mirrors diposed within the semiconductor medium adjacent to the ends of the gain medium.

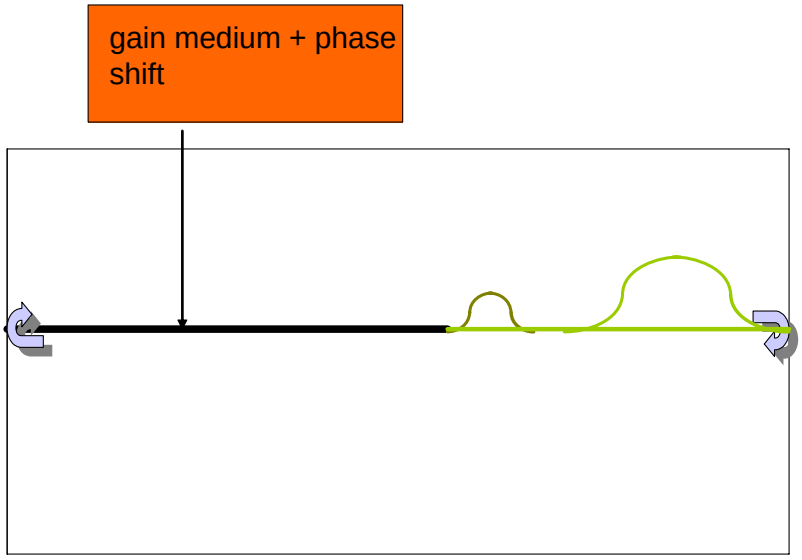

Figure 15.4: Top view of a tunable laser obtained by the combination of two MZIs.

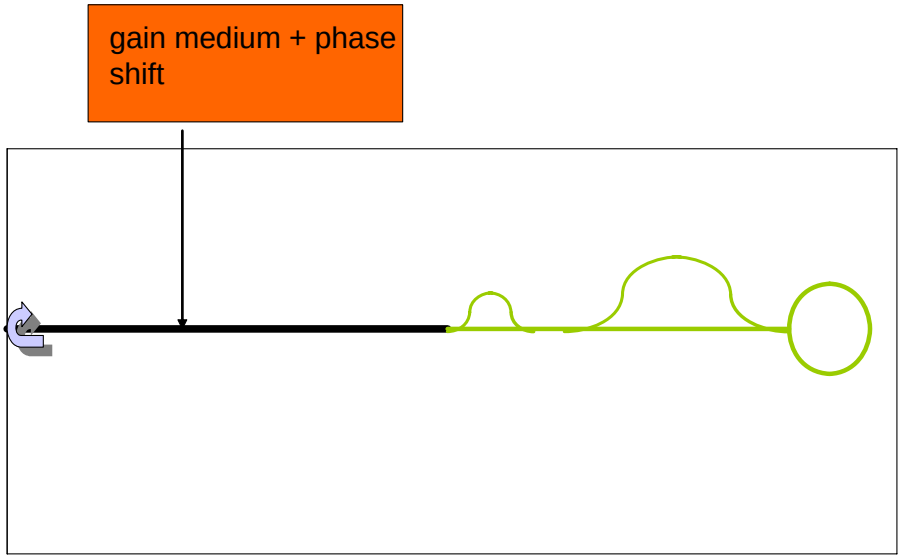

Figure 15.5: Top view of a tunable laser obtained by the combination of two MZIs and terminated with a loop instead of a cleaved facet.

Chapter 16

General Novel Laser Embodiments

In the previous sections and chapters we studied a few embodiments of tunable lasers. However, there are many other novel embodiments that could be of interest in future applications. Fig. 16.1 gives a generic picture of these lasers, where the dashed box could represent different combinations of resonator (that does not mean that all of them should absolutely represent a resonator); for example, in one case these resonators could be chosen from those represented in fig. 12.11.

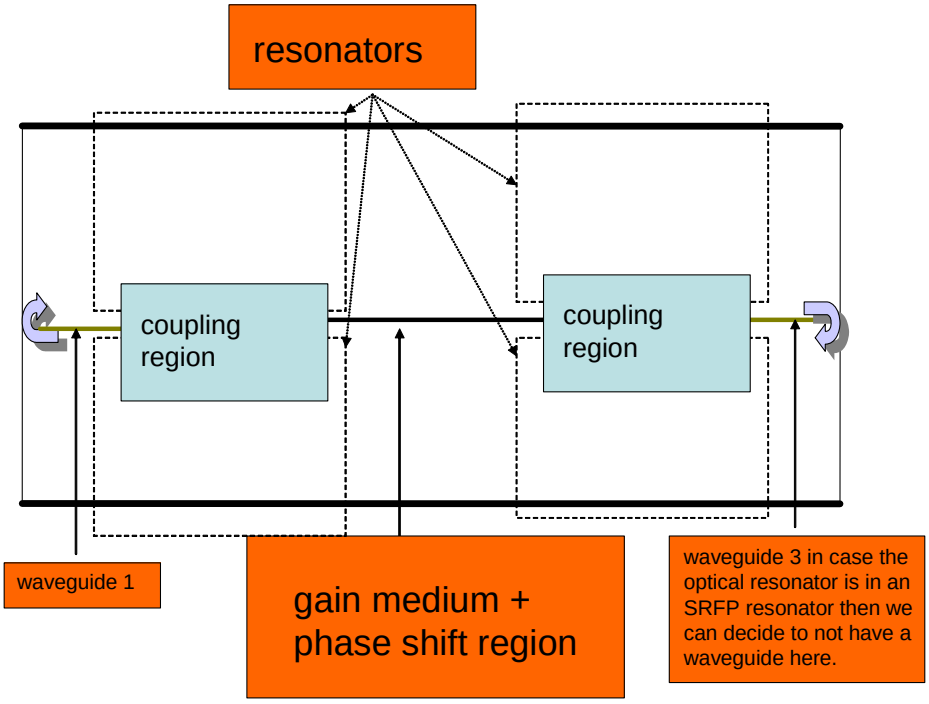

Figure 16.1: Illustrates a generic embodiment of lasers, which could be tuned in frequency also.

Chapter 17

Other Designs of the SRFP Resonator

Chapter 18

Semidisk Fabry-Perot Resonator (SDFP) and Semisphere Fabry-Perot Resonator (SSFP)

18.1 Semi Disk Fabry-Perot resonator (SDFP)

As studied earlier, one of the key SRFP resonator parameters is the length of the resonator, which is inversely proportional to the free spectral range of the device. For many applications it is of great interest to have a resonator with high free-spectral range. That means fabricating devices as much as smaller possible. But the limiting factor is the field radiation due to the bending of the waveguide. Indeed, as we have seen previously, due to its shape for the same free-spectral range, the required length of the SRFP is half that of the ring resonator. Therefore, the maximum FSR that an SRFP resonator exhibits is higher than that of a ring resonator. In the case of a ring resonator, in order to overcome this limit a disk resonator has been introduced. The modes of the disk resonator are the whispering gallery modes. The same reasoning

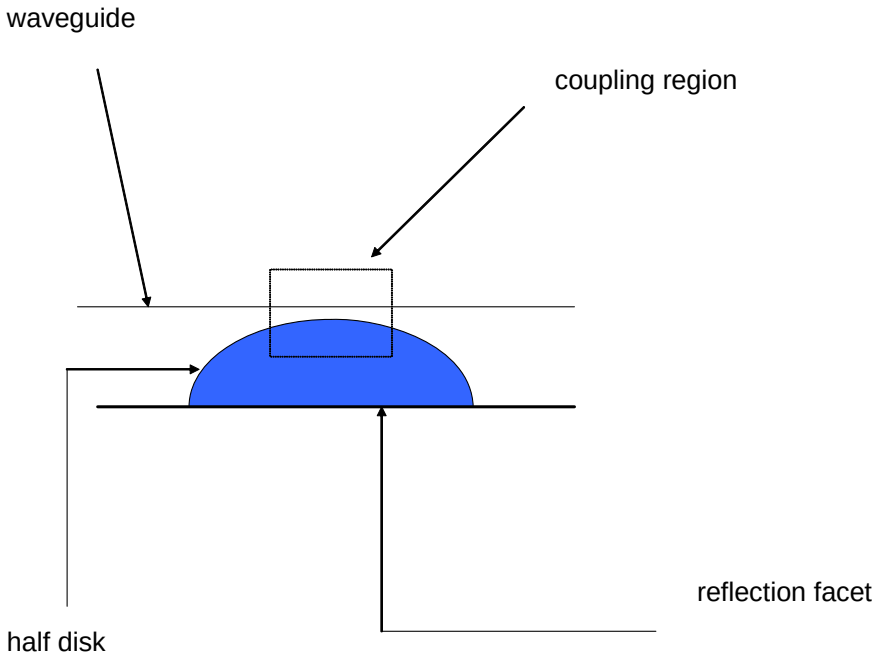

Figure 18.1: An Semidisk Fabry-Perot resonator.

could be made with the SRFP resonator. In order to be able to fabricate very small devices exhibiting high FSR without being limited by the bending loss, we could use a disk instead of a ring in the initial SRFP structure, fig. 18.1.

18.2 Semisphere Fabry-Perot resonator

In the past in order to increase further the quality factor of a disk resonator, a three-dimensional disk resonator, which is a sphere resonator, has been introduced. Similarly we introduce the semisphere Fabry-Perot (SSFP) where the ring resonator

in the case where an SRFP resonator is replaced by a sphere.

Chapter 19

An Electronic Version of the SRFP Resonator

The same way that we have described an SRFP resonator in optics, we can define a similar device in electronic, which is illustrated in fig. (19.2). The feed-back is now obtained by the reflection r_{hr}, which is created by electronic blocs. An example of similar analogy between electronic and optic is the electronic version of the ring resonator, which combined with others electronic components is illustrated in fig. (19.1).

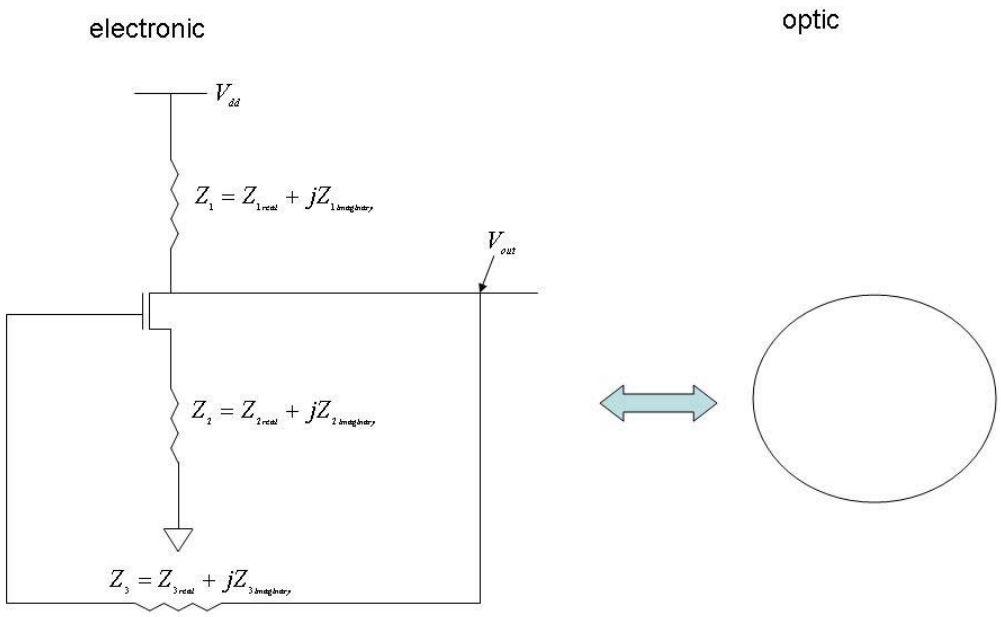

Figure 19.1: Emphasizes the analogy between an electronic oscillator and an optical ring resonator.

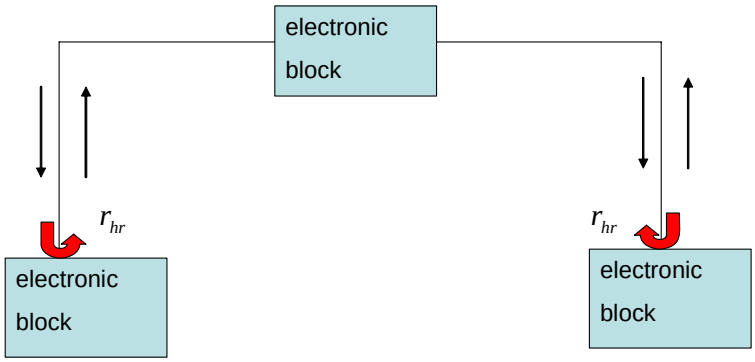

Figure 19.2: Block diagram of an electronic version of the SRFP.

Chapter 20

Novel Tiltmeter

We are presenting here the concept of using the quality factor of a resonator in order to monitor angle shift in an incident signal based on a transmission. The Q factor or quality factor is a measure of the "quality" of a resonant system. Resonant systems respond to (frequencies, angles of incidence, etc.) close to their natural (frequency, angle of incidence, etc.) much more strongly than they respond to other (frequencies, angles of incidence, etc.). The Q factor indicates the amount of resistance to resonance in a system. Systems with a high Q factor resonate with greater amplitude (at the resonant frequency) than systems with a low Q factor. Damping decreases the Q factor. Resonators have therefore been used to measure and monitor any change in frequency, since a change in frequency would decrease the Q factor of the system. In addition to monitoring a change in frequency, it is desirable in some circumstances to monitor the angle of incidence. However, nothing heretofore devised has used a resonator to monitor this angle. Thus, a continuing need exists for a system that allows a user to monitor the angle of incidence based on a transmission through a resonator. Within some regions of application, the quality factor is much more sensitive to angle shift than it is to frequency shift. Using its quality factor, we propose

for the first time to use the resonator to measure any angle shift from the optimum angle of incidence. The resonator is any suitable mechanism or device that allows for the resonant oscillation of an input signal, a non-limiting example of which includes a Fabry-Perot etalon. Other non-limiting examples include a hollow chamber whose dimensions allow the resonant oscillation of electromagnetic or acoustic waves, and an electrical circuit that combines capacitance and inductance in such a way that a periodic electric oscillation will reach maximum amplitude. Using the resonator, an incident signal is introduced to the resonator. The measured angle is the incident angle of the signal entering the resonator. Each time this angle shifts, it changes the transmitted intensity and reflected intensity. The degree to which the incident angle has been changed can be deduced by measuring either the transmitted intensity or the reflected intensity. One example of such embodiment is the one illustrated in fig. (20.2). However, the novel concept that we introduce here is not just restricted to that structure but can be expanded to the use of a wide variety of resonators.

20.1 A novel angle tiltmeter based on the use of a Fabry-Perot resonator

For many years the Fabry-Perot etalon has been used as an efficient tool to monitor wavelength changes of the input light. In addition, we introduce here the concept of using the Fabry-Perot etalon as a tool to monitor the incident angle change of the input light. We will derive a boundary condition determining when the transmission of an incident light through a Fabry-Perot etalon is either more sensitive to the wavelength change of the incident light or to its incident angle change. That allows us to conclude when the Fabry-Perot etalon can be used as a tool to monitor the wavelength change of the incident light and when it can monitor its angle change.

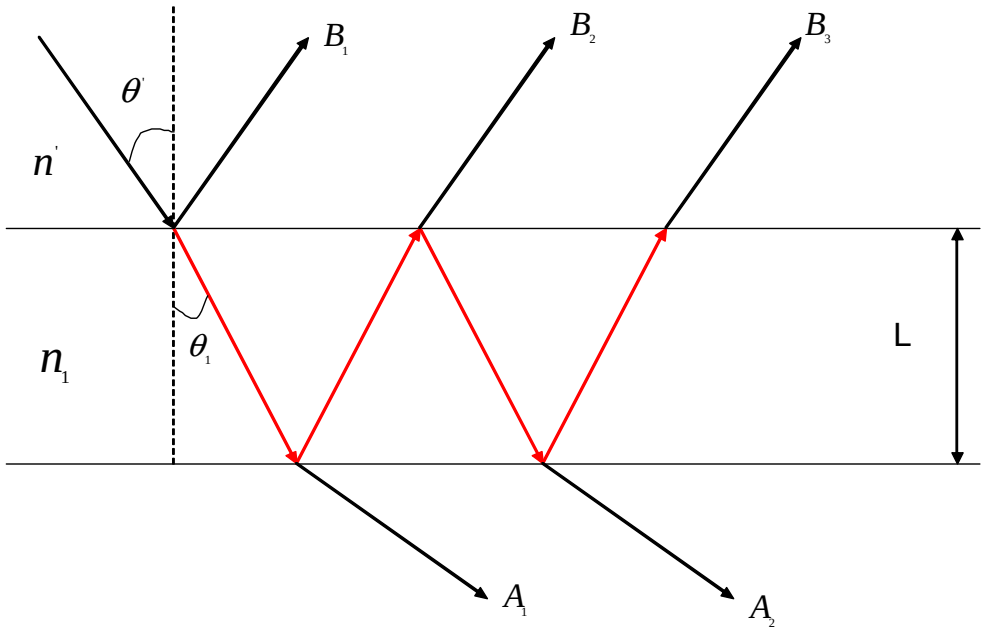

Figure 20.1: Multiple reflections model for analyzing the Fabry-Perot etalon.

A Fabry-Perot interferometer consisting of a plane-parallel plate of thickness l and index n is immersed in a medium of index $n\prime$, [1]. Let a plane wave be incident on the etalon at an angle θ to the normal, as shown in fig. 20.1. The problem of the transmission (and reflection) of the plane wave through the etalon can be treated by considering the infinite number of partial waves produced by reflections at the two end surfaces. The phase delay between two partial waves, which is attributable to one additional round trip, is given by

$$\partial = \frac{-4\pi nl\cos(\theta)}{\lambda},$$

where λ is the vacuum wavelength of the incident wave and θ is the internal angle of incidence. If the complex amplitude of the incident wave is taken as A_i, then the partial reflections, B_1, B_2, and so forth, are given by:

$$B_1 = rA_i,$$

$$\begin{aligned} B_2 &= tt^{'}r^{'}A_i e^{j\partial}, \\ B_3 &= tt^{'}r^{'3}A_i e^{2j\partial}, \end{aligned}$$

where r is the reflection coefficient (ratio of reflected to incident amplitude), t is the transmission coefficient for waves incident from n' toward n, and $r\prime$ and $t\prime$ are the corresponding quantities for waves incident from $n\prime$ toward n, and $r\prime$ and $t\prime$ are the corresponding quantities for waves traveling from n toward $n\prime$. The complex amplitude of the total reflected wave is

$$\begin{aligned} A_r &= B_1 + B_2 + B_3 + ... \\ A_r &= \left\{ r + tt^{'}r^{'}e^{j\delta}\left(1 + r^{'2}e^{j\delta} + ..\right)\right\} A_i \end{aligned}$$

For the transmitted wave,

$$\begin{aligned} A &= tt^{'}A_i, \\ A_2 &= tt^{'}r^{'2}A_i, \\ A_3 &= tt^{'}r^{'4}e^{2j\delta}A_i. \end{aligned}$$

Adding up the A terms, we obtain

$$A_t = A_i tt' \left(1 + r'^2 e^{j\delta} + r'^4 e^{2j\delta} + ..\right)$$

for the complex amplitude of the total transmitted wave. λ is the vacuum wavelength of the incident wave and θ is the internal angle of incidence. It can be shown that the Fabry-Perot etalon has an intensity transmission that is

$$T_{transmission} = \frac{(1-R)^2}{(1-R)^2 + 4r\sin\left(\frac{\delta}{2}\right)^2}. \tag{20.1}$$

Assuming that the geometry and material properties remain constant, equation (20.1) shows that the transmission is a function of the wavelength of the input signal, where R is the fraction of the intensity reflected. For many years the transmission intensity dependence on the wavelength of the input field has been used to monitor any wavelength change for the input field. Here we propose the same technique to monitor any angle change of the input field, fig. 20.2. From equation (20.1), it is clear that the transmission intensity is also angle dependent. That can be done since the intensity transmission is also angle dependent.

$$T_{ransmission} = \frac{(1-R)^2}{(1-R)^2 + 4r\sin\left(\frac{-2\pi nl\cos(\theta)}{\lambda}\right)^2}. \tag{20.2}$$

Taking the derivative of equation (20.2),

$$\frac{\partial T}{\partial \theta} = \frac{\delta\left(1-R\right)^2 R\sin\left(\frac{\delta}{2}\right)\frac{\partial R}{\partial\theta} - 4\left(1-R\right)^2\sin\left(\frac{\delta}{2}\right)\frac{\partial R}{\partial\theta} + 4R\left(1-R\right)^2\cos\left(\frac{\delta}{2}\right)\frac{\partial\delta}{\partial\theta}}{(1-R)^2 + 4R\sin\left(\frac{-2\pi nl\cos(\theta)}{\lambda}\right)}.$$

If the reflection R is angle independent meaning $\frac{\partial R}{\partial \theta} = 0$ within the working range, then

$$\frac{\partial T}{\partial \theta} = -T.\frac{4R\cos\left(\frac{\delta}{2}\right)\frac{\partial \delta}{\partial \theta}}{(1-R)^2 + 4R\sin\left(\frac{\delta}{2}\right)^2},$$

with

$$\frac{\partial \delta}{\partial \theta} = -\frac{4\pi nl\sin(\theta)}{\lambda},$$

and besides,

$$\frac{\partial T}{\partial \lambda} = -T.\frac{4R\cos\left(\frac{\delta}{2}\right)\frac{\partial \delta}{\partial \theta}}{(1-R)^2 + 4R\sin\left(\frac{\delta}{2}\right)^2}\frac{4\pi nl\cos(\theta)}{\lambda^2},$$

therefore,

$$\frac{\frac{\partial T}{\partial \theta}}{\frac{\partial T}{\partial \lambda}} = \tan(\theta)\,\lambda. \tag{20.3}$$

The variation of the light intensity transmission through the Fabry-Perot resonator dT has two components. One is the contribution $\frac{dT}{d\theta}$ of an angle change $d\theta$, the other is the contribution $\frac{dT}{d\lambda}$ of the wavelength change $d\lambda$. Therefore, we can express dT as

$$dT = \frac{\partial T}{\partial \theta}d\theta + \frac{\partial T}{\partial \lambda}d\lambda.$$

In the case that we would like to have a system that is rather more angle sensitive than wavelength sensitive, we shall have

$$\left|\frac{\partial T}{\partial \theta} d\theta\right| > \left|\frac{\partial T}{\partial \lambda} d\lambda\right|, \tag{20.4}$$

and in the case we would like to monitor the wavelength,

$$\left|\frac{\partial T}{\partial \theta} d\theta\right| < \left|\frac{\partial T}{\partial \lambda} d\lambda\right|, \tag{20.5}$$

using equation (20.3) and under the assumption of small angle change

$$d\theta \sim \theta,$$

$$\frac{\partial T}{\partial \theta} = \tan(\theta)\, \lambda \frac{\partial T}{\partial \lambda} \sim \theta \lambda \frac{\partial T}{\partial \lambda}.$$

So,

$$\left|\frac{\partial T}{\partial \theta} d\theta\right| > \left|\frac{\partial T}{\partial \lambda} d\lambda\right| => \left|\theta^2 \lambda \frac{\partial T}{\partial \lambda}\right| > \left|\frac{\partial T}{\partial \lambda} d\lambda\right|.$$

Therefore, in satisfying

$$\theta > \sqrt{\frac{d\lambda}{\lambda}}, \tag{20.6}$$

we will satisfy equation (20.4), and in satisfying

$$\theta < \sqrt{\frac{d\lambda}{\lambda}},$$

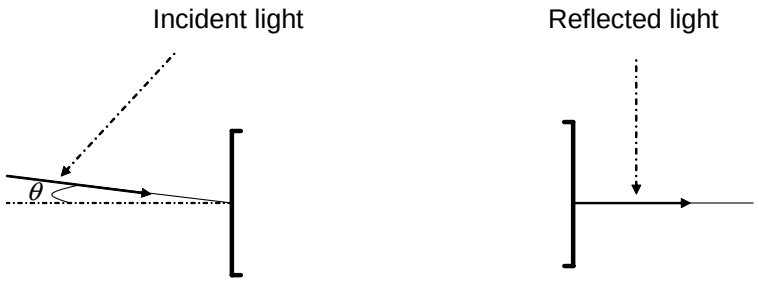

Figure 20.2: Illustration of tiltmeter setup based upon the use of a Fabry-Perot resonator.

we will satisfy equation (20.5). From [93], we can monitor wavelength change up $d\lambda = 10^{-12}$ m for a central wavelength of $\lambda = 1.55$ μm. So from equation (20.6), with the current technology we are able to detect angle change θ as small as a few millidegrees.

Chapter 21

Conclusions

We have seen that resonators, which are devices that create or sustain periodic or cyclic events (which can be a wave or a material), are the most fundamental and basic devices in science and engineering. Some examples of resonators are a guitar, lasers, oscillators, vibration of atoms, etc.

Over all resonators can be organized into two fundamental categories:

1. Using reflectors that reflect back the event, we force the event to come to its initial state. Examples of such resonators are:

   - Whenever we talk within a chamber that echoes our voice, we can call this resonator the archetype mechanical resonator.
   - The Fabry-Perot resonator, which is nothing more than the optical version of the archetype mechanical resonator cited before.

2. We shape the path of the event in such a way that it will come to its initial state without the help of any sort of reflector. Examples of such resonators are:

- Ring (sphere) resonator.
- Cyclotron.
- Any close shape resonator.

We have introduced, designed, and fabricated in this thesis a novel resonator that we call an SRFP resonator. The SRFP resonator combines in one resonator the advantages of the two types of resonator and has additional unique features. Within this thesis we have focused upon an optical application of an SRFP resonator. However, the SRFP could be used in any engineering field.

The advantages of an SRFP resonator over a typical optical version of the first category of resonator, which is called the Fabry-Perot, are:

- The reflection field has a greater finesse.
- It can be integrated on a chip more easily.
- Its length is not correlated with that of the chip, in contrast with a Fabry-Perot. The last means that in an Integrated Optical Device, the periodicity of the spectrum responses of SRFP resonators are not correlated. However in the case of a Fabry-Perot they are.
- The SRFP resonator is not interrupting the main waveguide.
- It is easier to fabricate a symmetrical SRFP since its two arms end in the same facet.

There are several advantages of an SRFP resonator over a ring resonator:

- The SRFP supports waves propagating in both directions (standing waves). This allows the resonator to transmit and reflect at the same time. However,

in the case of a waveguide coupled to a ring resonator there is no standing wave and therefore no reflected light.

- The SRFP exhibits a loss due to the bending of the waveguide that is less than half of that exhibited by a ring resonator. If we expect that similar to a ring resonator this loss determines how small the device could be fabricated, then an SRFP should be smaller than an equivalent ring resonator.

- The transmission extinction ratio of the SRFP is higher than a ring resonator.

We have also seen that one of the very interesting features of the SRFP resonator is to be able to generate very easily transmitted and reflected light that are in quadrature of phase. This interesting relation between the reflected and transmitted light is true for any symmetrical device. However, as has been shown here, it is much easier to fabricate a relatively high as accurate symmetrical SRFP resonator than a symmetrical Fabry-Perot resonator, as the latter requires both mirrors of the Fabry-Perot to be identical. In order to make optimal use of the phase relation between the reflected and the transmitted fields, neither the reflected not transmitted light can be negligible. This requires the resonator to have low finesse because in the case of high finesse a small variation in frequency will imply a major increase of the intensity of the reflected (transmitted) over the transmitted (reflected) light. The major advantage of the SRFP is that its finesse can be tuned by adjusting the coupling coefficient. By doing so we do not at all change the symmetry of the device. In case of the Fabry-Perot, tuning the finesse of the device without at the same time changing the symmetry of the device would mean simultaneously changing the reflection of both mirrors.

An emerging research field of interest is the reduction of the propagating speed of light within an optical structure. Most of the current schemes are based upon the propagation of light through ring resonators. However, if one compares a ring

and an SRFP resonator with the same length and coupling coefficients, the SRFP exhibits a delay time of twice that of the ring resonator. Besides, in addition to having a transmitted light it also has a reflected light that could be used in these sorts of schemes. So, not only does the SRFP exhibit a longer delay line than the ring and Fabry-Perot resonators, and therefore if used correctly it could increase the performance of current state of the art technologies, it also has a reflected light. If the SRFP is designed correctly then in addition to exhibiting higher performance than current technology it could also provide for easier fabrication and more compact devices. In order to cancel the effect of the bending loss and therefore to fabricate a ring resonator with even smaller features and higher FSR, the disk resonator has been introduced. Similarly, we have introduced the Semi Disk Fabry-Perot resonator (SDFP). In the case of the SDFP, a disk resonator is replacing the ring resonator used in an SRFP. In the past, in order to increase further the quality factor of a disk resonator, a three-dimensional disk resonator, which is a sphere resonator, has been introduced. Similarly, we have introduced the Semi Sphere Fabry-Perot (SSFP), where the ring resonator in the case of an SRFP resonator is replaced by a sphere. We also have introduced different novel tunable laser embodiments using SRFP resonators. One of the interesting features of the SRFP resonator is its ability to have a high finesse and a periodic and uniform reflection spectrum. That can be used in tunable laser applications that would generate multi modes with high mode suppression ratios. We also have introduced novel tunable laser embodiments based on planar fabrication. We indeed believe that besides exhibiting an ease of fabrication, planar fabrication will be of much interest in the future because it does not constrain the fabrication of the device on a limited number of materials for which the frequency range of operation is dictated by their energy bandgap.

We also presented at the end of the thesis, a novel way of measuring the tilt of a field.

References

[1] A. Yariv, *Optical Electronics in Modern Communications*, Oxford University Press, 5th edition, 1997.

[2] R. J. Lang, A. Yariv, J. Salzman, "Laterally Coupled-Cavity Semiconductor Laers," *IEEE Journal of Quantum Electronics*, Vol. QE-23, No. 4, April 1987.

[3] J. Salzman, R. Lang, and A. Yariv, "Frequency selectivity in laterally coupled semiconductor laser arrays", *Optics Letters*, Vol.10, No. 8, August 1997.

[4] A. Othonos, K. Kalli, *Fiber Bragg Gratings*: *Fundamentals and Applications in Telecommunications and Sensing*, Artech House Optoelectronics Library, 1999.

[5] M-C. Amann, J. Buus, *Tunable Laser Diodes*, Artech House Publishers, 1998.

[6] K. Aiki, M. Nakamura, J. Umeda, A. Yariv, A. Katzir, and H. W. Yen, "GaAs-GaAlAs distributed feedback laser with separate optical and carrier confinmenet," *Applied Physics Letters*, Vol. 27, No. 3, 1975.

[7] H. Kressel and J. K. Butler, *Semiconductor Lasers and Heterojunction LEDS*, New York: Academic Press, 1977.

[8] J. Singh, *Electronic and Optoelectronic* Pr*operties of Semiconductor Structures*, Cambridge University Press, 2003.

[9] D. A. Neamen, *Semiconductor Physics and Devices*: *Basic Principles*, 3rd edition, McGraw Hill Professional, 2003.

[10] H. Nelson, "Epitaxial Growth from the Liquid State and its Application to the Fabrication of Tunnel and Laser Diodes," *RCA Review*, 24, 603, 1963.

[11] National Materials Advisory Board Commission on Engineering and Technical Systems National Research Council, *Materials for High − Temperature Semiconductor Devices*, National Academy Press, 1995.

[12] G. H. B. Thompson, *Physics of Semiconductor Laser Devices*, Wiley, 1980.

[13] H. C. Casey, Jr. and M. B. Pamish, *Heterostructure Lasers*, *Part A : Fundamental Principles*, Academic Press, 1978.

[14] H. C. Casey, Jr. and M. B. Pamish, *Heterostructure Lasers*, *Part B : Materials and operating charactersitics*, Academic Press, 1978.

[15] G. P. Agrawal, and N. K Dutta, *Long − Wavelength Semiconductor Lasers*, Van Nostrand Reinhold, 1986.

[16] G. Morthier, and P. Vankwikelberge, *Handbook of distributed feedback laser diodes*, Artech House, 1997.

[17] C. Kittel, *Introduction to Solid State Physics*, Wiley, 7th edition, 1996.

[18] J. M. Ziman, *Principles of the Theory of Solids*, Cambridge University Press, 2nd edition, 1972.

[19] N. F. Mott and H. Jones, *Theory of the Properties of Metals and Alloys*, Oxford University Press, 1936.

[20] K. Seeger, *Semiconductor Physics*: *An Introduction*, Springer, 4th edition, 1989.

[21] R. Dalven, *Introduction to Applied Solid State Physics*, Plenum, 2nd edition, 1990.

[22] R. A. Smith, *Semiconductors*, Cambridge University Press, 2nd edition, 1978.

[23] S. M. Sze, *Semiconductor Devices*, *Physics*, *and Technology*, Wiley, 1985.

[24] M. L. Cohen and J. R. Chelikowsky, *Electronic Structure and Optical Properties of Semiconductors*, Springer, 2nd edition, 1989.

[25] W. Beenakker and H. van Houten, "Quantum transport in semiconductor nanostructures," *Solid State Physics*, Vol. 44, No. 1, 1991.

[26] G. Bastard et al., "Electronic states in semiconductor heterostructures," *Solid State Physics*, Vol. 44, No. 10, 1994.

[27] S. Taghavi Larigani, J. VanZyl, A. Yariv, "Optical Resonator and Laser Applications," United States Patent Publication Serial No. US20040032888.

[28] S. Taghavi Larigani, J. VanZyl, A. Yariv, "Tunable Semiconductor Lasers," United States Patent Publication Serial No US20040032886.

[29] S. Taghavi Larigani "Tunable Semiconductor Laser based on the combination of an Mach-Zehnder Interferometer with a Fabry-Perot or a Ring resonator cavity, using only one coupling region and exhibiting a high mode suppression ratio," United States Provisional Application Serial No. 60/392,517, filed June 28, 2002.

[30] S. Taghavi Larigani "Novel Wide Tunable Semiconductor Lasers based on the combination of a Mach-Zehnder inside a ring resonator cavity, using only one coupling region and exhibiting high supression mode ratio," United States Provisional Application Serial No. 60/398,428, filed July 24, 2002.

[31] S. Taghavi Larigani "Novel Wide Tunable Semiconductor Lasers based on the combination of a Mach-Zehnder inside a Fabry-Perot cavity resonator, using only one coupling region and exhibiting high mode supression ratio," United States Provisional Application Serial No. 60/398,429, filed July 24, 2002.

[32] S. Taghavi Larigani "Novel Wide Tunable Semiconductor Lasers based on the combination of a ring resonator cavity inside a Fabry-Perot cavity," United States Provisional Application Serial No. 60/398,430, filed July 24, 2002.

[33] S. Taghavi Larigani "Novel wide tunable semiconductor laser based on the combination of a Mach-Zehnder Interferometer inside a Fabry-Perot resonator," United States Provisional Application Serial No. 60/402,432, filed August 9, 2002.

[34] S. Taghavi Larigani, "Novel Tunable Semiconductor Lasers based on the combination of two resonators," United States Provisional Application Serial No. 60/406,428, filed August 28, 2002.

[35] S. Taghavi Larigani, "Double Semi-Ring Fabry-Perot Coupled Laser DSRFP-CL," United States Provisional Application Serial No. 60/424, 736, filed November 8, 2002.

[36] Shervin Taghavi Larigani "Novel Tunable Semiconductor Lasers based on the combination of two resonators," United States Provisional Application Serial No. 60/428,348, filed November 22, 2002.

[37] S. Taghavi Larigani "Novel TunableSemiconductors using ring resonator and back reflection,".S. Provisional Application Serial No. 60/435,110, filed Dec. 19, 2002.

[38] S. Taghavi Larigani, "Optical Resonator and Laser Applications," U.S. Application Serial No. 10/610,292, filed Jun. 30, 2003.

[39] A.Yariv, "Universal relations for coupling of optical power between microsenators and dielectric waveguides," *Electronics Letters*, Vol. 14, No. 4, 2000.

[40] L. A. Coldren and S. W. Corzine, *Diode Lasers and Photonic Integrated Circuits*, Wiley-Interscience Publications, 1995.

[41] L. Pavesi and D. Lockwood, *Silicon Photonics*, Springer-verlag, 2004.

[42] G. Reed and A. Knights, *Silicon Photonics*: *An Introduction*, John Wiley, 2004.

[43] M. O. Manasreh, *InP and Related Compounds Materials*, *Applications and Devices*, Gordon & Breach, 2000.

[44] J. Bhardwaj, H. Ashraf, A. McQuarrie, "Dry Silicon Etching for Mems," *Symposium on Microstructures and Microfabricated Systems*, Annual Meeting of the Electrochemical Society, 1997.

[45] S. M. Sze, *VLSI Technology*, McGraw-Hill, 1983.

[46] C. Linder, T. Tschan and N. F. de Rooji, "Deep dry etching techniques as new Ic compatible tool for silicon micromachining," *International Conference on Solid-State Sensors and Actuators*, *Digest of Technical Papers*, 1991.

[47] Richard A. Gottscho, Gerald Smolinsky, and Randolph H. Burton "Carbon tetrachloride plasma etching of GaAs and InP: a kinetic study utilizing nonperturbative optical techniques," *Journal of Applied Physics*, Vol. 53, No. 8, 1982.

[48] L. A. Coldren, K. Iga, B. I. Miller and J. A. Rentschler, "GaInAsP/InP stripegeometry laser with a reactive-ion-etched facet," *Applied Physics Letters*, Vol. 37, No. 8, 1980.

[49] L. A. Coldren, B. I. Miller, K. Iga, and J. A. Rentschler, "Monolithic two-section GaInAsP/InP active-optical-resonator devices formed by reactive ion etching," *Applied Physics Letters*, Vol. 38, No. 5, 1981.

[50] R. H. Burton, H. Temkin, and V.G. Keramidas, "Plasma Separation of InGaAsP/Inp Light-Emitting Diodes," *Applied Physics Letters*, Vol. 37, No. 4, 1980.

[51] R. E. Klinger and J. E. Greene "Reactive etching of GaAs in $CCl_{4-x}F_x$ (x=0,2,4) and mixed $CCl_{4-x}F_x$/Ar discharges," *Journal of Applied Physics*, Vol. 54, No. 3, 1983.

[52] R.H. Burton and G. Smolinsky, "CCl_4 and Cl_2 plama etching of III-V semiconductors and the role of added O_2," *Journal of Electrochemistry Society*, 129, 1599 1982.

[53] R. A. Barker, T. M. Mayer, and Randolph H. Burton "Surface composition and etching of III-V semiconductor in Cl_2 ion beams," *Applied Physics Letters*, Vol. 40, No. 7, 1982.

[54] V. Montgomery, R. H. Williams, and R.R Varma, "The interaction of chlorine with indium phosphide surfaces," *Journal of Physics C*: *Solid State Physics*, Vo. 11, 1989. 1978.

[55] T.R. Hayes, M.A. Dreisbach, P.M. Thomas, W.C. Dautremont-Smith, and L.A. Heimbrook, "Reactive Ion etching of InP in HI-based discharges," *Applied Physics Letters*,Vol. 60, No. 7, 1992.

[56] V. M. Donnelly, D. L. Flamm, C. W. Tu, and D. E. Ibotson, "Temperature dependence of indium phosphide and gallium arsenide etching in a chlorine plasma," *Journal of the Electrochemical Society*, Vol. 129 , No. 11, 1982.

[57] S. C. McNevin, "Chemical etching of GaAs and InP by chlorine: The thermodynamically predicted dependence on Cl_2 pressure and temperature," *Journal of Vaccum Science & Technology*.Vol. B4, 1986.

[58] D. A. Roberts, M. A. Pate, and P. A. Claxton "Electrical and structural changes in the near surface of reactivity ion etched InP," *Electron Letters*, Vol. 24, 1988.

[59] D. Lecrosnier, L. Henry, A. Le Corre, and Vaudry, *Electronics Letters*,Vol. 23, 1987.

[60] T.R. Hayes, *Indium Phosphide and Related Materials : Processing, Technology and Devices*, edited by A. Katz (Artech House), 1992.

[61] S.J. Pearton, U.K. Chakrabarti, A.Katz, F.Ren, and T.R.Fullowan, "High-rate, anisotropic dry etching of InP in HI-based discharges," *Applied Physics Letters*, Vol. 60, No. 7, 1992.

[62] S. J. Pearton, U. K. Chakrabarti, A. Katz, A. P. Perley, W.S. Hobson, and C. Constantine, "Development of an offline x-ray photoelectron spectroscopic personal computer-based data analysis system," *Journal of Vacuum Science & Technology A*, Vol. 9, No. 3, 1991.

[63] U.Niggebrugge, M. Klug, and G. Garus, "Gallium arsenide related compounds," *Institute of Physics Conference Series*, 1985.

[64] W. M. J. Green, R. K. Lee, G. A. DeRose, A. Scherer, and A. Yariv, "Hybrid InGaAsP-InP Mach-Zehnder racetrack resonator for thermooptic switching coupling control," *Optics Express*,Vo. 13, No. 5, 2005.

[65] K. Kasaya, O. Mitomi, M. Naganuma, Y. Kondo, and Y. Noguchi, "A Simple Laterally Tapered Waveguide for Low-Loss Coupling to Single-Mode Fibers," *IEEE Photonics Technology Letters*, Vol. 5, No 3, March 1993.

[66] Y. Shani, C. H. Henry, R. C. Kistler, R. F. Kazarinov and K J. Orlowsky, "Integrated Optic Adiabatic Devices on Silicon," *IEEE Journal of quantum Electronics*, Vol. 27, No. 3, March 1991.

[67] A. Yariv, *Optical Electronics in Modern Communications*, Oxford University Press, 5th edition, 1997.

[68] P. E. Barclay, K. Srinivason and O. Painter, "Design of photonic crystal waveguides for evanescent coupling to optical fiber tapers and integration with high Q cavities," *Journal of the Optical .Society of America : B* , Vol. 20, No.11, 2003.

[69] K. Kawano and T. Kitoh, *Introduction to Optical Waveguide Analysis : Solving Maxwell's Equation and the Schrodinger Equation*, Wiley-Interscience Publications, 2001.

[70] V. Swaminathan, *Indium Phsophide and Related Materials: Processing, Technology, and Devices*, A.Katz, Ed. Artech, 1991.

[71] D.V. Tishinin, P. D. Dapkus, A. E. Bond, I. Kim, C. K. Lin and J. O'Brien, "Vertical resonant couplers with precise coupling efficiency control fabricated by wafer bonding," *IEEE Photonics Technology Letters*, Vol. 11, No. 8, 1999.

[72] B.E. Little, S. T. Chu, W. Pan, D. Ripin, T. Kaneko, Y. Kokubun and E. Ippen, "Vertically coupled galss microring resonator channel dropping filters," *IEEE Photonics Technology Letters*,Vol. 11, No. 2, 1999.

[73] P. Rabiei and W. H. Steier, "Tunable polymer double micro ring filters," *IEEE Photonics Technology Letters*, Vol. 15, No. 9, 2003

[74] L. B. Soldano, F B. Veerman, M. K. Smit, B. H. Verbeek, A. H. Dubost, and E. C. M. Pennings, "Planar Monomode Optical Couplers Based on multi-mode Interference Effects," *Journal of Lightwave Technology*, Vol 10, No 12, 1992.

[75] R. Ramaswami and K.N. Sivarajan, "*Optical Networks : A practical Perspective.*" Morgan Kaufmann, 1998.

[76] A. Melloni and M. Martinelli, "Synthesis of Direct-Coupled Resonators Band Pass Filters for WDM Systems," *IEEE Journal of Lightwave Technology*, Vol. 20, No.2, 2002.

[77] C. K. Madsen and J. H. Zhao, "*Optical Filter Design and Analysis*: *A Signal Processing Approach.*" Wiley, 1999.

[78] G. Lenz, B. J. Eggleton, C. R. Giles, C.K. Madsen and R.E Slusher, "Dispersive Proprieties of Optical Filters for WDM Systems," *IEEE Journal of Quantum Electronics*, Vol. 34, No.8, 1998.

[79] A. Melloni, R.Costa, G. Cusmai, F. Morichetti, P. Rosotti and M. Martinelli," *Experimental investigation of ring − resonators in SiON technology.*"2003.

[80] M. Papuchon and A. Roy, "Electrically active optical bifurcation: BOA," *Applied Physics Letters*, Vol. 31, No. 4, 1977.

[81] P A. Besse, M Bachmann, H. Melchior, L.B. Soldano, and M. K. Smit, "Optical Bandwidth and Fabrication Tolerances of multi-mode Interference Couplers," *Journal of Lightwave Techno* log *y*, Vol. 12, No. 6, 1994.

[82] O. Bryngdahl, "Image formation using self-imaging techniques," *Journal of the Optical Society of America*,63, No. 4, 1973.

[83] R. Ulrich and G. Ankele, "Self-imaging in homogenous planar optical waveguides," *Applied Physics Letters*, Vol. 27, No. 6, 1975.

[84] W. Green, *InGaAsP − InP Semiconductor Microcavity Geometries for Annular Bragg* Re *flection*, *Optical Switching*, *and Sen* sin *g*, Ph. D. Thesis, *Cali fornia Institute of Technology*, 2005.

[85] J. Haavisto and G. A. Pajer, "Resonance effects in low-loss ring waveguides," *Optics Letters*, Vol. 5, No. 12, 1980.

[86] K. Kawano and T. Kitoh, *Introduction to Optical Waveguide Analysis : Solving Maxwell's Equation and the Schrodinger Equation*, Wiley-Interscience Publications, 2001.

[87] J. M. Heaton, R. M. Jenkins, D. R. Wight, J. T. Parker, J. C. H. Birbeck, and K. P. Hilton, "Novel 1-to-N way integrated optical beam splitters using symmetric mode mixing in GaAs/AlGaAs multi-mode waveguides," *Applied Physics Letters*, Vol. 61, No. 15, 1992.

[88] W. Idler, M. Achilling, D.Baums, G.Lauble, K.Wunstel, and O.Hildebrand, "Y-laser with 38 nm tuning range," *Electronics Letters*, Vol. 27, 1990.

[89] M.Kuznetsov, P.Verlangieri, A.G.Dentai, C.H.Joyner, and C.A. Burrus, "Asymmetric Y-Branch Tunable Semiconductor Laser with 1.0 THz Tuning Range," *IEEE Photonics Technology Letters*, Vol. 4, No. 10, 1992.

[90] Kuznetsov, M., Verlangieri, P., Dentai, A. G., Joyner, C. H., and Burrus, C. A., "Widely tunable (45 nm, 5.6 THz) multi-quantum- well three-branch Y3-lasers for WDM networks, " *IEEE Photonics Technology Letters*, Vol. 5, No. 8, 1993.

[91] B. Borchert, S. Illek, T. Wolf, J. Rieger, and M. C. Amann, "Vertically integrated Mach-Zehnder interferometer (VMZ) widely tunable laser diode with improved wavelength access, " *Electronics Letters*, Vol. 30, No. 24, 1994.

[92] B. Liu, A. Shakouri, E. Bowers "Wide Tunable Double Ring Resonator Coupled Lasers," *IEEE Photonics Technology Letters*, Vol. 14, No. 5, 2002.

[93] T. Niemi, M. Uusimaa, S. Tammela, P. Heimala, T. Kajava, M. Kaivola, H. Ludvigsen "Tunable Silicon Etalon for Simultaneous Spectral Filtering and Wavelength Monitoring of a DWDM Transmitter," *IEEE Photonics Technology Letters*, Vol. 13, No. 1, 2001.

[94] S. Taghavi Larigani, J. Van Zyl, A. Yariv "Jet Propulsion Laboratory Research and Development fund 2003," accepted.